Chapter 5
Upper Water Structure and Paleo-Monsoon

Zhimin Jian, Jun Tian and Xiangjun Sun

Introduction

Hemipelagic sediments in the SCS often register higher depositional rates. Carbonate compensation depth (CCD) in this marginal ocean basin is generally deeper than neighboring sea basins. Thus the SCS offers an ideal locality for paleoceanographic studies in the low-latitude western Pacific (Wang P. 1999). The first several cores in the world ocean used for high-resolution stratigraphy using accelerator mass spectrometer (AMS) ^{14}C dating technique were from the southern part of this basin (Andree et al. 1986; Broecker et al. 1988). This is particularly significant for the western Pacific region where high-resolution paleo-studies are hampered by poor carbonate preservation and low sedimentation rates.

Climate and hydrography in the SCS are largely controlled by the monsoonal wind system which is characterized by its pronounced seasonality. Strong southwesterly winds during summer and northeasterly winds during winter drive a semi-annual reversal in surface-water circulation from approximately clockwise to anti-clockwise (Wyrtki 1961). The oceanographic features of the upper ocean such as sea surface temperatures (SST) and the thermocline are driven by the monsoon circulation and hence display conspicuous seasonality (see Chapter 2). Since the 1990s, numerous experiments and expeditions have been organized to study the East Asian monsoon in the SCS, such as the "South China Sea Monsoon Experiment (SCSMEX)" (1996–2001) by meteorologists (Ding et al. 2004), "Monitor Monsoon" expedition in 1994 (Sarnthein et al. 1994) and ODP Leg 184 (Wang P.

Z. Jian (✉)
State Key Laboratory of Marine Geology, Tongji University, Shanghai 200092, China
e-mail: jian@tongji.edu.cn

J. Tian
State Key Laboratory of Marine Geology, Tongji University, Shanghai 200092, China
e-mail: tianjun@tongji.edu.cn

X. Sun
Institute of Botany, Chinese Academy of Sciences, Beijing 100093, China; State Key Laboratory of Marine Geology, Tongji University, Shanghai 200092, China
e-mail: sunxj@tongji.edu.cn

P. Wang, Q. Li (eds.), *The South China Sea*, Developments in Paleoenvironmental Research 13, DOI 10.1007/978-1-4020-9745-4_5,
© Springer Science+Business Media B.V. 2009

et al. 2000) by earth scientists. Now the SCS and the Arabian Sea respectively have become the foci for the East and South Asian monsoon studies in both modern and paleo-climatology (Wang B. et al. 2003).

The upper ocean and monsoon of the SCS in the geological past were highly sensitive to changes in climate boundary conditions. During glacial periods, the SCS became a semi-enclosed basin connected to the western Pacific through the Bashi Strait and to the Sulu Sea through the Balabac and Mindoro Straits due to low sea level, inevitably resulting in a pronounced difference in surface and deep circulation (Wang P. et al. 1995; Jian and Wang 1997) and hence altering the upper water structure and deep water conditions. Since the 1990s, a large number of papers have been published on the monsoonal evolution and variability using proxy measurements relating to changes in SST, vertical thermal structure, productivity, wind-blown (e.g., eolian dust and specific pollens) and river-discharged grains (Wang P. et al. 2005 and references herewith). The present chapter provides a synthesis of the upper ocean structure and East Asian monsoon history in the SCS, beginning with the SST and thermocline depth history, then the vegetation history in the deep-sea pollen record, and finally an outline of the monsoon history.

5.1 Sea Surface Temperature History (Jian Z. and Tian J.)

SST Proxies

Sea surface temperature (SST) is not only one of the main subjects for international paleoceanographic studies since the 1970s like CLIMAP, but also the starting point of the East Asian paleo-monsoon study since the 1990s in the SCS. So far, three methods including paleoecology of planktonic foraminiferal transfer function, alkenone unsaturation index ($U^{K'}_{37}$) of sediments, and Mg/Ca ratios of planktonic foraminiferal tests have been applied to reconstruct the past SST variations in the SCS. Numerous paleo-SST sequences have been generated, in particular for the late Quaternary, although the use of some SST proxies remains debatable.

Foraminiferal Transfer Function

The first attempt to reconstruct paleo-SST in the SCS was in 1990, when transfer function FP-12 was applied to foraminiferal census over the last glacial cycle at 3 core sites in the northern SCS (Wang and Wang 1990). It was found that the glacial/interglacial SST contrast was much more significant in the SCS than in the adjacent open Pacific, indicating an amplifier effect of glacial signals in the marginal sea. However, the transfer function FP-12E initially employed was a regional version of Imbrie-Kipp's transfer function, based on census data of planktonic foraminifers in 165 coretops from the open western Pacific Ocean, with the standard errors of 2.48 °C for winter SST and 1.46 °C for summer SST (Thompson 1981). The SST reconstruction using FP-12E has inevitable biases in the marginal seas where upper ocean hydrology is different from that of the open Pacific.

To avoid these drawbacks, Pflaumann and Jian (1999) developed a calibrated SIMMAX-28 transfer function to estimate past SST in the SCS. SIMMAX method used modern analog technique with a similarity index (Pflaumann et al. 1996). SIMMAX-28 was based on 30 new planktonic foraminiferal census data of surface sediment samples recovered between 630 and 2883 m water depths in the SCS, together with the 131 data sets published from the western Pacific. The standard errors of the transfer function SIMMAX-28 are 1.27 °C for winter SST and 0.45 °C for summer SST. This regional SIMMAX method offers a slightly better understanding of the marginal sea conditions of the SCS than FP-12E, but is also biased toward the tropical temperature regime, like FP-12E, because of the very limited data from temperate and subpolar regions. Application of SIMMAX-28 transfer function on sediment core 17940 from the northern SCS (Pflaumann and Jian 1999) revealed nearly unchanged summer temperatures around 28 °C for the last 30 kyr, while winter temperatures varied between 19.5 °C in the last glacial maximum (LGM) and 26 °C during the Holocene, and during Termination 1A the winter estimates show a Younger Dryas cooling by 3 °C subsequent to a temperature optimum of 24 °C during the Bølling/Allerød period.

The different results from the two methods can be illustrated with an example from the southern SCS, namely the SST-sequence of core 17957-2 over the past 1.5 myr (Fig. 5.1) (Jian et al. 2000b). Estimates of the winter and summer SSTs for the core top are 27.2 °C and 29.4 °C using FP-12E, and 27.0 °C and 28.9 °C

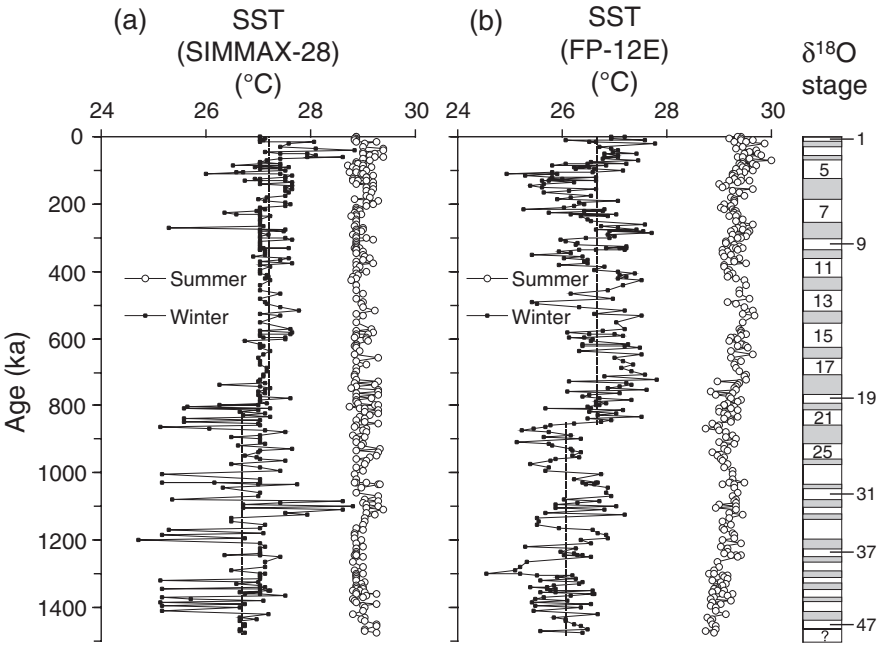

Fig. 5.1 Down-core variations in the estimated winter and summer SSTs in core 17957-2 using (**a**) SIMMAX-28 and (**b**) FP-12E methods show slightly different results (from Jian et al. 2000b). *Dashed lines* mark the average winter SST before and after marine isotope stages (MIS) 21–20

using SIMMAX-28, respectively. For the whole core, the SIMMAX-28 derived winter SST varies from 24.7 to 27.8 °C, while the summer SST varies from 28.8 to 29.4 °C. Both FP-12E and SIMMAX-28 derived winter and summer SSTs are slightly warmer with a narrow range of seasonality in core 17957-2 when compared to previous estimates using transfer function FP-12E (Wang and Wang 1990; Miao et al. 1994; Wang P. et al. 1995). Glacial/interglacial cycles are well presented in the FP-12E derived SST records but are somewhat obscured in the SIMMAX-28 derived SST records (Jian et al. 2000b).

For core MD972151 from the southern SCS, five transfer functions including the Imbrie-Kipp method (IKM), modern analog technique (MAT), modern analog technique with similarity index (SIMMAX), revised analog method (RAM), and the artificial neural network technique (ANN) were used to evaluate the magnitude of cooling during the LGM (Chen M. et al. 2005). The MAT, SIMMAX, RAM and ANN showed similar SST estimation results with $\leq$1 °C uncertainties in coretop SST calibrations. The IKM performed significantly worst in the calibration exercise, producing glacial SST estimates similar to present-day values, whereas all other four techniques indicated $\sim$1 °C cooler glacial SST in the tropical western Pacific.

Alkenone Unsaturation Index

Pelejero and Grimalt (1997) established a calibrated linear relationship between $U^{K'}_{37}$ in surface sediment samples mainly consisting of coccolithophorids and SST for the SCS. The relationship between C_{37} alkenones composition and water temperature is based on the degree of unsaturation of the ketones, which is measured by means of several indices: $U^{K}_{37} = (C_{37:2} - C_{37:4})/(C_{37:2} + C_{37:3} + C_{37:4})$ and $U^{K'}_{37} = (C_{37:2})/(C_{37:2} + C_{37:3})$, where $C_{37:4}$, $C_{37:3}$ and $C_{37:2}$ are the concentrations of heptatriaconta-(8E, 15E, 22E, 29E)- tetraen-2-one, heptatriaconta-(8E, 15E, 22E)-trien-2-one and heptatriaconta-(15E, 22E)-dien-2-one, respectively. Even in the warm waters (25–29 °C) of the SCS, $U^{K'}_{37}$ and SST show a good linearity, indicating that the alkenone unsaturation index ($U^{K'}_{37}$) is a good SST proxy. This linear relationship is expressed as an equation, $U^{K'}_{37} = 0.031T + 0.092$, which is very similar to the frequently used equation ($U^{K'}_{37} = 0.033T + 0.043$) established for *Emiliania huxleyi* in culture and column water samples (Prahl and Wakeham 1987). The equation of $U^{K'}_{37}$ is valid for temperatures of the annually averaged water mass between 0 and 30 m in the SCS. SST estimates using this equation for core 17961-2 from the southern SCS show significant SST increases during Termination I. In sediment cores 18252-3 and 18287-3 from the southwestern and southern SCS, $U^{K'}_{37}$-derived SST increased abruptly by 1 °C or more at the end of Termination IA (Kienast et al. 2001, 2003), concurrent with the pre-Bølling warming about 14.6 ka ago observed in the Greenland Ice Sheet Project (GISP) 2 ice core. In IMAGES core MD972151 from the southern SCS, Zhao et al. (2006) used $U^{K'}_{37}$ to reconstruct the SST history for the past 150 kyr on a millennial scale, suggesting glacial/interglacial SST changes by 4 °C and 5 °C for Termination I and Termination II, respectively.

However, Bentaleb et al. (2002) questioned the usage of $U^{K'}_{37}$ as a SST proxy after calibrating water samples collected from the western Pacific Ocean. Their results showed a constant value of unity (1.0) for the $U^{K'}_{37}$ index when the surface

water temperature reached 26.4 °C, indicating that paleo-SSTs above 26.4 °C may not be accurately calculated by using the $U^{K'}_{37}$ index. Pelejero and Calvo (2003), however, pointed out that Bentaleb et al. (2002) might have been made errors in designating a value of unity to the $U^{K'}_{37}$ index when the $C_{37:3}$ alkenone was not detected. Zhao et al. (2006) detected both $C_{37:2}$ and $_{37:3}$ alkenones in all samples from the southern SCS, enabling them to estimate SST up to 29 °C during MIS 5.5, which supports the use of the $U^{K'}_{37}$ index as a paleothermometer in the region.

Mg/Ca Ratios of Foraminifera

The Mg/Ca ratio of planktonic foraminiferal shells has also been widely used as useful proxy of past SST reconstruction in the SCS. This method has been proved to be valid in a number of oceanographic settings (Hasting et al. 1998; Lea et al. 2000). Mg paleothermometry has certain unique advantages over other proxies (Lea et al. 2000), the most important of which is that Mg/Ca is measured in foraminiferal shells, which are by themselves a vital archive of past climate and the carrier phase for oxygen isotopes. Measuring both Mg/Ca and $\delta^{18}O$ in foraminiferal shells from the same sample makes it possible to separate the magnitude and timing of SST and $\delta^{18}O_{water}$ changes (Elderfield and Ganssen 2000). Hasting et al. (2001) developed an empirical equation based on core top sample calibrations, i.e., Mg/Ca ($mmol.mol^{-1}$) $= 0.38 \times \exp(0.089 \times SST(°C))$, and then compared three independent paleotemperature estimates from an AMS ^{14}C-dated core 18287-3 from the southern SCS: Mg/Ca ratio from planktonic foraminifera (*Globigerinoides ruber* and *Globigerinoides sacculifer*), alkenone thermometry ($U^{K'}_{37}$) and different foraminiferal transfer functions (SIMMAX28, RAM and FP-12E). Results from these three different methods show similar average glacial/interglacial temperature differences of about 2.5 °C. The most important shift that appears in all the three records is an abrupt SST increase by about 1.3–1.8 °C near the end of the last glacial period, synchronous with the 14.6 ka warming event observed in the GISP2 ice core. At two depth intervals with enhanced preservation, the Mg/Ca-deduced SSTs were 1 to 3.5 °C higher than predicted, which led Hasting et al. (2001) to conclude that even in a shallow core expected to have no significant carbonate dissolution, enhanced preservation events may lead to more positive Mg/Ca values and, therefore, higher inferred SST.

Not only dissolution but also planktonic foraminiferal species variations affect the validity of Mg/Ca as a paleo-SST proxy. Core top Mg/Ca measurements of samples from the tropical Pacific and Atlantic indicate *G. ruber* being the most accurate SST recorder and *G. sacculifer* a subsurface temperature register at 20–30 m (Dekens et al. 2002). When considering water depth of a core as a dissolution correction parameter and ΔCO_3^{2-} a dissolution parameter, a calibrated equation for *G. ruber* Mg/Ca in the Pacific can be used: Mg/Ca $=$ 0.38exp[SST-0.61(core depth km)$-$1.6 °C] (Dekens et al. 2002). All the results from using this equation are plausible, as seen from SST reconstructions for Site 1143 between 3.3 and 2.5 Ma (Tian et al. 2006) and for Site 1145 for the past 145 kyr (Oppo and Sun 2005).

Wei et al. (2007) measured Mg/Ca in *G. sacculifer* for a past ~260 kyr SST reconstruction at Site 1144. Because there is no calibration for *G. sacculifer* in the

SCS, Wei et al. (2007) established the relationship between SST and Mg/Ca ratios on *G. sacculifer* shells without a sac chamber by five calibrations, including shells from culture (Nürnberg et al. 1996), from core-top sediments (Dekens et al. 2002; Rosenthal and Lohmann 2002), and from sediment traps (Anand et al. 2003). Each calibration was evaluated by two calculated results: SST of the topmost sample and SST change from LGM to the Holocene. Evaluation shows that SST calculations based on *G. sacculifer* in the SCS from Nürnberg et al. (2000) ($T = (\log Mg/Ca - \log 0.491)/0.033$), Anand et al. (2003) ($Mg/Ca = 0.347 \exp(0.090T)$) and Dekens et al. (2002) for the Atlantic ($Mg/Ca = 0.37 \exp[0.09(T - 0.36$ core depth km)]) agree quite well with each other with average temperature offsets less than 0.1 °C.

The planktonic foraminifer *G. ruber* (white) has two morphotypes, *G. ruber* sensu stricto (s.s.) living in the top 30 m of the water column and *G. ruber* sensu lato (s.l.) living at depths below 30 m (Wang L. 2000). Steinke et al. (2005) showed that *G. ruber* s.s. often register significantly higher Mg/Ca ratios than *G. ruber* s.l. as the latter precipitated its shells in slightly colder waters. Increased temperature differences between the two morphotypes occur mostly during periods of low salinity, especially during the Bølling/Allerød and the early Holocene. Their findings are supported by $\delta^{18}O$ and $\delta^{13}C$ differences between the two morphotypes and by stable oxygen isotope studies on core-top material from the SCS (Wang L. 2000; Löwemark et al. 2005) and by plankton tow and pumping studies from the Pacific (Kuroyanagi and Kawahata 2004). However, even the author themselves (Steinke et al. 2005, 2008a) accept that specimens of the two morphotypes of *G. ruber* are usually insufficient in high-resolution core samples for separate Mg/Ca analyses, thus a SST bias using both morphotypes appears to be unavoidable.

Intercomparison

SST reconstructions derived from planktonic foraminiferal transfer functions usually produce significant discrepancies with those derived from alkenone unsaturation and Mg/Ca ratios (Huang et al. 1997b; Steinke et al. 2001). In addition, SST records from different foraminifer transfer functions do not always agree with each other (Jian et al. 2000b; Steinke et al. 2001; Chen M. et al. 2005). To test the reliability of SST reconstructions, Steinke et al. (2008b) compared SST estimates using five different transfer function techniques on planktonic foraminiferal faunal census data from core MD01-2390 in the tropical southern SCS. All SST records derived from transfer functions indicate nearly unchanged or unusually higher temperatures during the LGM relative to modern temperatures, in contrast to substantial cooling of 2–5 °C inferred by $U^{K'}_{37}$ or Mg/Ca ratios from the same core (Steinke et al. 2006). The glacial planktonic foraminiferal assemblage from the southern SCS that has no modern analog is the main reason why the transfer function derived SST estimates for the LGM are inaccurate (Steinke et al. 2008b). The abundances of *Pulleniatina obliquiloculata* and *Neogloboquadrina pachyderma* (dextral) are abnormally high in glacial assemblages. The glacial high abundance of *P. obliquiloculata* probably resulted from a process involving stronger mixing and/or enhanced upwelling due to an intensified winter monsoon, which prevented shallow-dwelling, warm

indicators to establish larger populations. Similarly, the glacial high abundance of *N. pachyderma* (dextral) was likely caused by a winter inflow of cold surface water from the northeast via the Bashi Strait due to the combined effects of an intensified winter monsoon, a southward shift of the polar front and the eastward migration of the Kuroshio Current during the LGM (Steinke et al. 2008b). As reported also by Jian et al. (1999), Huang et al. (2002), Steinke and Chen (2003) and Xu et al. (2005), *P. obliquiloculata* during glacials was consistently more abundant at southern than northern SCS localities, implying a unique phenomenon from the southern SCS. The abnormal glacial planktonic foraminiferal assemblage often causes warm SST estimates for the southern SCS using transfer functions (Chen M. et al. 2005; Steinke et al. 2008b). Comparatively, therefore, SST estimates based on Mg/Ca ratios and alkenone unsaturation index are more realistic and reliable (Steinke et al. 2008a,b).

In core 17940 from the northern SCS, the estimated annual SST curve (average of summer and winter SST) based on $U^{K'}_{37}$ measurements shows a smoother outline without the obvious short-term fluctuations revealed by the SIMMAX-derived SST curve during the Holocene and the LGM (Pelejero et al. 1999a). The discrepancy between the planktonic foraminiferal- and $U^{K'}_{37}$ (coccolithophorids)-derived SST may be attributed to the disparity between these two organisms. While coccolithophorids are nannoplankton living in the uppermost water, planktonic foraminifera live in water column from the sea surface down to several hundred meters and different species reach peak abundances at different times throughout the year. In addition to temperature, planktonic foraminiferal assemblage may have been affected by other water mass variables such as salinity and by fertility (Pflaumann and Jian 1999).

Paleo-SST Reconstruction

Most of the continuous paleo-SST records from the SCS, especially those derived from geochemical methods ($U^{K'}_{37}$ and Mg/Ca ratios), cover only the late Pleistocene. Although faunal transfer functions are biased in SST estimates for the glacial southern SCS (Chen M. et al. 2005; Steinke et al. 2008b), they are still the main technique used to reveal the long-term trend of SST variability in the SCS on the tectonic timescale.

Plio-Pleistocene

The longest paleo-SST sequences from the SCS are those derived from ODP Leg 184 cores. Late Pliocene-Pleistocene SST records have been obtained using PF-12E transfer functions at Site 1143 in the southern SCS (2.5–0 Ma), and at Site 1146 (4–0 Ma) and Site 1144 (1.1–0 Ma) in the northern SCS (Li B. et al. 2004; Zheng et al. 2005) (Fig. 5.2). In these studies, the extinct species were replaced by their modern counterparts for SST calculations (Anderson 1997). The results show that winter SST gradually decreased at Site 1146 since 3.1 Ma, superimposed by large amplitude fluctuations. The decrease by more than 7 °C on average was in parallel with an upcore reduction in the abundance of mixed-layer species influenced by the

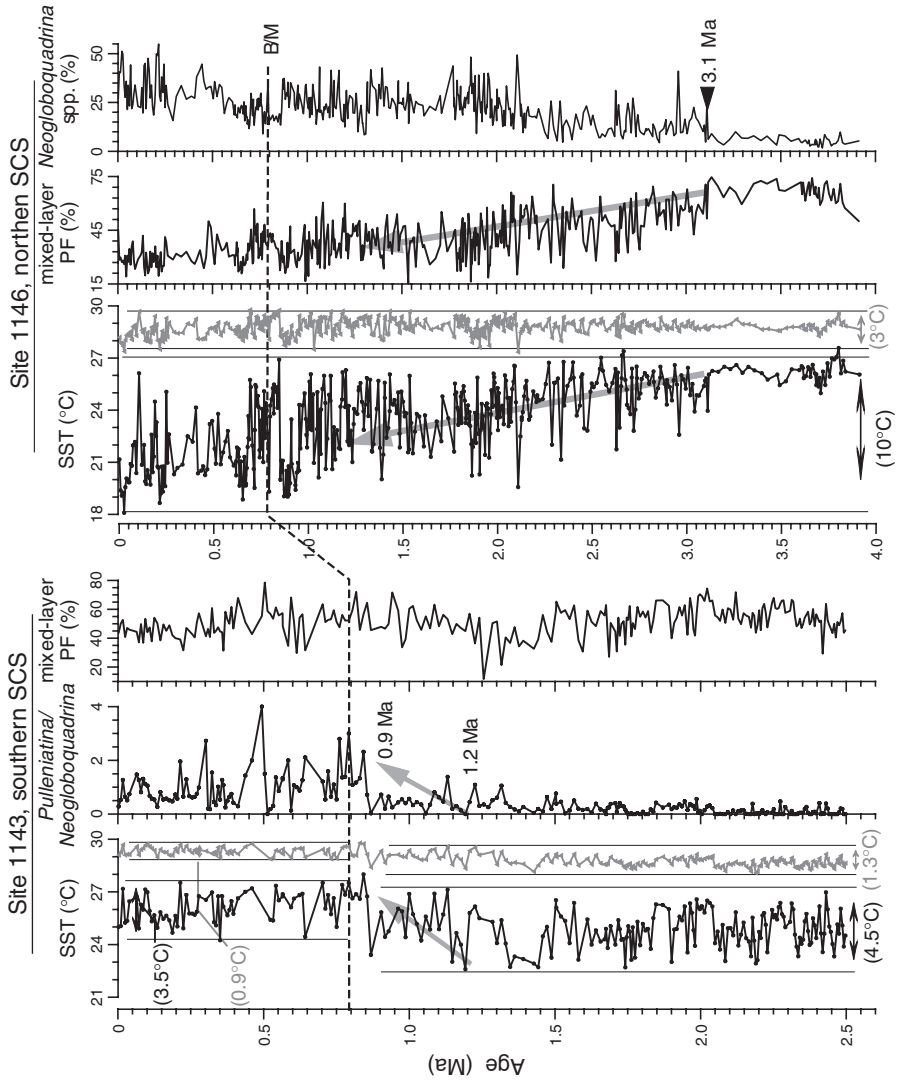

Fig. 5.2 Comparison of transfer-function estimated winter (*black*) and summer (*gray*) SST variations between Site 1143 and Site 1146 shows different trends since the late Pliocene (after Li B. et al. 2004 with Site 1146 data from Huang B. 2002). B/M is Brunhes/Matuyama paleomagnetic boundary at 0.78 Ma

East Asian winter monsoon variability. The decreased SST at Site 1146, therefore, was probably responding to intensified East Asian winter monsoon especially during the period of 3.1–2.0 Ma, as documented also in terrestrial records from the loess plateau (An 2000) and marine isotopic records from the southern SCS (Tian et al. 2004, 2006).

At Site 1143 from the southern SCS, the amplitudes of the SST fluctuations were 1.3 °C for summer and 4.5 °C for winter between 2.5 and 0.9 Ma but changed to 0.9 °C for summer and 3.5 °C for winter after 0.9 Ma, consistent with SST estimates from other southern SCS sites (e.g., Fig. 5.1). Therefore, the southern SCS has maintained relatively warm and stable SST since the late Pliocene, while the northern SCS experienced larger amplitude SST fluctuations especially during the Pleistocene.

Of particular interest are rapid SST changes in such periods as 3.1–2.5 Ma and 1.2–0.9 Ma. For the period from 3.3 to 2.5 Ma, the estimated SST at ODP Site 1143 using Mg/Ca ratio of *G. ruber* varies between 31 and 26.4 °C, showing a pattern of stepwise decrease corresponding to the onset of the significant Northern Hemisphere Glaciation (Fig. 5.3) (Tian et al. 2006). Three steps (periods 1–3) of SST changes can be recognized: MIS M2-G18 (3.3–2.97 Ma), G18-G6 (2.97–2.7 Ma), and G6-99 (2.7–2.5 Ma), with SST decreasing by ~5 °C from 3.3 to ~2.7 Ma before increasing by ~1.5 °C until ~2.5 Ma. Moreover, the amplitude of the millennial- or orbital-scale variability of SST also decreased (Tian et al. 2006).

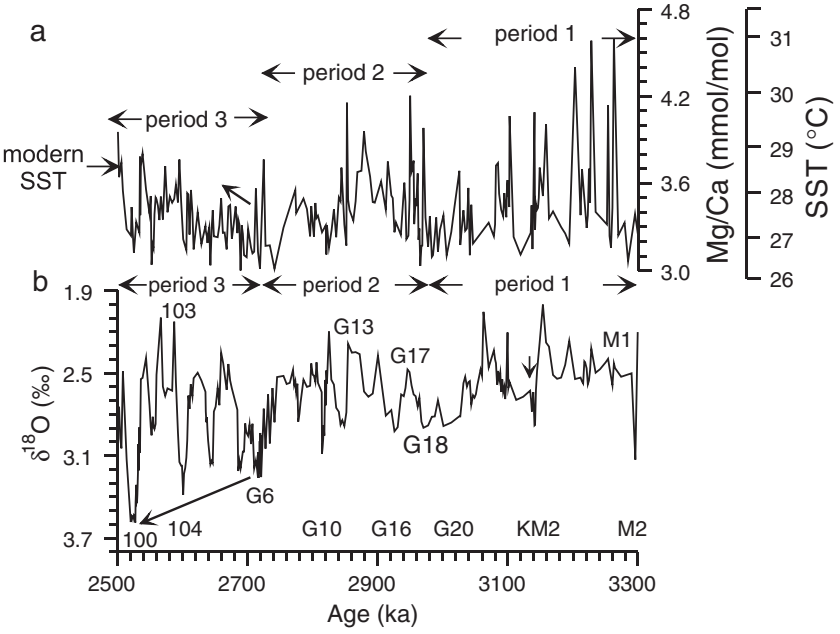

Fig. 5.3 Paleo-SST reconstruction for 3.3–2.5 Ma at ODP Site 1143, southern SCS, based on Mg/Ca ratio of *G. ruber* shows stepwise SST decreases from period 1 to period 3 (modified from Tian et al. 2006). (**a**) Mg/Ca ratio and Mg/Ca derived sea surface temperature; (**b**) *Cibicidoides* $\delta^{18}O$. The letters and numbers denote Marine Isotope Stages (MISs)

For the period from 1.2 to 0.9 Ma, the estimated SST at ODP Site 1143 using transfer function PF-12E shows winter SST increases by ~2 °C (Fig. 5.2a; Li B. et al. 2004). Because *P. obliquiloculata* contributes 80% to a tropical dissolution-resistant factor in PF-12E (Thompson 1981), its relatively high abundance since 0.9 Ma probably contributed to estimated SST higher than in earlier periods, consistent also with an increase in the *Pulleniatina/Neogloboquadrina* ratio (Fig. 5.2b). As *Pulleniatina* and *Neogloboquadrina* are both deep-dwelling species but respectively indicate warmer and cooler water temperatures (Hemleben et al. 1989; Chaisson 1995), their ratio increase at 0.9 Ma may indicate a warm subsurface water mass in the southern SCS at the time. The SST variations, *Pulleniatina* abundance, and *Pulleniatina/Neogloboquadrina* ratio at Site 1143 all indicate relatively warm surface waters in the southern SCS during the Pleistocene with enhanced warm subsurface waters right after the mid-Pleistocene climate transition between 1.2 and 0.9 Ma. A similar finding was reported from core 17957-2 also in the southern SCS, although the SST estimates using FP-12E and SIMMAX-28 show slightly different results (Fig. 5.1) (Jian et al. 2000b). The SIMMAX-28-derived winter SST exhibit larger amplitude fluctuations before the Brunhes/Matuyama (B/M) boundary, whereas the PF-12E-derived winter SST show greater changes across the MIS 22/21 transition (Fig. 5.1).

Late Pleistocene

Late Pleistocene SST variations have been studied in numerous cores in the SCS with higher time resolutions than those Pliocene-Pleistocene records. Wang L. et al. (1999a) reported a millennial-scale $U^{K'}_{37}$ SST record for the past 35 kyr from core 17940, northern SCS, by calibrating $U^{K'}_{37}$ to annual mean SST in 0–30 m water depth, together with the FP-12E-based summer and winter SST estimates (Fig. 5.4). While the summer SST remained almost constant over the entire last glacial cycle, the winter SST decreased with a number of short-term negative oscillations by ~2 °C during the MIS 3, paralleling some "warm" $\delta^{18}O$ minima. The MIS 2 SST minima match well with heavy $\delta^{18}O$ values toward the end of the LGM. Prominent declines in winter SST also occur in the late Holocene.

In the southern SCS, Steinke et al. (2006) reported a high resolution SST record for the past 22 kyr based on planktonic foraminiferal Mg/Ca ratios from core MD01-2390 (Fig. 5.5), showing an average temperature change of 3.1 ± 0.6 °C. This temperature change is relatively larger than previous reconstructions. This could be related to the fact that the entire *G. ruber* population instead of "morphospecific" samples of *G. ruber* s.s. from the glacial period was used for Mg/Ca measurements. As mentioned above, *G. ruber* s.l. specimens generally yield lower Mg/Ca ratios and hence lower SST estimates compared to G. *ruber* s.s. In core MD01-2390, the abundance of *G. ruber* in LGM samples is very low, and the use of both *G. ruber* s.l. and *G. ruber* s.s. for Mg/Ca analyses contributes to lower SST-estimations for the LGM (Steinke et al. 2006, 2008a).

An abrupt temperature increase by at least 1 °C at the end of Heinrich 1 (H1) event (Termination IA) is recorded in two short $U^{K'}_{37}$ SST records spanning the

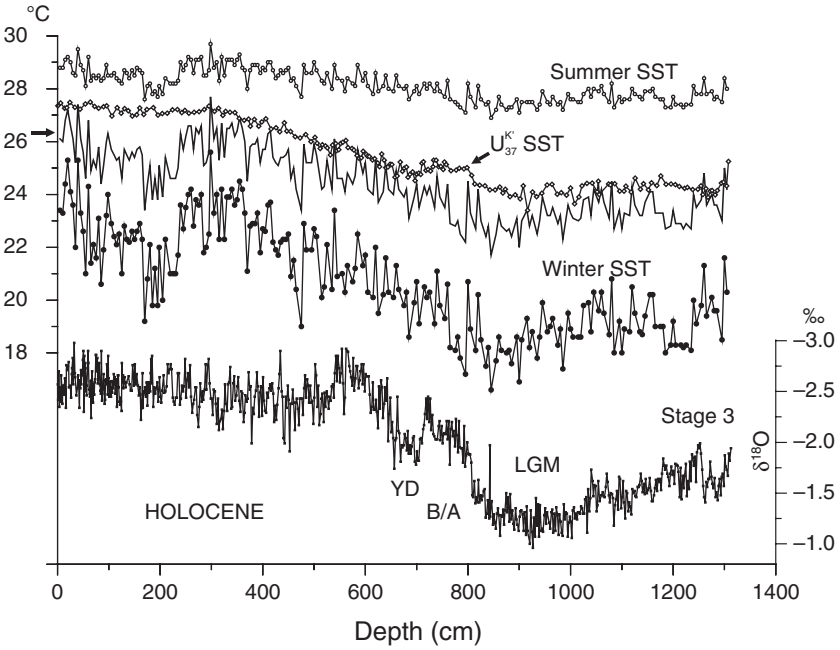

Fig. 5.4 SST estimates for core 17940 in the northern SCS are based on FP-12E transfer function (*circles* for summer, *dots* for winter and *coarse line* for the annual mean) and based on the $U^{K'}{}_{37}$ (*diamonds* for annual mean SST), as compared with *G. ruber* $\delta^{18}O$ curves (modified from Wang L. et al. (1999a). YD = Younger Dryas; B/A = Bølling-Allerød. Horizontal arrow marks modern annual mean SST value at 0–30 m

last 13,000 yr from cores 18287-3 and 18252-3 in the southern SCS (Fig. 5.6) (Kienast et al. 2001). Within the recognized dating uncertainties, this SST increase was synchronous with the Bølling warming 14.6 ka ago as recorded in the GISP2 ice core.

SST Variations at Millennial Scales

In recent years, remarkable progresses have been made on SST reconstructions on millennial time scales in the SCS. Representing these are the alkenone derived SST record in IMAGES core MD972151 from the southern SCS (Zhao et al. 2006) and the Mg/Ca derived SST record at ODP Site 1145 from the northern SCS (Oppo and Sun 2005).

In the southern SCS, the alkenone data from core MD972151 generate a SST record over the past 150 kyr, with sampling resolution of 150 to 200 years (Fig. 5.7) (Zhao et al. 2006). It shows glacial SST variations from 23.5 to 26 °C and interglacial SST variations from 27 to 28.9 °C, in general agreement with previously reported records from the southern SCS (Pelejero et al. 1999a,b; Wang P.1999; Kienast et al. 2001; Steinke et al. 2001; Chen M. et al. 2005) and from the tropical western Pacific ocean (Lea et al. 2000; Stott et al. 2002; Rosenthal et al. 2003; Visser et al. 2003).

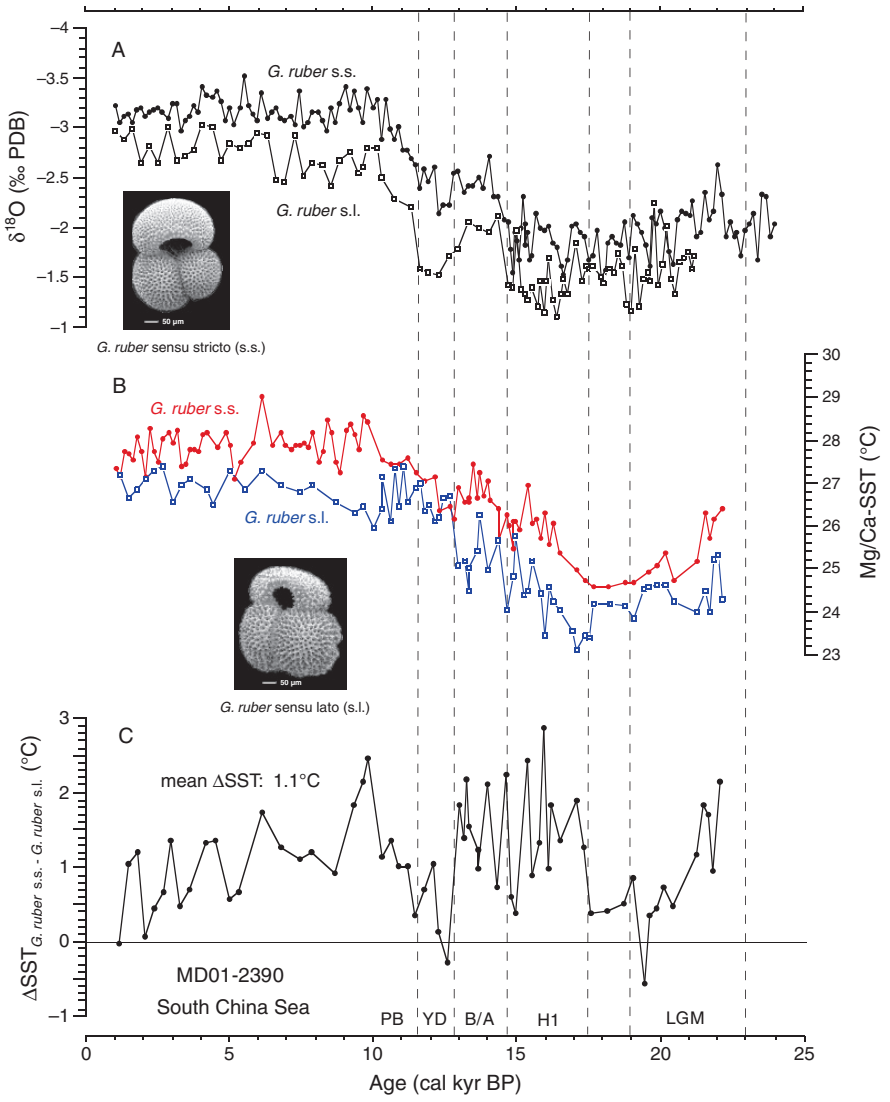

Fig. 5.5 Paleo-records from two morphotypes of *G. ruber* in core MD01-2390 are compared: (A) δ^{18}O of *G. ruber* s.s. and *G. ruber* s.l., (B) inferred SSTs using Mg/Ca ratios in *G. ruber* s.s. (*filled circles*) and *G. ruber* s.l. (*open circles*), and (C) SST differences between these two morphotypes (from Steinke et al. 2006, 2008a). PB = Preboreal; YD = Younger Dryas; B/A = Bølling–Allerød; H1 = Heinrich 1 event; LGM = Last Glacial Maximum

SST increased by ~5 °C during Termination II and by ~4 °C during Termination I. For Termination I, the lowest SST (23.8–24.0 °C) was recorded at 15.2–14.1 ka, just prior to the Bølling transition instead of during the LGM between 23 and 19 ka. Following this was an increase by 3 °C (to 27 °C) within 100 years during

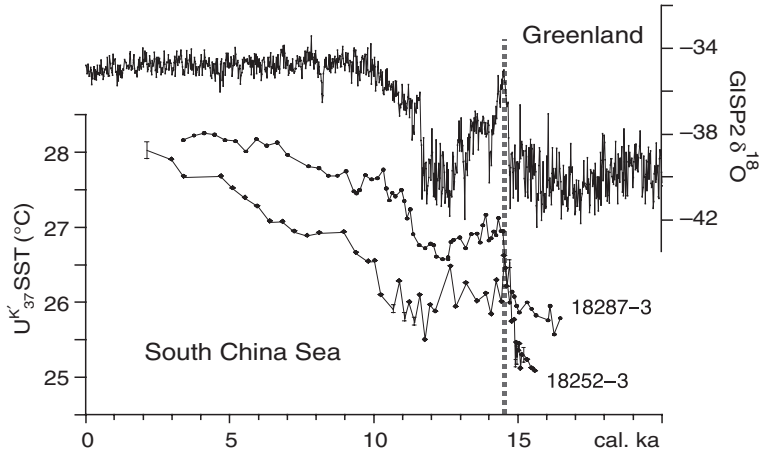

Fig. 5.6 $U^{K'}_{37}$ SST records in cores 18252-3 and 18287-3 from the southern SCS on independent calendar time scales are compared with the GISP2 $\delta^{18}O$ record (Stuiver and Grootes 2000), showing contemporary SST increase at 14.6 ka marked by the vertical dashed line (Kienast et al. 2001)

the Bølling/Allerød and IS1 warm event. A similar SST pattern occurred also in Termination II, with a very cold event (23.5–23.7 °C) lasting 2700 years (between 137 and 134 ka) in late MIS 6 (Fig. 5.7). Frequent SST oscillations were observed within MIS 3, with frequencies similar to the D-O cycles observed in Greenland ice cores. SST was around 26 °C during typical warmer interstadial events and dropped to ~24.4 °C during colder stadial events.

The SST curve from core MD972151 is comparable with the $\delta^{18}O$ record of the Hulu stalagmite from eastern China (Wang Y. et al. 2001) with some minor differences (Fig. 5.7). Between 65 and 10 ka, the SST oscillated within a range of 24–26 °C, while the Hulu $\delta^{18}O$ fluctuated between −6.5 and −9.5‰ during the period of 60–30 ka before increasing to a maximum of −4.5‰ at 16 ka. These millennial-scale oscillations in the two records correlate well with each other and with the Greenland GISP2 record. Within the error of the age model, for example, most of the positive SST excursions on the order of 1.0–1.5 °C over a few hundred years can be correlated with the interstadials in the GISP2 record and with more negative $\delta^{18}O$ values in the Hulu $\delta^{18}O$ record, indicative of stronger summer monsoons. Similarly, several significant cool intervals (24.4–24.2 °C) between these interstadial events possibly correspond to the Heinrich events reported from the North Atlantic Ocean (Bond et al. 1993; Chapman et al. 2000) (Fig. 5.7). Therefore, Zhao et al. (2006) concluded that millennial-scale SST changes in the SCS were mainly caused by the variability of the winter monsoon. Moreover, the simultaneous rise in sea level and in $U^{K'}_{37}$ SST during Termination I indicates an important role of sea-level change on the regional SST variability by influencing the exchange of tropical ocean warm surface water with the SCS water through the Sunda Shelf region (sill depth 30–50 m). When sea-level drop was less than 30 m relative to

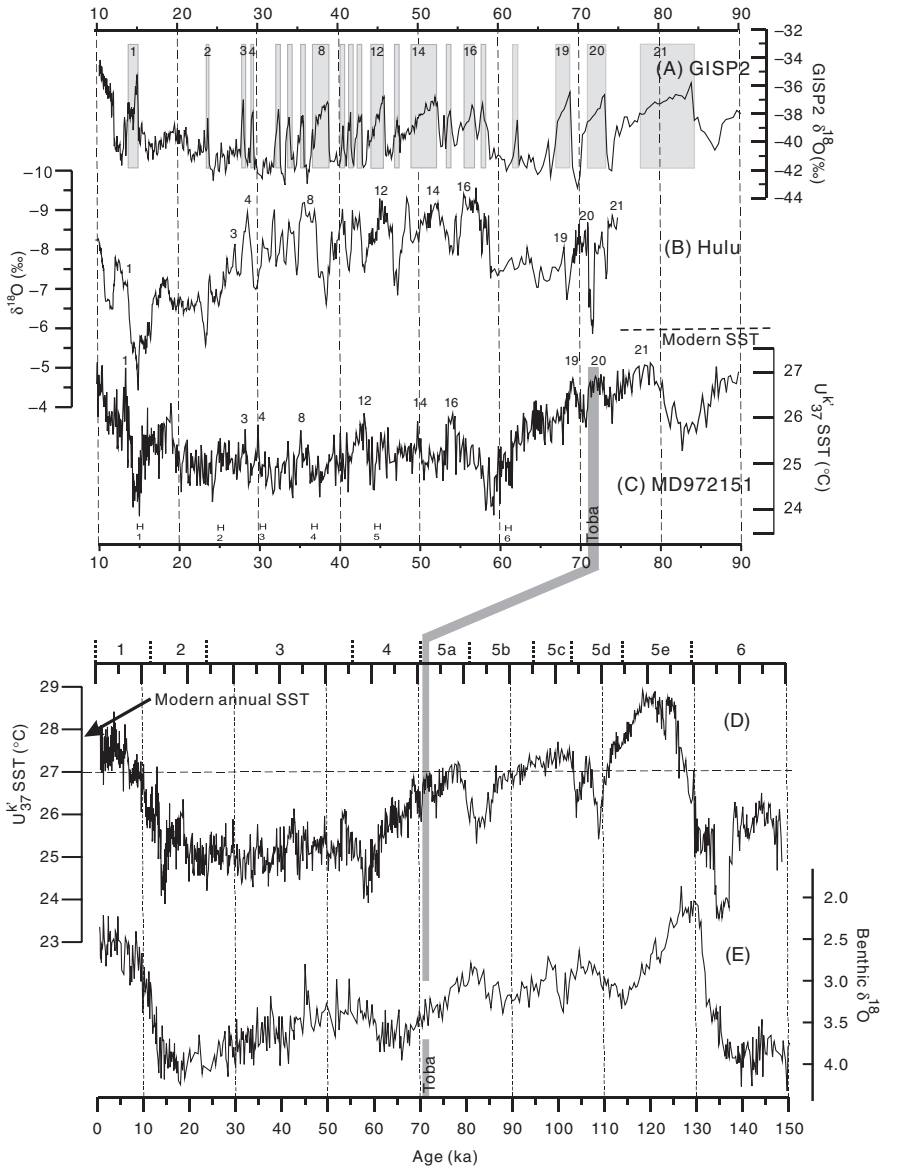

Fig. 5.7 Comparison between $U^{K'}_{37}$ SST and benthic $\delta^{18}O$ records of core MD972151 (C, D, E) and the $\delta^{18}O$ record of the Hulu Cave (B) (Wang Y. et al. 2001) and the $\delta^{18}O$ record of the GISP2 ice core from Greenland (A) (Dansgaard et al. 1993) shows a good correlation of interstadial events and Heinrich events (H1 to H61) (from Zhao et al. 2006). The vertical bar indicates the youngest Toba tephra layer. Below 40 ka, GISP2 has turned out to deviate by 2500 yrs from new annual-layer counts (Svensson et al. 2008)

today's, SST at MD972151 was constantly above 27 °C, a situation which occurred during MIS 5e, part of MIS5c and 5a, and over the last 11 kyr (Zhao et al. 2006).

In the northern SCS, Oppo and Sun (2005) reconstructed SST variations at ODP Site 1145 for the past 140 kyr (Fig. 5.8) using an equation developed for *G. ruber* Mg/Ca ratios in the Pacific (Dekens et al. 2002). The estimated SST for the late Holocene was ~28 °C, corresponding to an abundance peak of *G. ruber* in late summer. The maximum SST of the previous interglacial (MIS 5e) was ~1 °C warmer than the late Holocene, in a good agreement with alkenone-based SST estimates (Pelejero et al. 1999a). Glacial SST was ~4 °C colder than the late Holocene, also consistent with previous estimates for the northern SCS (Wang P. et al. 1995; Pelejero et al. 1999a). After the MIS 5e temperature peak, SST within the last interglacial changed several times by ~3 °C marking other MIS 5 substages (Fig. 5.8).

Suborbital SST changes at Site 1145 are best developed since ~80 kyr. Based on a visual correlation between the SST record and the Hulu $\delta^{18}O$ record, Oppo and Sun (2005) suggested that SST changes in the northern SCS were synchronous with abrupt events in the seasonality of monsoon precipitation and in temperature changes over Greenland, and that the distinct cold events likely corresponded to the Heinrich events from episodic massive iceberg discharges into the subpolar North

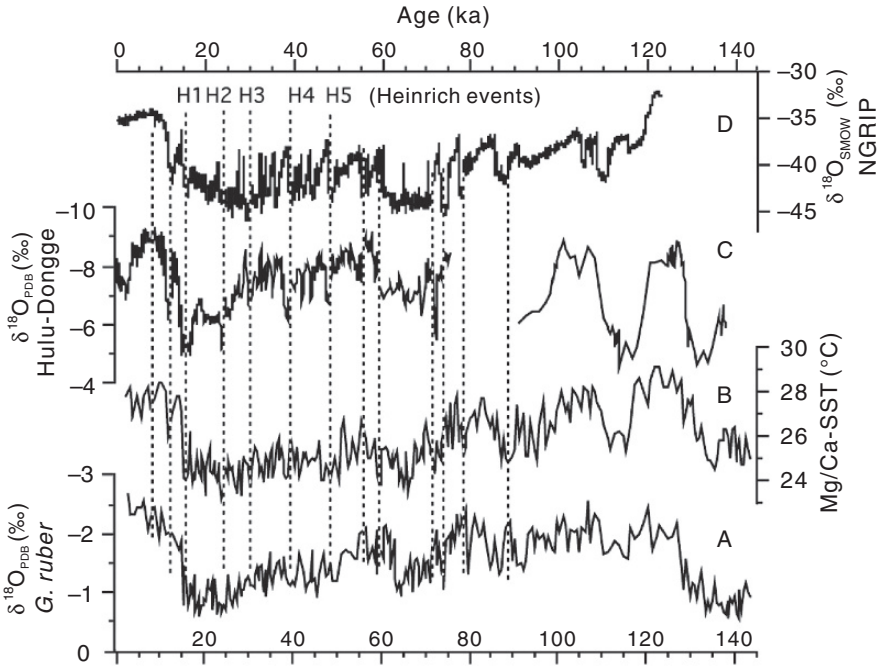

Fig. 5.8 Planktonic $\delta^{18}O$ (A) and Mg/Ca-based SST (B) from ODP Site 1145 are compared with various $\delta^{18}O$ records: (C) speleothem $\delta^{18}O$ from Hulu Cave (Wang Y. et al. 2001) and Dongge Cave (Yuan et al. 2004), and (D) Greenland ice core $\delta^{18}O$ (NGRIP Members 2004). *Dashed lines* mark likely correlations between marine and terrestrial records (from Oppo and Sun 2005)

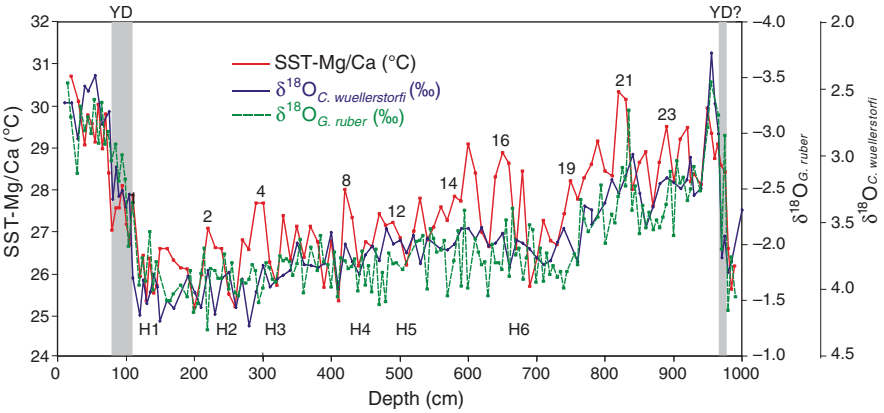

Fig. 5.9 Comparison between Mg/Ca SST estimates and $\delta^{18}O$ records of benthic (*C. wuellerstorfi*) and planktonic foraminifera (*G. ruber*) in core 17961 from the southern SCS (Jian et al. 2008). Also shown are interstadial events (2 to 23), Heinrich events (H1 to H61) and the Younger Dryas (YD) or similar events (*gray bars*)

Atlantic (Fig. 5.8). A good match between the Mg/Ca SST record and the benthic $\delta^{18}O$ from the same site also implies that the demise of ice sheets during the last deglaciation did not precede Northern Hemisphere summer insolation increase (Oppo and Sun 2005).

The outlined SST changes are confirmed by our new Mg/Ca-derived SST record from core 17961 in the southern SCS (Fig. 5.9). During the last deglaciation, SST changes were apparently synchronous with changes in both benthic (*C. wuellerstorfi*) and planktonic (*G. ruber*) $\delta^{18}O$, without any noticeable phase lead or lag between them (Jian et al. 2008). Together with the recent published SST records (Kienast et al. 2001; Oppo and Sun 2005), our new data support the inference that, in the East Asian monsoon region, tropical SST changes during the last deglaciation were synchronous with warming events in Greenland. These SCS records are in conflict with postulates from the equatorial western Pacific Ocean (Lea et al. 2000; Visser et al. 2003), although the SCS, particularly its southern part, belongs to the tropical Pacific. Therefore, the precise phase relationship between tropical and high-latitude climates during past abrupt climate events require further studies on higher time resolution before these inconsistencies can be resolved.

Paleo-SST Patterns

Paleo-SST in the SCS

As described in Chapter 2, the modern SST distribution in the SCS is largely controlled by the seasonally reversing monsoon-driven surface circulation. With the seasonal alternation of prevailing winds, i.e. the southwest monsoon in summer and northeast monsoon in winter, the SCS displays a trans-basinal pattern of surface currents with opposite directions during summer and winter. In summer, surface

water of the tropical Indian Ocean flows northward into the SCS, while in winter the northeast wind drives the tropical and subtropical Pacific waters together with the cooler coastal waters into the SCS, leading to a steeper south-north (S-N) temperature gradient in the winter SCS. According to Levitus and Boyer (1994), the SST of the SCS ranges from 22 to 28.8 °C during winter, with steep gradients toward the coast of China, while during summer, the SST varies only between 27 and 29 °C.

During the LGM, however, when sea level dropped by 100–120 m, all the southern connections to the open ocean closed, and the SCS changed to a semi-closed basin with Bashi Strait as its only water passage way to the open ocean. Winter and summer SST estimates for the LGM from ten cores (Fig. 5.10) show distinct S-N contrast (Wang P. et al. 1995). The winter SST displayed a south-north (S-N) trend, from 17.5 °C in the north to 23 °C in the south, whereas the summer SST showed

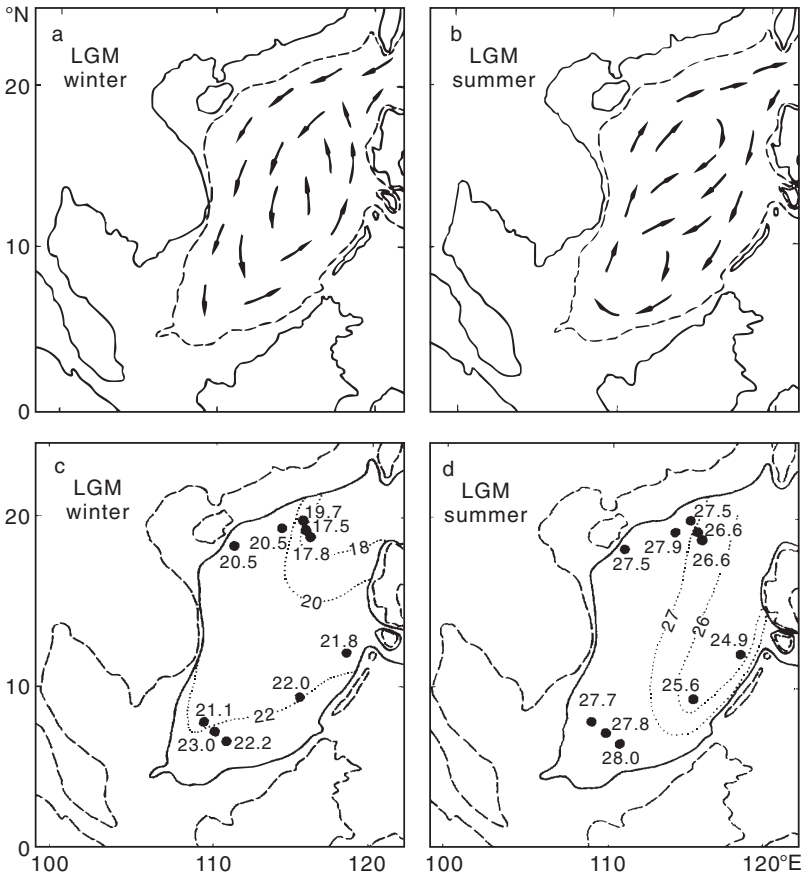

Fig. 5.10 Surface circulation (**a**, winter; **b**, summer) and average SST (**c**, winter; **d**, summer) in the SCS during the LGM show different distribution patterns (Wang P. et al. 1995). *Dotted lines* denote isotherms (°C). Filled circles with numbers indicate the position of cores and average SST during the LGM, respectively

an east-west trend, from <25 °C in the east to 27–28 °C in the west, indicating basic changes in surface circulation.

These SST patterns during the LGM are also supported by numerical simulations. As shown in Fig. 5.10, when sea level was low, the glacial surface circulation was counter-clockwise for winter and basically clockwise for summer. Therefore, the earlier interglacial (and postglacial) trans-basinal patters of circulation must have been replaced by semi-enclosed patterns as schematically shown in Fig. 5.10 (Wang P. et al. 1995).

North-South Comparison of SST

The S-N temperature gradient in the winter SCS seems to exist throughout the entire Quaternary and can be used to indicate changes in the strength of the East Asian winter monsoon. Reconstructions of SST at ODP Sites 1146 and 1143 reveal increased SST gradient between the northern and southern SCS during glacials of the late Pleistocene due to strengthened winter monsoon, consistent with other winter monsoon proxy records (Fig. 5.11). For example, the S-N SST difference (ΔSST) between core 17964 (112°12.8′E, 06°09.5′N) from the south and core 17940 (117°23.0′E, 20°07.0′N) from the north displays increased values during the last glacial stage and decreased values during the Holocene, respectively, indicating intervals of strengthened and weakened winter monsoons (Fig. 5.12).

The SST estimates in cores 17940 and 17964 are based on planktonic foraminiferal transfer function and possibly biased by age control and ecological effects. Recently, Oppo and Sun (2005) published the first SST record based on Mg/Ca ratio measurements at ODP Site 1145. This northern SCS record is compared with a southern SCS record in core 17961 (112°19.9′E, 08°30.4′) derived also from the Mg/Ca ratio (Jian et al. 2008). The S-N SST and planktonic $\delta^{18}O$ differences between Site 1145 and core 17961 were calculated after interpolating the two sets of data to 1 kyr interval. The results show that the S-N SST gradient in the SCS fluctuated frequently, although the time resolution for the lower part of core 17961 is lower than that at Site 1145 (Fig. 5.13). Spectral analyses of the ΔSST reveal a precessional cycle ($\sim$23.2 kyr) and millennial variabilities mainly at 2.0–2.4 kyr and 1.4 kyr (Fig. 5.14). Particularly, during the D-O interstadials in the last glacial stage, the S-N SST differences decreased correspondingly, indicating weakened winter monsoons.

Paleo-SST in the Western Pacific

On the basis of micropaleontological data, the CLIMAP studies concluded that the "ice-age ocean was strikingly similar to the present ocean in at least one respect:

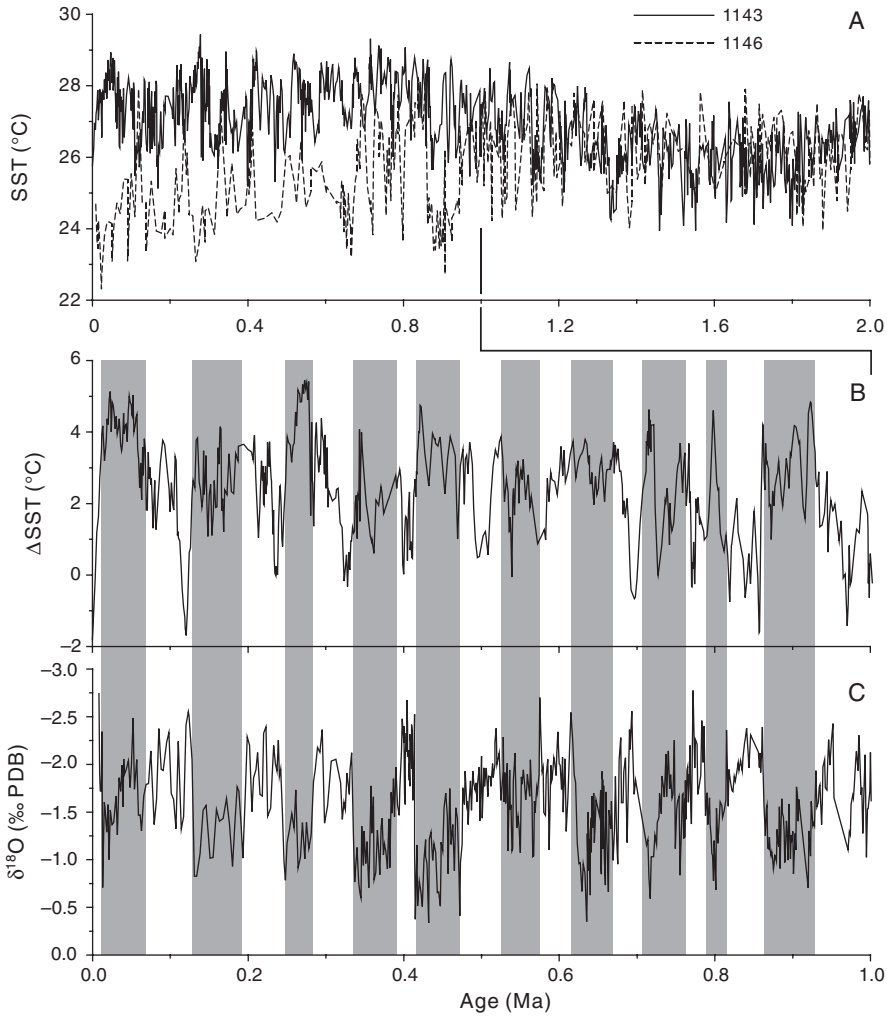

Fig. 5.11 SST variations are revealed at (**A**) the southern Site 1143 (*dashed line*, Xu et al. 2005) and the northern Site 1146 (*solid line*, Huang et al. 2003) derived from foraminiferal transfer function, (**B**) SST difference (ΔSST) between these two sites, and (C) *G. ruber* $\delta^{18}O$ at Site 1146. *Vertical gray bars* indicate glacial stages

large areas of the tropics and subtropics within all oceans had sea-surface temperature as warm as, or slightly warmer than, today" (CLIMAP 1981). Recent studies, however, have different conclusions (e.g., Hostetler et al. 2006).

Wang P. (1999) summarized the available paleo-SST data from the SCS and East China Sea, Sulu Sea and the adjacent western Pacific during the LGM, which were based on planktonic foraminiferal census using the transfer function FP-12E. As seen from Fig. 5.15, the LGM summer SST for the South China Sea and Sulu Sea

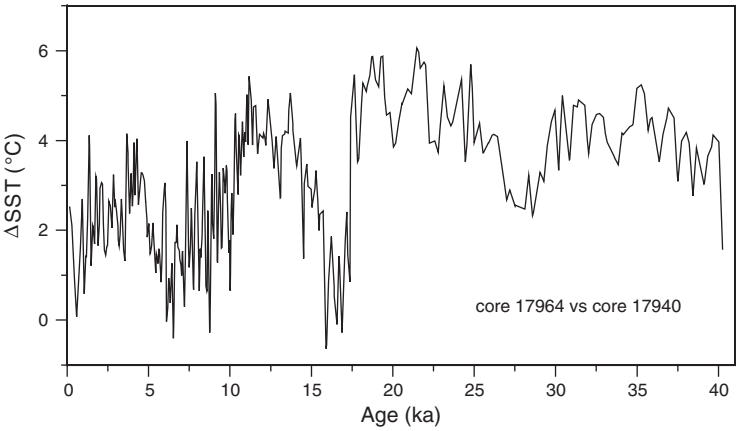

Fig. 5.12 S-N SST difference (ΔSST) between core 17964 from the southern and core 17940 (Pflaumann and Jian 1999) from the northern SCS was based on inferred SSTs using foraminiferal transfer function

between 5 and 20 °N ranges from 25.6 to 29.0 °C, averaging 27.8 °C, while in the open western Pacific at the same latitudes it ranges from 27.1 to 29.6 °C with an average of 28.7 °C. The LGM winter SST varies from 16.0 to 24.0 °C in the South China and Sulu Seas, averaging 21.1 °C, and from 23.8 to 28.0 °C in the open ocean, averaging 26.0 °C, or 4.9 °C higher than that in the marginal seas. Thus, the winter SST at the LGM was much cooler in the western Pacific marginal seas than in the open ocean, whereas in summer the SST was similar in the marginal seas and ocean, resulting in a much more intensive seasonality during the LGM in the marginal seas. In general, the winter SST at the LGM was at least 3–4 °C lower in the SCS and Sulu Sea than in the open Pacific, and the LGM seasonality is about 4 °C higher in the open ocean, supporting the early finding of the amplifying effect of glacial signals in the marginal seas (Wang and Wang 1990).

These different results of paleo-SST reconstructions led to new efforts to improve the paleoecological transfer function technique and to debate whether the technique is applicable to the whole tropics (Anderson and Webb 1994). Up to now, nearly ten cores in the SCS have been analyzed for $U^{K'}_{37}$ measurements, confirming LGM-Holocene SST contrast by 4–4.5 °C in the north and by 2.5 °C in the south (Huang et al. 1997a; Pelejero et al. 1999a; Kienast et al. 2001; Zhao et al. 2006), all slightly exceeding that in the open Pacific (Lea et al. 2000).

Oxygen isotope data for the late Quaternary are now available from many sites in the western Pacific marginal seas, in particular the SCS. As seen from LGM-Holocene changes in the $\delta^{18}O$ of shallow-dwelling planktonic foraminifers (*G. sacculifer* or *G. ruber*) (Fig. 5.15d), the $\delta^{18}O$ contrast is again much more significant in the marginal seas than in the open ocean, with $<1.7‰$ in the open ocean south of 30 °N but $>1.7‰$ in the marginal seas at the same latitudes. Although the greater $\delta^{18}O$ difference in the marginal seas might be partly caused by salinity changes and

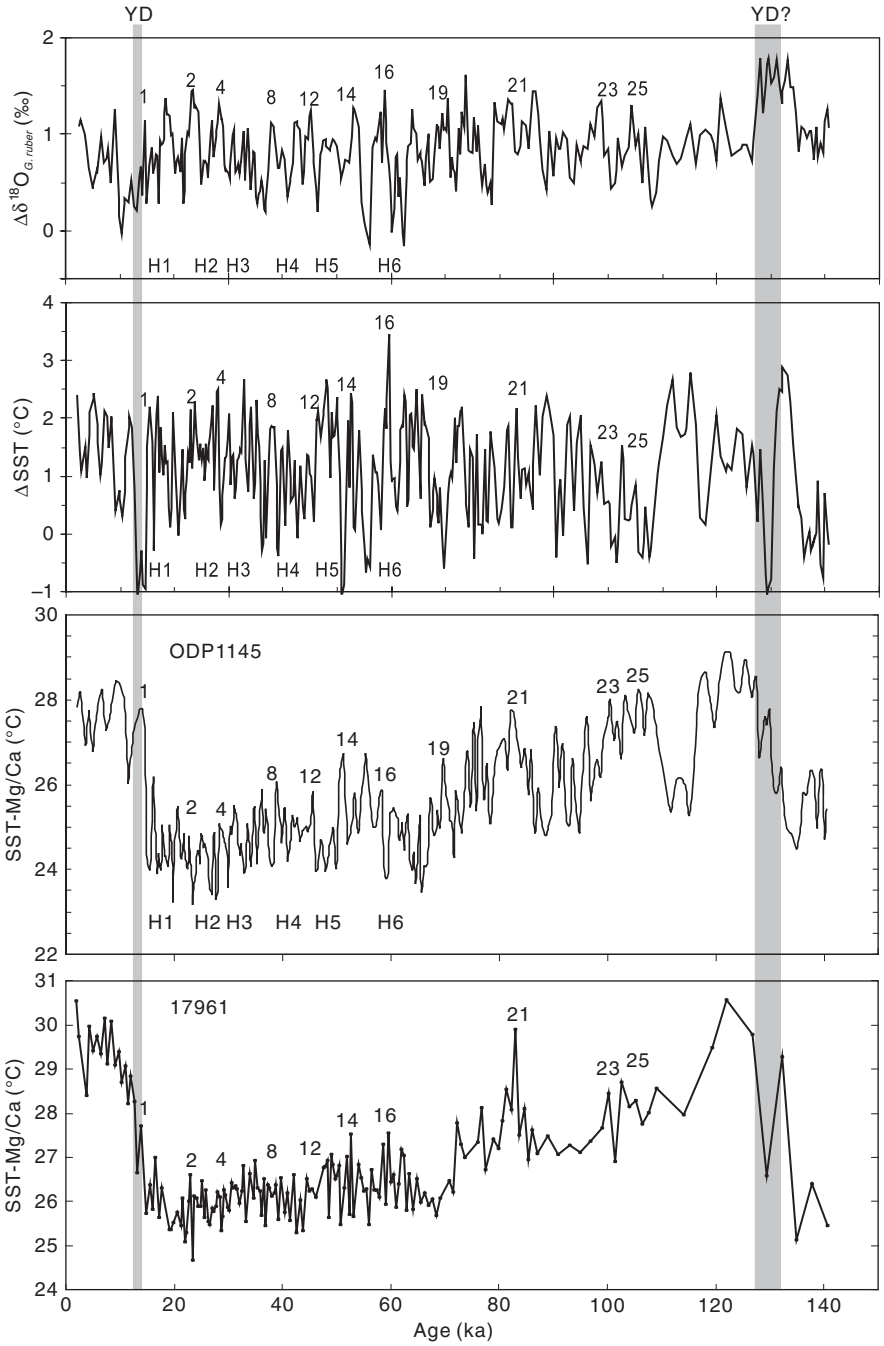

Fig. 5.13 S-N differences are shown in SST (ΔSST) and *G. ruber* $\delta^{18}O$ ($\Delta\delta^{18}O_{G.\ ruber}$) between cores 17961 from the southern (Jian et al. 2008) and ODP Site 1145 from the northern SCS (Oppo and Sun 2005). *Gray bars* show the Younger Dryas (YD) or similar events. Numbers denote the D-O events, and H1 to H6 indicate Heinrich events

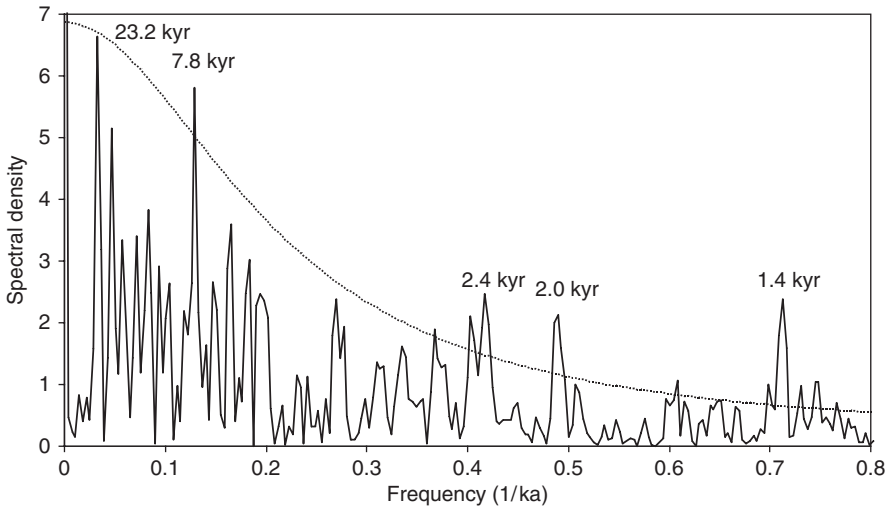

Fig. 5.14 Results of spectral analyses on the S-N SST difference (ΔSST) between core 17961 and Site 1145 reveal several precessional and millennial periods (numbers) exceeding the upper limit of red noise at 90% confidence level (*dotted line*)

in part controlled by sedimentation rates and bioturbation, there is no contradiction between the $\delta^{18}O$ data and the trend of paleo-SST change discussed above (Wang P. 1999).

5.2 Thermocline Depth History (Tian J. and Jian Z.)

The upper-water structure, particularly the thermocline depth, is of particular importance for the low-latitude Pacific and the SCS because of its close ties with El Nino-Southern Oscillation and with the East Asian monsoon. Therefore, past thermocline changes in the SCS can shed light on the history of both the East Asian monsoon (Jian et al. 2000a; Huang et al. 2002; Tian et al. 2005b) and the Western Pacific Warm Pool (Li B. et al. 2004; Li Q. et al. 2006). Seasonal variations of thermocline depth in the modern SCS are discussed in Chapter 2 (Thermocline and upwelling), here we review the history of thermocline depth changes starting from its proxies.

Proxies of Thermocline Depth

Foraminiferal Assemblage

Planktonic foraminiferal assemblages, transfer functions, and $\delta^{18}O$ gradient between surface and sub-surface planktonic foraminifers have been applied for reconstructing past thermocline changes in the SCS. Quantitative analyses of the modern planktonic foraminiferal distribution indicate that shallow dwelling species such as

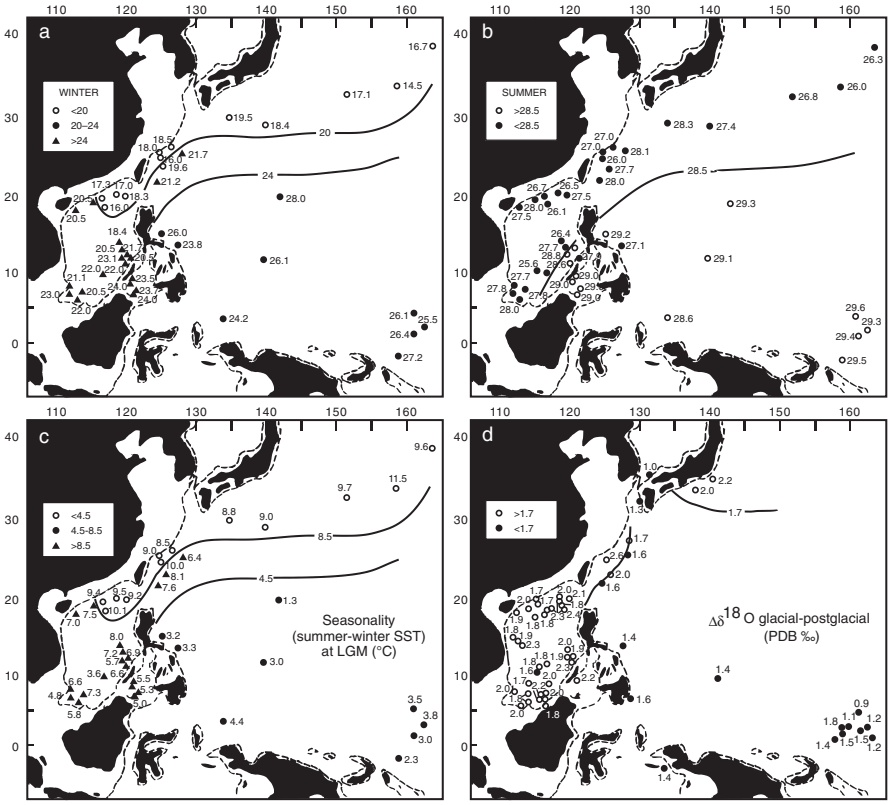

Fig. 5.15 SST estimates in cores from the low- and mid-latitude western Pacific and marginal seas at the LGM based on transfer function FP-12E show variations in (**a**) winter SST, (**b**) summer SST and (**c**) seasonality in SST (summer SST minus winter SST), as compared with (**d**) LGM-Holocene planktonic $\delta^{18}O$ differences (Wang P. 1999)

G. ruber and *G. sacculifer* dominate the assemblage when the surface mixed layer is deep and the thermocline is depressed to below the photic zone, and vice versa for the deep thermocline dwelling species such as *P. obliquiloculata* and *Globorotalia tumida* (Bé et al. 1985; Ravelo and Fairbanks 1992; Jian et al. 2000a). The vertical depth habitats of tropical planktonic foraminifers provide a primary tool for reconstructing upper water structure in paleo-oceans (Fairbanks et al. 1982; Thunell et al. 1983; Bé et al. 1985), so paleo-thermocline depth can be reconstructed either using the abundance ratio between shallow and deep dwelling species or transfer functions, as in the case of SST reconstruction. While the former may indicate relative changes, the latter provides quantitative estimates of the thermocline depth. In the tropical Pacific Ocean, two transfer function techniques, the Imbrie-Kipp Method (IKM) (Imbrie and Kipp 1971) and the modern analog technique (MAT) (Hutson 1980) have been widely used and the results show that subsurface

hydrography of the tropical Pacific during the LGM was only slightly different from the present-day's structure there (Andreasen and Ravelo 1997).

$\delta^{18}O$ Gradient Between Surface and Subsurface Planktonic Foraminifera

Another useful proxy of the paleo-thermocline depth in the western Pacific is the $\delta^{18}O$ difference between surface and subsurface dwelling planktonic foraminiferal species (Ravelo and Shackleton 1995; Jian et al. 2001). Larger $\delta^{18}O$ differences between subsurface and surface species usually indicate a shallow thermocline with a large temperature range in the photic zone with colder intermediate waters getting close to the surface, whereas smaller $\delta^{18}O$ differences often result from a deepened thermocline with a narrow temperature range (Ravelo and Shackleton 1995). For example, in the modern tropical Pacific, the thermocline is deep in the west but shallow in the east. The subsurface to surface foraminiferal $\delta^{18}O$ differences in core top samples are smaller (1.0‰) in the western Pacific but larger (1.9‰) in the eastern Pacific, corresponding to the deep and shallow thermoclines in these two Pacific sectors, respectively (Billups et al. 1999). Similarly, in the equatorial Atlantic the subsurface to surface foraminiferal $\delta^{18}O$ differences in core top samples are smaller (0.9‰) in the west with a deep thermocline but larger (1.4‰) in the east with a shallow thermocline (Billups et al. 1999). By using $\delta^{18}O$ differences between the subsurface *G. tumida* and the near-surface dwelling species *G. sacculifer*, Billups et al. (1999) constructed the upper ocean thermal gradient variations at the open west Pacific ODP Site 806 between 5 and 3 Ma. The consistently small $\delta^{18}O$ differences led the authors to suggest that the thermal gradient in the photic zone remained small and the mixed layer remained deep during the early Pliocene at Site 806.

The same has been observed in the modern SCS. As shown in Fig. 5.16, the core top $\delta^{18}O$ differences ($\Delta\delta^{18}O_{(P\text{-}G)}$) between *P. obliquiloculata* and *G. ruber* in the southern SCS ranges from 0.76 to 1.38‰ in the summer monsoon upwelling area off Vietnam, but from 1.68 to 1.83‰ outside this area. Smaller $\delta^{18}O$ differences between subsurface and surface species mean shallower thermocline in the upwelling area (Tian et al. 2005b). Therefore, the $\delta^{18}O$ difference $\Delta\delta^{18}O_{(P\text{-}G)}$, can be used to indicate thermal gradient variations in the SCS, with large $\Delta\delta^{18}O_{(P\text{-}G)}$ values implying decreased mixed layer depth, and vice versa for smaller $\Delta\delta^{18}O_{(P\text{-}G)}$ values.

Paleo-Thermocline Depth

Thermocline Evolution on Tectonic Timescales Since the Late Miocene

Abundance variations of deep-dwelling planktonic foraminiferal species have been used to estimate relative thermocline changes in the tropical and subtropical Pacific (Kennett et al. 1985) as well as in the SCS. Based on the relative abundances of the total deep-dwelling species and such species groups as *Neogloboquadrina* spp., *Pulleniatina* spp., and *Globoquadrina dehiscens* at Sites 1143 and 1146, Li B. et al. (2004) revealed the relative thermocline evolution in the northern and southern SCS for the past 12 myr.

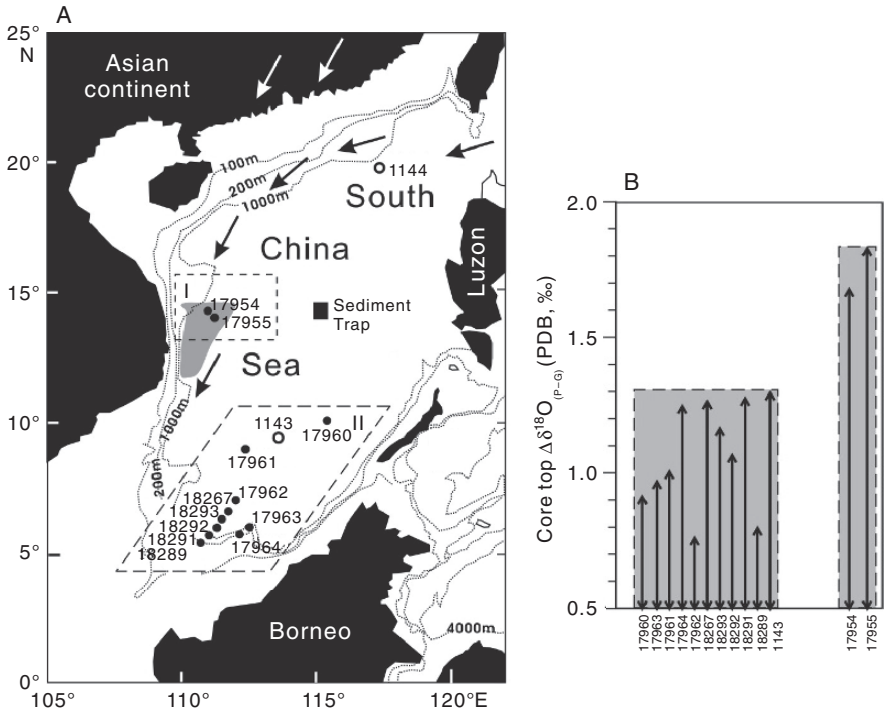

Fig. 5.16 $\delta^{18}O$ differences between subsurface-dwelling *P. obliquiloculata* and surface dwelling *G. ruber* ($\Delta\delta^{18}O_{(P\text{-}G)}$) (**B**) in core top samples can be used as an indicator of thermocline depth changes. (**A**) Locations of coretop sites (*black dots* = piston cores, *open circles* = drill holes). *Arrows* denote the direction of the East Asian winter monsoon wind and surface circulation. *Black solid square* denotes the location of the sediment trap in the central SCS. Cores 17954 and 17955 from summer upwelling region off Vietnam have larger $\Delta\delta^{18}O_{(P\text{-}G)}$ values (Tian et al. 2005b)

As shown in Fig. 5.17, a major decrease in the abundance of deep-dwelling planktonic foraminifera between 11 and 9 Ma at both sites, centered at 10 Ma, may indicate a deeper thermocline in the SCS after 10 Ma. Lower total abundances of deep-dwelling planktonic foraminiferal species from 10 to 8.2 Ma (Site 1143) and 8.58 Ma (Site 1146) suggest that a deeper thermocline persisted until 8.2 and 8.58 Ma in the southern and northern SCS, respectively. The thermocline in the western Pacific is 50–100 m deeper than in the eastern Pacific (Levitus and Boyer 1994). It has been suggested that the closure of the Indonesian Seaway played an important role in the early formation of the WPWP (Kennett et al. 1985). The closure of the Indonesian Seaway could have contributed greatly to WPWP evolution owing to the piling up of warm surface water in the western equatorial Pacific and the strengthening of the Equatorial Under Current (Maier-Reimer et al. 1990; Hirst and Godfrey 1993). Accordingly, the synchronous thermocline deepening at 10 Ma at sites 1143 and 1146 likely has been caused by initial formation of the WPWP due to the increased closure of the Indonesian Seaway in the early part of the late Miocene.

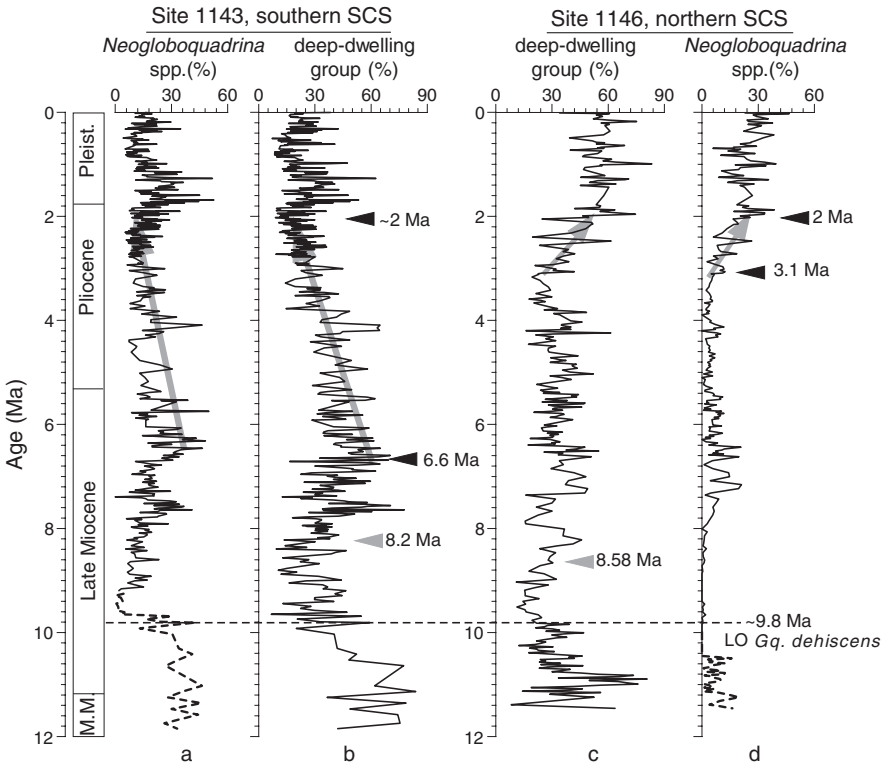

Fig. 5.17 Down-core variations of *Neogloboquadrina* spp. and total deep-dwelling planktonic foraminifera at Site 1143 (**a, b**) and Site 1146 (**c, d**) show different trends (Li B. et al. 2004). *Neogloboquadrina* spp. (*solid line*) includes *Neogloboquadrina dutertrei*, *Neogloboquadrina pachyderma*, *Neogloboquadrina humerosa*, and *Neogloboquadrina acostaensis*. *Dashed lines* indicate the abundance of *Globorotalia siakensis-Globorotalia mayeri* complex. M.M. = Middle Miocene; LO = last occurrence

Globoquadrina dehiscens was a typical subsurface species living mainly in warm temperate waters during the Miocene, which became extinct from the world oceans at 5.6 Ma near the Miocene/Pliocene boundary (Kennett et al. 1985; Berggren et al. 1995). In the SCS, however, the faunal data from Sites 1143 and 1146 show that the last occurrence (LO) of *Gq. dehiscens* at core depths of 470 m at Site 1143 and 412 m at Site 1146 corresponds to an age at ~9.8 Ma (Fig. 5.17). This event has also been reported from numerous petroleum wells on the northern shelf of the SCS, such as BY 7-1-1 (Qin 1996). The LO of *Gq. dehiscens* at these industrial sites is close to the zone N15/N16 boundary, and is accompanied by the first occurrences of *Neogloboquadrina acostaensis* and *Globorotalia merotumida*. The disappearance of *Gq. dehiscens* after 10 Ma from both the southern and northern parts of the SCS probably provides additional evidence for the initial development of the WPWP during the early part of the late Miocene (Li Q. et al. 2006). The pile up of warm

water during the formation of the WPWP probably eliminated the temperate water dwellers such as *Gq. dehiscens* that characterized the fauna before 10 Ma in the SCS.

At approximately 6.6 Ma the deep-dwelling planktonic foraminiferal species at Site 1143 constituted more than 60% of the total fauna, reflecting a shallower thermocline at that time. Later, it gradually decreased to the lowest abundance values of 10% at 2 Ma (Fig. 5.17b), a trend also observed in the *Neogloboquadrina* group (Fig. 5.17a). Site 1143 now lies within the modern WPWP, so thermocline variations at this locality should have responded to the warm pool development. These faunal decreases imply a thermocline deepening after 6.6 Ma in the southern SCS, probably related to the evolution of the western Pacific hydrography toward modern "warm pool" conditions after 6.6 Ma.

At Site 1146 in the northern SCS, the total deep dwelling species and species of *Neogloboquadrina* did not change significantly until 3.1 Ma (Fig. 5.17c and d). *Neogloboquadrina* spp. increased markedly over the 3.1–2.0 Ma period, from less than 10% to more than 20% of the fauna, and increased further to 30% in the Pleistocene. The total deep-dwelling species also increased from 25 to 55% over the same period, reaching the highest value of $>83\%$ at 1.0 Ma in the middle Pleistocene. These abundance increases at Site 1146 reflect a sudden shoaling of the thermocline after 3.1 Ma that continued into the Pleistocene in the northern SCS. These patterns contrast sharply with those at Site 1143, indicating that different controlling factors had been operating on the upper waters of the southern and northern parts of the SCS since the late Miocene. The faunal data from Site 1146 also suggest that the upper water conditions analogous to the modern northern SCS first occurred in the middle Pliocene. The shoaling thermocline from 3.1 to 2 Ma at Site 1146 thus indicates an intensified East Asian winter monsoon during that period, consistent with the eolian sediment records from central China (An et al. 2001).

Pleistocene Thermocline Variations on Orbital Scales in the Southern SCS

Transfer function derived thermocline change. Compared to the Neogene history discussed above, the Pleistocene thermocline depth can be estimated quantitatively using foraminiferal transfer function. The very deep dwelling species *Globorotalia truncatulinoides* has an unusual life cycle and is very useful in the reconstruction of the upper thermal structure. It reproduces at $\sim$600 m and from this depth juveniles rapidly travel to the surface then sink slowly through the water column, growing by adding chambers (Bé 1977; Bé et al. 1985; Hemleben et al. 1989). A higher proportion of this species probably indicate a very deep thermocline and/or thick mode water thermostads (Lohmann and Schweitzer 1990; Ravelo and Fairbanks 1992; Martinez 1994, 1997). In core 17957-2 from the southern SCS, the percentage abundance of *G. truncatulinoides* shows a trend of gradual decrease during the Brunhes chronozone which indicates water mixing and the depth of thermocline (DOT) gradually decreased (Fig. 5.18). Especially, the *G. truncatulinoides* left-coiling form, which requires a thermocline much deeper than the right-coiling form, and *Globoquadrina conglomerata* abruptly increased in MIS 5, indicating that the thermal structure of upper water column greatly changed during at that time.

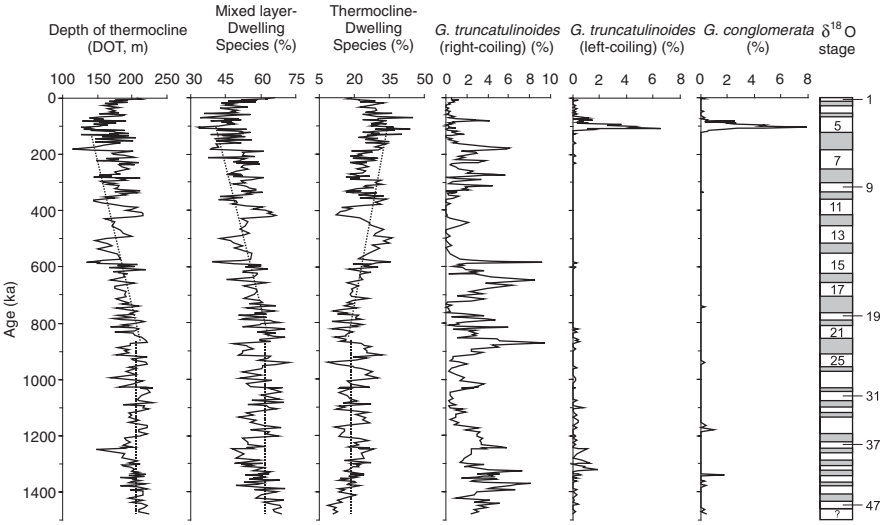

Fig. 5.18 Pleistocene thermocline history in the southern SCS is revealed in faunal proxies from core 17957-2, including the depth of thermocline (DOT) using transfer function of Andreasen and Ravelo (1997), relative abundance of mixed layer dwelling species, thermocline dwelling species, right-coiling and left-coiling *G. truncatulinoides*, and *Globoquadrina conglomerata*. Also indicated are marine isotope stages (numbers) and the general trends of changes before and after MIS 22 – 21 (*dashed lines*) (from Jian et al. 2000a)

The average Holocene DOT estimates in core 17957-2 is ~190 m, agreeing with the modern annual DOT derived from the world ocean atlas for this region (Levitus and Boyer 1994). The estimated downcore DOT ranges from 115 to 230 m, relatively deeper during interglacials than during glacials. Before MIS 22-21 or before the mid-Pleistocene revolution (MPR), DOT changed little around 200 m. Later it gradually decreased during the Brunhes chronozone, with an average of 180 m. The shallowest DOT of ~115 m occurred within MIS 6 before deepening again after abrupt increases in the *G. truncatulinoides* left-coiling form and in *G. conglomerata* during MIS 5.

In responding to DOT shoaling, the abundance of mixed layer dwelling species reduced while thermocline dwelling species increased (Ravelo et al. 1990; Ravelo and Fairbanks 1992). The mixed layer dwelling species in core 17957-2 decreased in abundance since the MPR and reached a minimum during MIS 6-5, while the thermocline dwelling species changed in an opposite trend (Fig. 5.18), reflecting a shoaling DOT, a phenomenon also observed in the western equatorial Pacific during the same time by the $\delta^{18}O$ difference between *G. sacculifer* and *P. obliquiloculata* (Schmidt et al. 1993).

However, the transfer function-derived DOT changes do not always display similar patterns of glacial/interglacial changes in different parts of the SCS. The prevailing monsoon system coupled with Ekman effect results in winter upwelling off the northwestern edge of the Philippines and summer upwelling along the Vietnam coast (Chapter 2). The winter upwelling region centered about 100 km

offshore between 16 and 19 °N off the northwestern Philippines had been revealed by the distributions of temperature, salinity and dissolved oxygen concentration, and also by the tracer distribution obtained from a numerical experiment (Chao et al. 1996; Shaw et al. 1996). The summer upwelling is also predicted from a climatology-driven circulation model in response to summer monsoonal winds (see Chapter 2). Late Quaternary records of monsoon-driven coastal upwelling can be highly promising for reconstructing the past thermocline changes and hence the East Asian monsoon variability. For example, shoaled thermocline and enhanced organic carbon flux have been inferred as result of intensified upwelling off eastern Vietnam during interglacials and off the northwestern Philippines during glacials (Jian et al. 2001; Fig. 5.19), showing a seesaw pattern of the DOT changes during

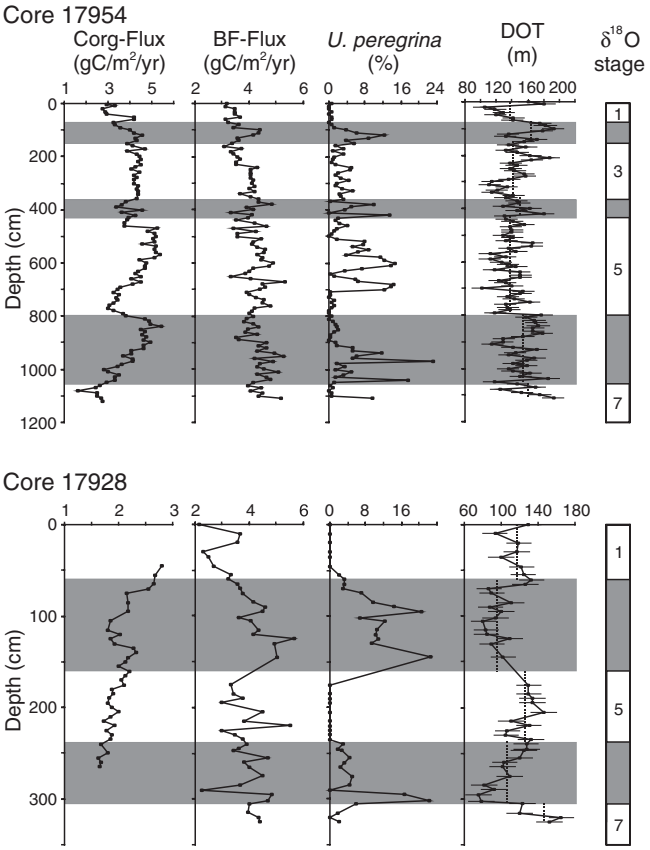

Fig. 5.19 Downcore variations in paleoproductivity indicators are compared between core 17954 off Vietnam and core 17928 off northwestern Luzon: C_{org}-Flux (organic carbon flux to the seafloor based on organic carbon content using the equation of Sarnthein et al. 1992), BF-flux (organic carbon flux to the seafloor based on the relative abundance data of benthic foraminifera using the technique of Kuhnt et al. 1999), the relative abundance of benthic foraminifer *Uvigerina peregrina* indicative of high organic carbon flux, and the depth of thermocline (DOT) with error *bars* (*short horizontal lines*) and average DOT for each MIS (from Jian et al. 2001)

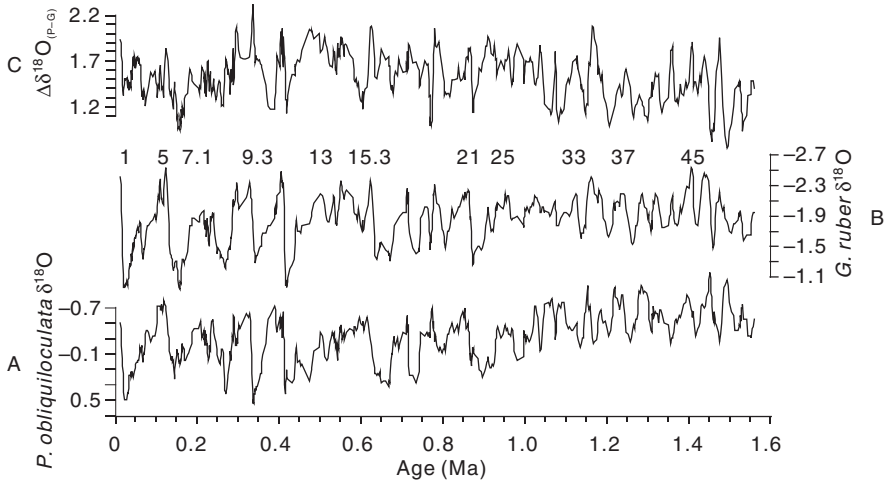

Fig. 5.20 Last 1.56 myr $\delta^{18}O$ records at ODP Site 1143 from the southern SCS after 3-point Gaussian smoothing show variations in the upper water structure: (**A**) $\delta^{18}O$ of *P. obliquiloculata* (PDB, ‰,), (**B**) *G. ruber* $\delta^{18}O$ (PDB, ‰), and (**C**) $\Delta\delta^{18}O_{(P-G)}$ (*P. obliquiloculata* $\delta^{18}O$ minus *G. ruber* $\delta^{18}O$) (PDB, ‰) (from Tian et al. 2005b)

glacial/interglacial cycles from the east to the west. The seasaw pattern of the DOT changes is probably unique to the SCS due to the monsoon influences in both summer and winter seasons.

$\delta^{18}O$ gradient derived thermocline change. An alternative way of thermocline reconstruction is by $\Delta\delta^{18}O_{(P-G)}$. Its values at ODP Site 1143 were reduced by 0.5–1.0‰ during glacials or stadials compared to the adjacent interglacials or interstadials, suggesting that the thermocline depth was deeper during glacial and stadial periods over the last 1.56 myr (Fig. 5.20) (Tian et al. 2004). On the contrary, during interglacial or interstadial periods, large $\Delta\delta^{18}O_{(P-G)}$ values imply a shallower thermocline. Exceptions to this general pattern are rare, including relatively high $\Delta\delta^{18}O_{(P-G)}$ values for MIS 16 and relatively low values for MIS 17 (Fig. 5.20).

However, the estimated DOT changes using these two methods show two opposite patterns for the early Pleistocene glacial/interglacial cycles in the southern SCS. The $\delta^{18}O$ gradient between *P. obliquiloculata* and *G. ruber* at Site 1143 exhibits deeper thermocline during glacials and shallower thermocline during interglacials throughout the Pleistocene (Fig. 5.20C), whereas transfer function derived DOT shows entirely different trends before and after the mid-Pleistocene revolution (MPR) around 0.9Ma mostly due to the abnormally high abundance of *P. obliquiloculata* in post-0.9 Ma glacial times. *P. obliquiloculata* is a typical thermocline dweller and its abundance heavily influences the accuracy of planktonic foraminiferal transfer functions. Its abundance shows higher values in interglacials before MPR but higher values in glacials after MPR in the southern SCS, such as at ODP Site 1143 (Xu et al. 2005), SONNE cores 17957-2 (Jian et al. 2000b) and 17962 (Fang et al.

2000). Although the transfer function techniques of Andreasen and Ravelo (1997) were successfully applied to reconstruct past thermocline depths in the open tropical Pacific, these techniques should be applied with caution in the southern SCS because of the potential no-analog behavior of planktonic foraminiferal species, especially of *P. obliquiloculata*.

Trans-Pacific Comparison and the Western Pacific Warm Pool

The upper ocean structure across the tropical Pacific is characterized by marked gradients of SST and thermocline depth, which are affected by ENSO (El Niño-Southern Oscillation) on different time scales. During normal conditions, the tropical eastern Pacific is bathed with cold surface water and a shallow thermocline, and the western Pacific with warm surface water and a deep thermocline. However, during El Niño years, the slopes of the seesaws of SST and thermocline across the equatorial Pacific were reduced, as a result of thermocline deepening and surface water warming in the east and thermocline shoaling and surface water cooling in the west. The SST records derived from the planktonic Mg/Ca ratio at ODP Site 806 in the west and at ODP Site 847 in the east well document the evolution of the trans-Pacific equatorial SST gradient over the last 5 myr and reveal permanent El Niño-like conditions in the late Pliocene period (Ravelo et al. 2004; Wara et al. 2005). The SST records show that the SST gradient across the equatorial Pacific was only 1.5 °C before ~2 Ma, very similar to the situation during a modern El Niño event. However, the SST gradient reached as high as 4–5 °C just after 2 Ma. In addition, the proxy records of thermocline changes using the planktonic $\delta^{18}O$ difference at ODP Site 847 reveal significant thermocline shoaling or water cooling in the eastern equatorial Pacific at ~3.5 Ma, much earlier than the abrupt increase in the SST gradient. Similar changes in planktonic $\delta^{18}O$ differences are also reported from ODP Site 851, another site from the eastern equatorial Pacific (Cannariato and Ravelo 1997).

The 28 °C isotherm, which constrains the northern boundary of the Western Pacific Warm Pool (WPWP), separates the SCS into two parts from the northeast to the southwest. The thermocline in the modern SCS shoals from ~175 m in the south to ~125 m in the north (Levitus and Boyer 1994), a seesaw pattern similar to that across the West and East Pacific. Variations in the relative abundances of the deep-dwelling planktonic foraminifera at ODP Site 1146 and at ODP Site 1143 reflect the evolution of the thermocline depth gradient across the northern and southern SCS since the late Miocene (Jian et al. 2006) (Fig. 5.21). The thermocline gradient between the northern and southern SCS probably enhanced for the first time during the 11.5–10.6 Ma, as indicated by an opposite change in the relative abundance of deep-dwelling planktonic foraminifera between Site 1146 and Site 1143. Between 10.6 and 4.0 Ma was a period with weakened thermocline gradient between the two sites. More significant increases in the thermocline gradient occurred at about 4.0–3.2 Ma, as marked by a jump in the abundance of deep-dwelling species at Site 1146 but a major decrease at Site 1143 (Jian et al. 2006). The faunal evidence of thermocline deepening from ODP Site 1143 at about

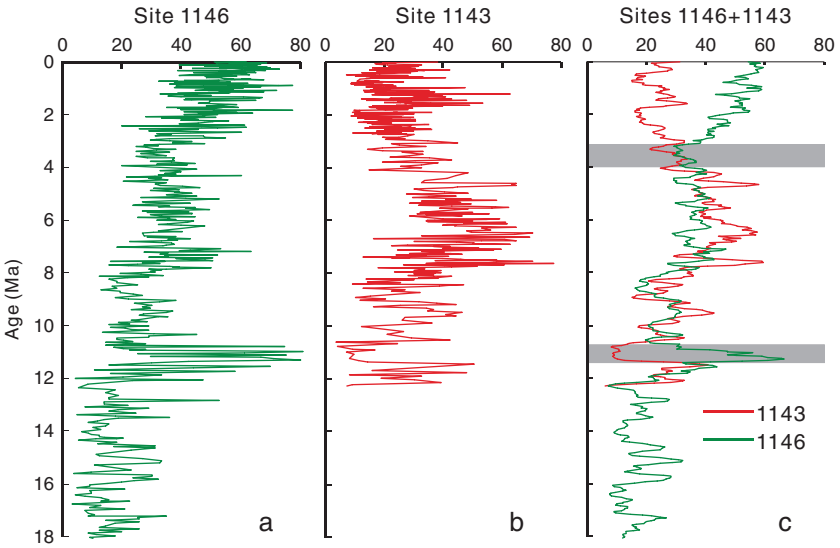

Fig. 5.21 Changes in the abundances (%) of planktonic foraminiferal deep-dwelling species at ODP Site 1146 (**a**) and Site 1146 (**b**) show increased south-north thermocline gradient (**c**, 5-point moving average) at ~11 Ma and since ~3 Ma (*horizontal bars*) in the SCS (Jian et al. 2006)

4.0–3.2 Ma matches well with the record thermocline shoaling in the east equatorial Pacific around ~3.5 Ma (Wara et al. 2005). The thermocline variations between the eastern and western equatorial Pacific reflect the long-term evolution of climate conditions in the pan-Pacific region. For example, the similarly decreased thermocline gradients across the east-west equatorial Pacific in the late Pliocene and in the modern El Niño years probably reflect the El Niño-like climate conditions during the late Pliocene and subsequent weakening. The development of a S-N thermocline gradient in the SCS since the Pliocene is comparable to the trans-Pacific east-west thermocline variations, indicating the long-term evolution of the WPWP.

5.3 Vegetation History in Deep-Sea Record (Sun X.)

Pollen grains in marine sediments are originating from vegetation on land and then buried in the sea after being transported by winds or currents. Deep-sea palynology yields terrestrial climate signals among the ocean records and bridges the paleoenvironmental studies across from land to sea. Pollen grains derived from the deep-sea, however, are typically transported over long distance and they integrate palynological information over a large area. Therefore, the use of pollen as climate and vegetation proxy depends on adequate knowledge of its modern distribution. A

survey of modern pollen in surface sediments is a prerequisite for paleoenvironment interpretation of the SCS sediment records.

Pollen Distribution in Surface Sediments

A total of 40 surface sediment samples from the SCS were investigated for pollen (Fig. 5.22) (Sun et al. 1999). The results are calculated and summarized by isopoll maps of pollen concentration (grains/g) and pollen percentage, which display distribution patterns of different pollen types related to their dispersal routes and mechanisms in the SCS. The concentrations of total pollen, total tree pollen, pine and fern spores bear very similar distribution patterns. Their highest concentrations occur in the northern part of the SCS, adjacent to Taiwan and Bashi Straits and decrease towards southwest along the direction of winter monsoon and surface currents. Their concentration isopoll figures are stretched as a tongue, extending from the Bashi trait towards the southwest. This can be illustrated with *Pinus* concentration isopoll map (Fig. 5.22A), and is most likely resulting from the northeastern winter monsoon which brings the conifer pollen from the southeast part of mainland China and Taiwan to the sea before being transported further afield by surface currents (Sun et al. 1999). This interpretation is confirmed by the depositional process recorded by sedimentation traps in the northern SCS (Su and Wang 1994). On the other hand, pollen concentrations of tropical/subtropical trees and herbs are very low and their values decrease from the continental shelf to the deep sea, implying their dispersal from the coastal areas of south China and Taiwan mainly by river discharges (Fig. 5.22B).

The pollen concentrations in the southern SCS are much lower, only one tenth of those of the northern part, and decrease from the coastal areas of islands (mainly Borneo) to the deep-sea. This pollen distribution pattern indicates that the pollen source areas in the southern SCS are the islands east of the Sunda Shelf, mainly Borneo, and pollen grains reach there chiefly by river transport (Sun et al. 1999).

Pollen percentage results display that, along the continental shelves of the northern and southern SCS, the fern spores are the dominant component, respectively reaching 80% and 70% of total pollen and spores sum. The subdominant components are trees, reaching 40% in the northern, southern, and eastern margins of the SCS but diminishing seaward. Percentages of herb pollen are quite low, contributing less than 10% of the total in near 90% of samples.

Among tree pollen, *Pinus* is found to be prevalent in the surface sediments from the northern SCS, contributing 80% in most of samples, but it is only less than 10% in the southern SCS (Fig. 5.22C). Its maximal values of concentration occur in the northeast SCS and stretch as a saddle from NE to SW, being consistent with the direction of the NE winter monsoon and the surface current. Pollen of tropical and subtropical complex reaches 60% in the southern part, but only $<1\%$ in the north (Fig. 5.22D). Mangrove pollen is abundant in the southern part, reaching a maximum of 20%, but only $\sim 1\%$ in the northern part (Fig. 5.22E).

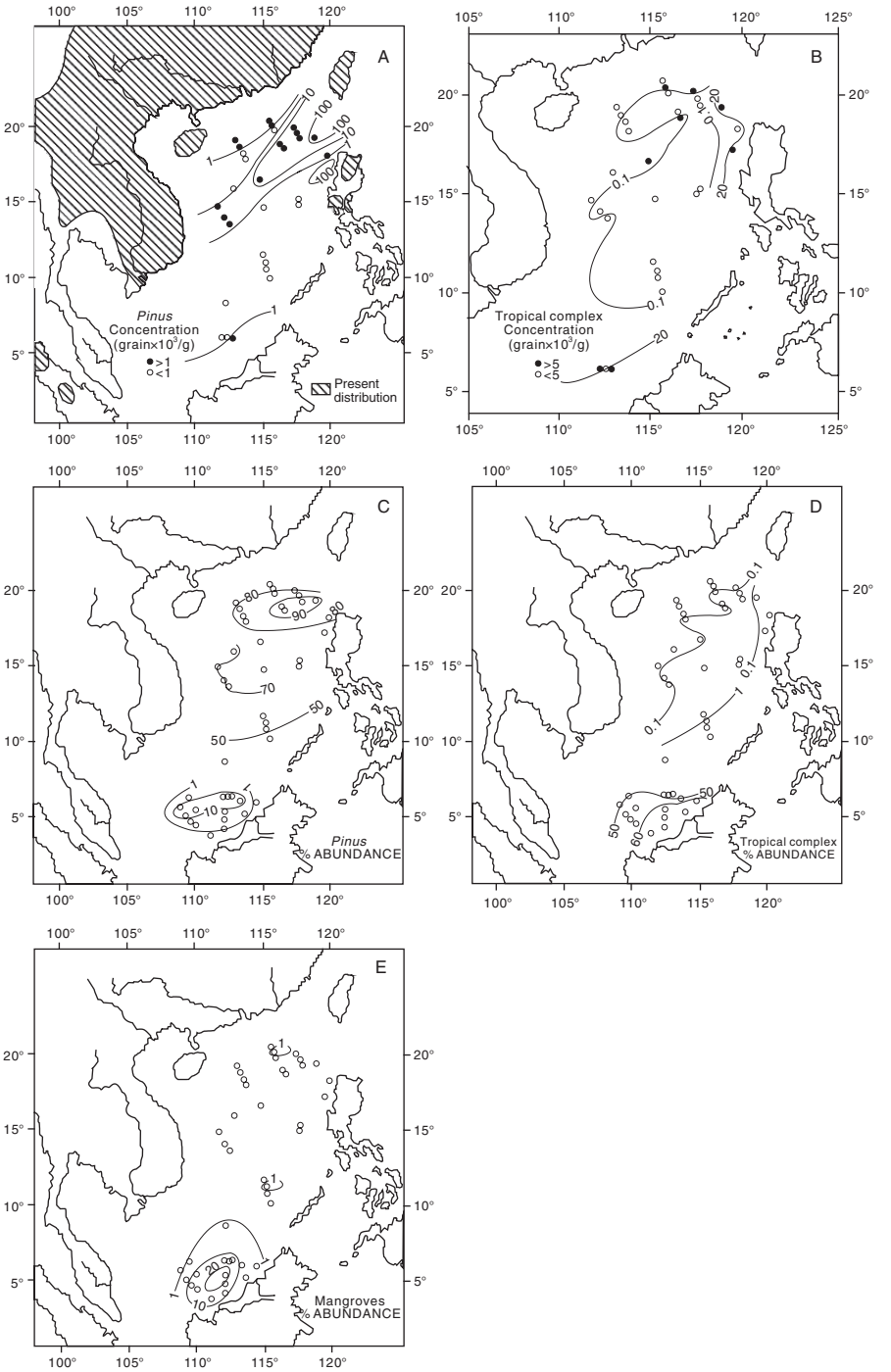

Fig. 5.22 Maps show concentration isopolls (10^3/g.dry sediment) and relative abundance isopoll (%) of (**A**) *Pinus* concentration, (**B**) tropical complex concentration, (**C**) *Pinus*%, (**D**) tropical complex %, and (**E**) mangroves% in the modern SCS (modified from Sun et al. 1999)

Long-Term Evolution

All of the pollen sequences discussed here were based on samples retrieved during cruises "Sonne 95" in 1994 (Sarnthein et al. 1994), "Sonne 115" in 1996 (Stattegger et al. 1997) and "ODP Leg 184" in 1999 (Wang P. et al. 2000) (see Table 5.1, Fig. 1.1). Of those only the ODP cores enabled us to study the long-term vegetation history before the late Pleistocene. Because of the extremely low pollen concentrations in a number of stratigraphic intervals, only the early-to-middle Oligocene, late Miocene-Pliocene, and Pleistocene pollen sequences are discussed here.

Oligocene

The longest deep-sea record from the SCS was recovered at ODP Site 1148 from the northern lower continental slope (at modern water depth of 3,294 m), but from the entire profile only the Oligocene section yielded sufficient quantity of pollen for a statistically meaningful study. As seen from Fig. 5.23, the Oligocene assemblage is dominated by montane conifer tree pollen. The broad-leave tree pollen groups include mainly tropical-subtropical components. A distinct change in pollen assemblage occurred at around 32.0 Ma when the temperate montane conifer and cool and drought-enduring deciduous tree taxa remarkably increased. Therefore, the pollen data suggest that tropical montane rainforest and lowland rainforest developed in the neighboring areas before 32.0 Ma, but the climate turned to be cooler and drier after 32.0 Ma. This climate change is well correlated with previous observations during oil exploration in the Zhujiangkou (Pearl River Mouth) Basin (Wu et al. 2003).

Noteworthy is the occurrence of abundant coastal and neritic dinoflagellate cysts together with the Oligocene pollen (Mao et al. 2007), which seem to be incompatible with the deep-water benthic fauna from the same samples (see Chapter 6). This unusual combination of coastal dinoflagellates with deepwater ostracoda and foraminifera is most probably associated with the narrow gulf shape of the early SCS basin at the early stage of seafloor spreading. Since then, the depth of the SCS basin increased during its further opening, as evidenced by the changes in benthic microfauna, accompanied by increased abundance of oceanic dinoflagellate species upward in the profile (Mao et al. 2007).

Late Miocene-Pliocene

The late Miocene-Pliocene pollen sequence is based on 380 samples from the depth interval of 76–512 mcd (meter composite depth) at ODP Site 1143, southern SCS. Four pollen zones are defined from the pollen diagrams (Fig. 5.24) (Luo and Sun 2007):

Table 5.1 Location, water depth, core length, chronology, sampling interval, time resolution and references of studied pollen sites are listed

Site	Location	Water Depth (m)	Core Length (m)	Age	No. of samples	Sampling Interval (cm)	Resolution (y)	Reference
ODP1144	20°3.18′N 117°23.0′E	2037	520	1.03 Ma	1250		820 (154–1160)	Sun and Luo 2001 Luo et al. 2001 Sun et al. 2003 Luo et al. 2005
17940	20°07′N 117°23.0′E	1727	13.30	37 ka	102	10	360	Sun and Li 1999 Sun et al. 1999 Sun et al. 2000b
ODP 1148	18°50′N 116°34′E	3294	850	33 Ma	169		43000	Wu et al. 2003 Mao et al. 2007
ODP1143	9°22′N 113°17′E	2772	510	~12 Ma	380	28–220	7000–52500	Luo and Sun 2007
17962	7°11′N 112°5′E	1970	8.0	30 ka	82	10	365	Sun et al. 2002
17964	06°09.5′N 112°2.8′E	1556	13.03	26 ka	62	20	420	Li and Sun 1999
18287	5°39′N 110°39′E	598	5.66	16.5 ^{14}C ka	112	5	120	Wang X. et al. 2007
18300	4°21′N 108°39′E	91	8.85	39.2 ^{14}C ka	52	20	800	Wang X. 2006
18302	4°09′N 108°34′E	83	5.98	20.16 ^{14}C ka	41	20	500	Wang X. 2006
18313	3°52′N 108°52′N	98	6.2	No record	12	40		Wang X. 2006
18323	2°47′N 107°53′E	92	5.4	31.27 ^{14}C ka	50	20	600	Wang X. 2006

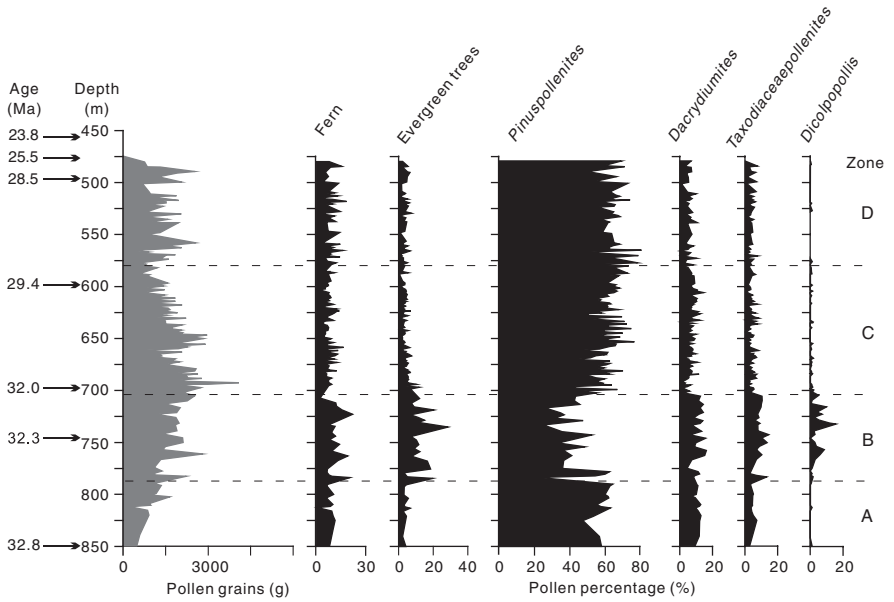

Fig. 5.23 Pollen concentration and percentage diagrams of selected palynomorph components in the Oligocene section of ODP Site 1148 show a major change at ~32 Ma (based on Wu et al. 2003)

P1 (521–413 mcd, 11.9–8.15 Ma) is characterized by very low pollen influx (48 grains/cm^2/kyr in average). *Pinus* (52.1%) is the dominant taxon, and the tropical lowland rainforest pollen (16.5%) comes second. The percentages of fern spores are very high, occupying 107.9% of the total land seed plants.

P2 (413–171 mcd, 8.15–4.29 Ma) is characterized by abruptly increased pollen influx (1648 grains/cm^2/kyr in average), which is nearly 35 times more than those in P1. Cool-tolerant pollen groups increased during this stage, at the cost of warm-tolerant groups. But pollen of the tropical lowland rainforest (6.5%) and fern spores (62.6%) dropped sharply.

P3 (171–122 mcd, 4.29–2.63 Ma) is characterized by decreased pollen influx (85 grains/cm^2/kyr) and dramatically increased fern spores (329.4%). During this stage, pollen of the temperate forest fell sharply (2.1%), and the mangrove pollen appeared in very low percentages.

P4 (122–76 mcd, 2.63–1.58 Ma) is characterized by a second rise in pollen influx (194 grains/cm^2/kyr) with strong fluctuations. The lowland rainforest pollen and especially the ferns (329.4%) increased in percentages. More mangrove pollen (1.3%) were found during this stage.

A distinct boundary occurs at 8.1 Ma when pollen influx values increased abruptly. The cool-tolerant montane and temperate groups also increased while percentages of tropical lowland group and fern declined. These dramatic changes in pollen influx presumably resulted from exposure of the Sunda Shelf from 8.1 to 4.3 Ma because of the sea level drop.

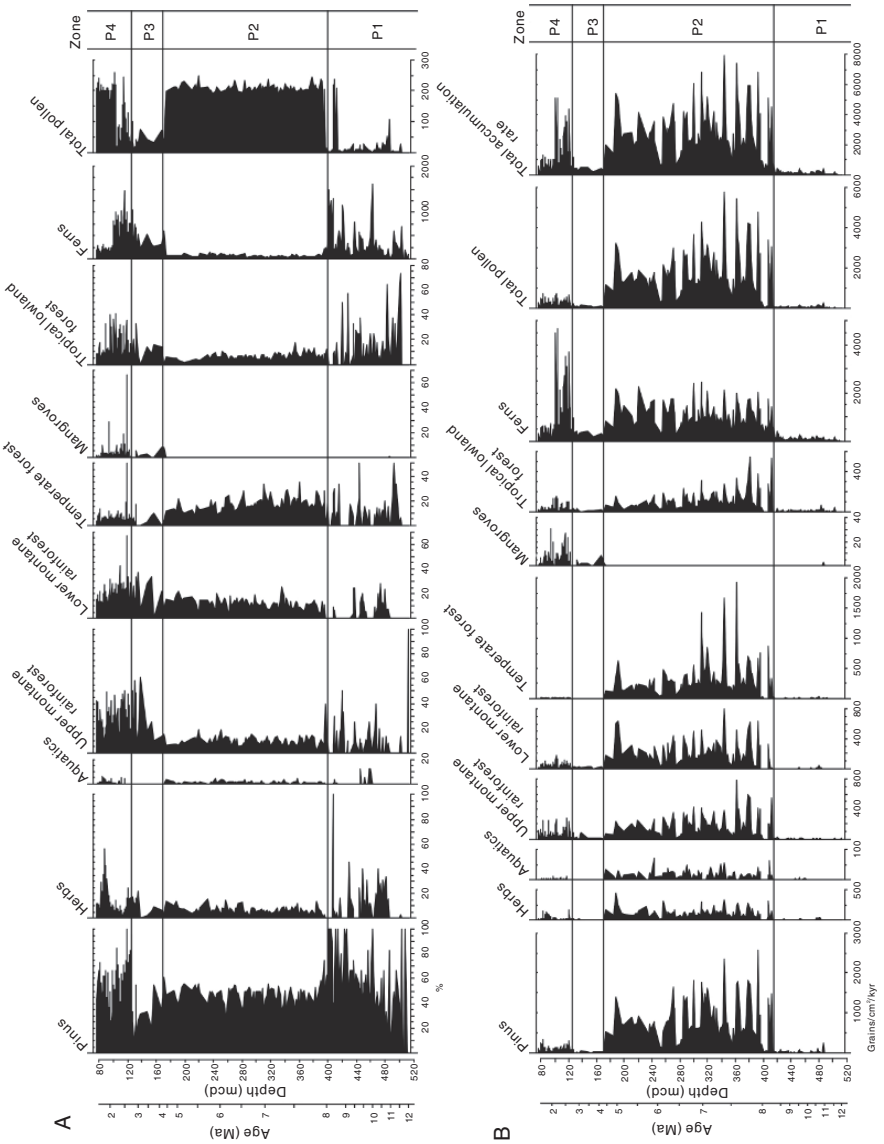

Fig. 5.24 (continued)

The increase of cool-tolerant group probably indicates a climate cooling since ~8 Ma, in consistent with loess sequence results and other records. The loess records demonstrate a massive eolian deposition since 7–8 Ma, implying arid climate and desert environment developed in the late Miocene (Sun and An 2001). The terrestrial pollen records demonstrate that a bloom of grass vegetation occurred during time intervals of 8.5–6.0 Ma in the Jiuxi Basin (Ma et al. 2004), 8.6–8.4 Ma and 6.9–6.6 Ma in the Linxia Basin (Ma et al. 1998) from the northwestern China, indicating dry and cold climate. The pollen influx at Site 1143 decreased from 4.3 to 2.6 Ma, probably related to sea level rise and submergence of the Sunda Shelf. Since ~2.6 Ma, the pollen influx increased again and fluctuated in a wide range. A rough comparison of pollen influx values with $\delta^{18}O$ data indicates that the time intervals with high influx values correspond to glacial periods with heavy $\delta^{18}O$ values and the low influx values are correlated with interglacial periods with lighter $\delta^{18}O$ values (Luo and Sun 2007).

Pleistocene

The best palynological record of the Pleistocene in the SCS is from ODP Site 1144, northern SCS. It provides a long pollen sequence spanning the past 1.3 myr, with an average time resolution of about 820 years. A total of 1250 pollen samples were analyzed for the 504 m long sequence. Chronology of the sequence is based on micropaleontology and magnetostratigraphy (Wang P. et al. 2000), as well as the $\delta^{18}O$ record of *G. ruber* (Bühring et al. 2001). Sediments of the profile are almost continuous except for a hiatus at 196.64 m where MIS 8 is almost completely missing, and two short-term hiatuses respectively within MIS 5.5 and MIS 11.31. Often, lighter $\delta^{18}O$ stages are correlated to pine-dominant pollen zones assigned to interglacials, and heavier $\delta^{18}O$ stages correspond to herb-predominant pollen zones belonging to glacials. On this basis, a total of 29 pollen zones have been recognized which almost completely coincide with isotopic stages MISs 1–29 (Fig. 5.25).

A total of 174 pollen types have been identified, but except for pine and some herbs, most of the pollen types contain very few grains, in particular for some tropical and subtropical taxa (Fig. 5.26). *Pinus* pollen dominates pollen assemblages throughout the profile, followed by herbs in percentages. These two types together can reach up to 80% of the total pollen sum of land seed plants, though the downcore variations are very significant. *Pinus* almost always shows higher percentages in the interglacial (varying from 39 to 81%) than in the adjacent glacial stage (30–54%). Herbs pollen includes 29 pollen components, with the most important components from *Artemisia*, Poaceae and Cyperaceae. Pollen from Chenopodiaceae and other Asteraceae are moderate, and all other taxa are very low in percentage. In contrast

←

Fig. 5.24 Late Miocene–Pliocene pollen diagrams (**A**, pollen percentages; **B**, pollen influx) from ODP Site 1143 can be divided into 4 pollen zones, indicating major changes at 8.1, 4.3 and ~2.6 Ma (from Luo and Sun 2007). Pollen percentages are based on total pollen numbers of seed land plants, while pollen influx represents numbers of pollen grains/cm^2/kyr

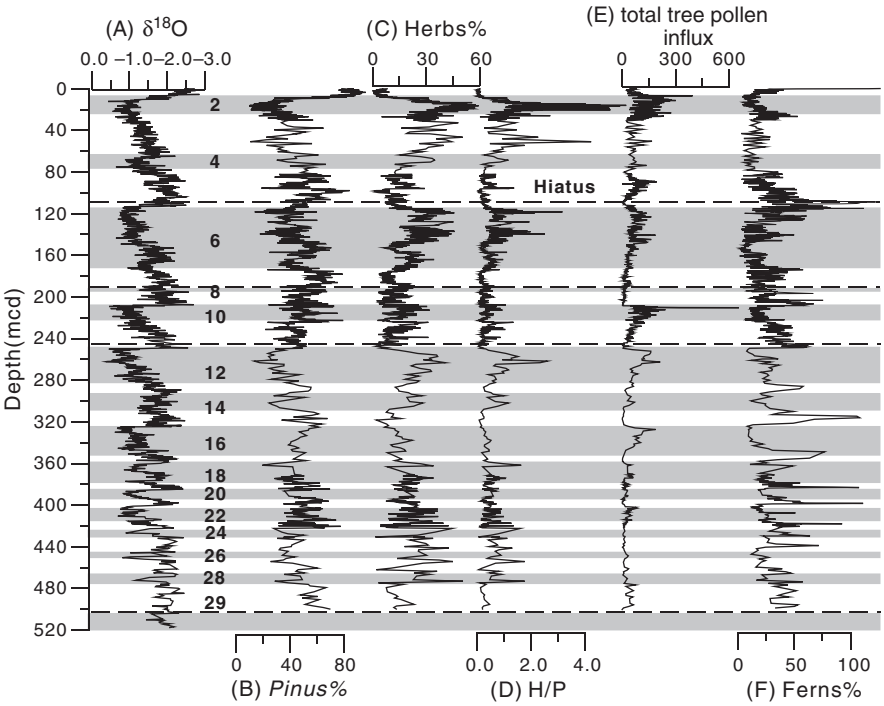

Fig. 5.25 Glacial/interglacial contrasts in pollen assemblages (B to F) are compared to *G. ruber* $\delta^{18}O$ record (A) at ODP Site 1144, northern SCS (from Sun et al. 2003). Numbers denote the marine isotope stages. Dashed horizontal lines mark the presence of hiatus

to *Pinus*, the percentages of herbs and their main taxa are low during interglacial periods (4.9–25.5%), but considerably higher during glacials (12.8–32.7%) (Sun et al. 2003).

The tropical and subtropical group includes a large number of taxa, but only a few grains of each taxon can be encountered per sample, except *Quercus* (evergreen type). This group ranks third, inferior to *Pinus* and herbs in pollen percentages, and ranges from 6.3 to 20%. No distinct glacial/interglacial variations in its percentage can be found, although the middle part of the profile (from MIS 19 to 12) bears

Fig. 5.26 Pollen diagram of ecological groups and selected taxa from ODP Site 1144 are shown by (**A**) pollen percentages, calculated on the total pollen sum of land seed plants, and (**B**) pollen influx (grains/cm^2/yr) (from Sun et al. 2003). Ecological groups shown in the figure are: Herbs (*Artemisia*, Poaceae and Cyperaceae as the main components, with sparse Asteraceae, Chenopodiaceae etc.); Boreal conifers (*Picea, Abies*, and *Tsuga*); Tropical upper mountain group (*Podocarpus, Dacrycarpus, Dacrydium* and *Phyllocladus*); Temperate deciduous group (*Betula, Alnus, Carpinus, Juglans, Ulmus* etc.); Tropical and subtropical evergreen group (*Quercus*, *Altingia, Ilex, Castanopsis/Lithocarpus, Mallotus/Macaranga*, Euphorbiaceae, Palmae, Melastomataceae, Meliaceae, Euphorbiaceae, Moraceae); Mangroves (mainly *Rhizophora* and *Sonneratia*) and Aquatics (*Typha, Myriophyllum, Nymphoides*)

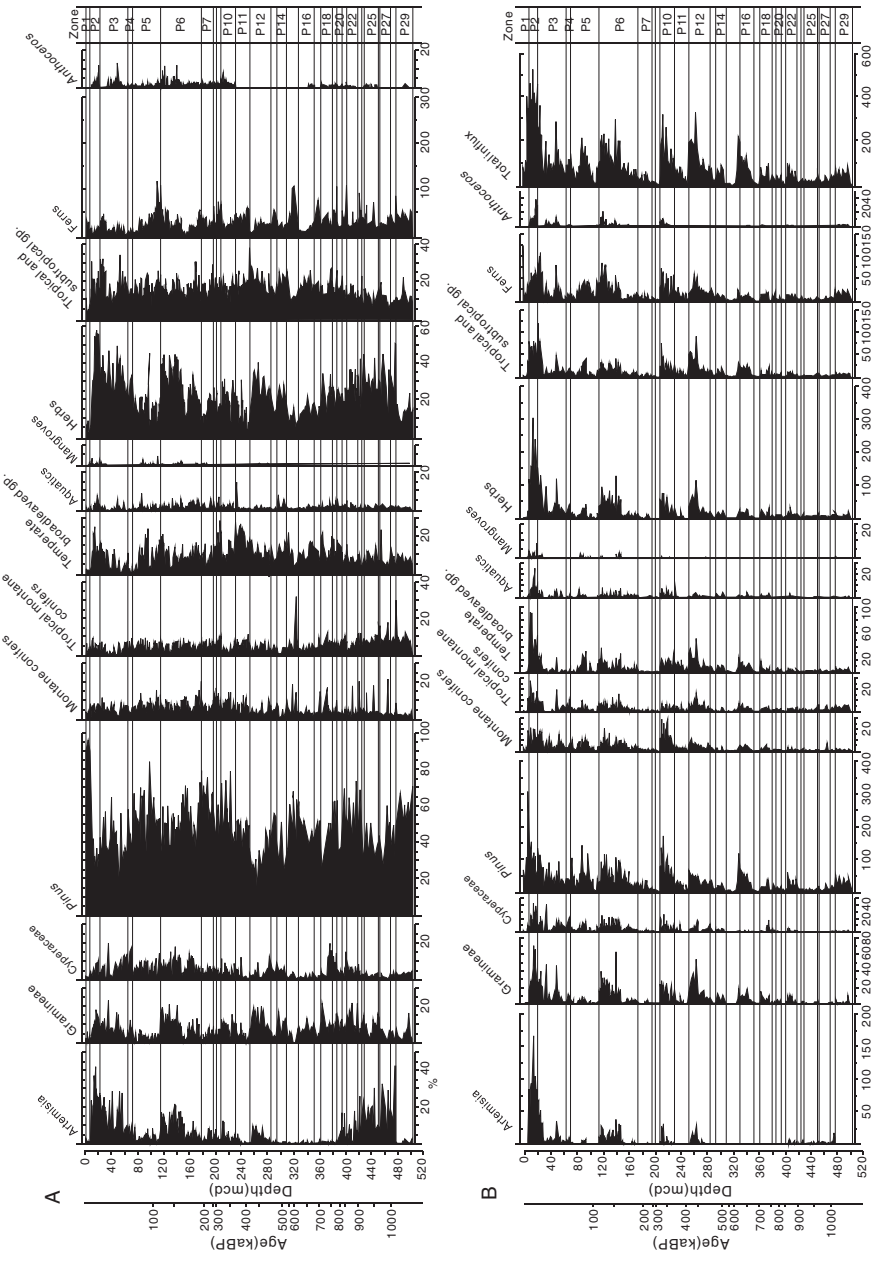

Fig. 5.26 (continued)

higher percentages than the upper and lower parts. Mangroves, of which *Rhizophora* is the most important, is very low in percentage, ranging from 0 to 0.3%. Mangrove pollen is almost completely absent before MIS 12, occur only in trace numbers since MIS 12, but increase to maximum values in the LGM and the Holocene (MIS 2 and 1). *Anthoceros*, the dwarf liverwort genus is also recorded, with insignificant numbers in interglacial intervals. Aquatic plants occur in low proportions (less than 2%) throughout the profile. Fern spores are found in large numbers ranging from 11.7 to 58.2% of total land seed plants and represent a variety of types with spores of *Cyathea* and *Gleichenia* dominating. Generally, fern spores are more frequent in interglacials, and achieve highest percentages in MIS 1, 5e and 15 (Fig. 5.26A).

Pollen influx (Fig. 5.26B) is expressed as numbers of pollen grains accumulated on one square centimeter during one year. In general, influx values of total pollen and pollen of each ecological group or taxon are very low (4 grains/cm^2/yr) in the lower part of the profile (from the bottom of the profile to MIS 17), then begin to increase upward and reach the maximum (864 grains/cm^2/yr) in MIS 2 (LGM). The range of pollen influx variations can exceed two orders of magnitude (Fig. 5.26B). In addition, the influx values of total pollen and pollen of each ecological group or taxon are clearly greater in glacials than those in neighboring interglacials.

The pollen sequence at Site 1144 provides a vegetation and monsoon history of the Pleistocene. During interglacials, low amounts of pollen are found in the sediments, particularly from tropical/subtropical plants and herbs, thereby providing very limited information about the terrestrial vegetation. In contrast, a large amount of pollen in glacial sediments at Site 1144 could have been brought in by a strengthened northeast winter monsoon from the Asian mainland and Taiwan Island. In addition, pollen grains could also have been transported from the exposed continental shelf by water flow and wind at glacial sea-level lowstands (Sun et al. 2003).

Pollen assemblages at Site 1144 have revealed the changes in evergreen forest composition over the last million years, indicating that the evergreen broadleaved forests still survived in the southern coastal areas of China in glacials, probably broader in its distribution than today. The early period of the vegetation history before 900 ka is marked by relatively high percentages of tropical montane pollen and *Altingia* within the tropical and subtropical pollen, implying cooler climate than today. The period of 900–360 ka saw the occurrence of Dipterocarpaceae, Celastraceae, *Cycas, Eugenia, Mallotus/Macaranga* and *Trema*, indicating a relatively warm climate. Since ~360 ka trees from Fagaceae began to expand and became absolutely dominant in the forest, probably implying strengthened seasonality and cooler climate than before.

The pollen data from core 17940, a site near Site 1144, have already showed that, during the LGM, the emerged part of the continental shelf was mainly covered by grassland inferred from the high percentages of herb pollen (Sun et al. 1999). This is further confirmed by the pollen records from Site 1144. The long-term trends in the pollen record also bear information about evolution of the shelf and its vegetation during the glacial emergence. Before 900 ka, the narrowly emerged shelf was probably covered by grassland mainly of *Artemisia* during glacials, and

then mainly of Poaceae and Cyperaceae during glacials between 900 and 160 ka. The *Artemisia* population increased again and occupied most part of the extensive emerged continental shelf during the last glacial stage. There were also sedge swamps and wetlands on the continental shelf during glacials, as indicated by the pollen of Cyperaceae, water plants like *Typha* and *Myriophyllum*, and small liverwort (*Anthoceros*). The existence of mangrove pollen since MIS 10 (Fig. 5.26), even in very low percentages, indicates that mangrove survived along the northern coast of the SCS during some glacial periods within the last 360 ka.

The frequent alternations between pine and herbaceous pollen at Site 1144 correspond to sea level changes during the last million years (Sun et al. 2003). The pollen ratio between shore plants (represented by herbaceous pollen, H) and upland ones (indicated by pine pollen, P) may indicate the relative distance of the studied site from the coast (Traverse 1988), with high ratio of H/P implying shorter distance to the coast and low ratio vice versa. The palynologically inferred changes in the distance from the coast indicated by H/P ratios at Site 1144 should be ascribed to eustatic sea-level changes during glacial cycles (Fig. 5.25). H/P ratios reach the maximum (5.5) during the LGM, and the minimum (0.01) in the Holocene. The large amplitude variations of H/P values in MIS 3 may suggest significant sea-level changes in the area, as recorded in the coastal zone of China (Wang P. et al. 1981).

However, a broader emerged shelf can also result in a higher H/P ratio than a narrow one. Changes in the size or width of the exposed continental shelf in the northern SCS are probably other factors influencing H/P variations. The small amplitudes in variations and low values of H/P before MIS 6 suggests a narrow and steep continental shelf, with only a limited area exposed at the lower sea-level stand, and the broadening of the continental shelf around MIS 6 was probably caused by neotectonics of the China continent related to the uplift of the Tibetan plateau (Fig. 5.27) (Li J. 1991; Li and Fang 1996).

Pollen records at Site 1144 serve as direct proxies of the past variability of the East Asian winter and summer monsoons. The downcore variations of the tree pollen influx (Fig. 5.26) show that the higher values occur in glacial periods compared with lower values in neighboring interglacials, indicating intensification of the winter monsoon in glacial periods and weakening in interglacials. Moreover, in most cases the pollen influx values are very low at the beginning of a glacial cycle and then increase gradually, reaching the maximum at its end and then abruptly falling down to the minimum at the beginning of the next interglacial. Similar to

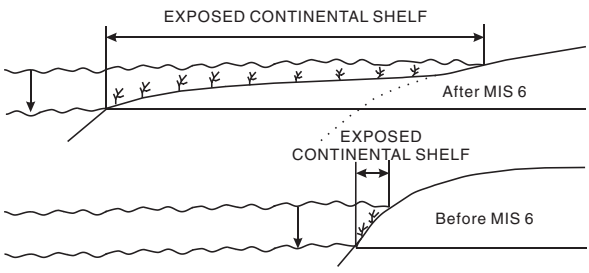

Fig. 5.27 Schematic diagrams show changes in width of the northern continental shelf of the SCS during glacial stages before and after MIS 6, as inferred from the pollen record (from Sun et al. 2003)

foraminiferal $\delta^{18}O$ variations, they indicate a causal relationship between global ice volume and monsoon variations.

Over the past 1 myr, the tree pollen influx value noticeably increased since MIS 16, indicating that the Asian winter monsoon began to intensify since ~670 ka ago when the European Alps experienced the first major glacial, the Günz glaciation. Grain size analysis of a number of loess sequences from the Loess Plateau in central China also shows the intensification of the winter monsoon during the last ~0.6–0.45 myr. Significant advance of the Mu Us desert (north of the Loess Plateau) and better development of paleosols than those formed before imply enhancement of both winter and summer monsoons during the last 0.6 myr (Ding et al. 1999). Similarly, increased dust influx in Lingtai and Xifen loess profiles is regarded as an increase of aridity and, hence, of winter monsoon intensity during the last ~0.6 myr (Hovan et al. 1989; Sun and An 2001).

Other pollen records such as herbs demonstrate similar glacial cycles as the tree pollen influx. Fox example, the high values of tree pollen influx at MIS 2, 5, 12 are accompanied by similar peaks of *Artemisia* and herbs in general (Fig. 5.25), all displaying sawtooth-like curves. However, tree pollen influx also shows high values at MIS 5b and two spikes within MIS 3, probably related to intensive and variable winter monsoon during these interglacial periods. The unstable climate of MIS 3 is also evidenced by the high H/P ratio and high percentage of *Anthoceros* at Site 1144.

For the pollen sequence at Site 1144, there are humidity-indicative palynomorphs closely related to the summer monsoon intensity. Ferns usually grow under humid conditions, with higher fern percentages suggesting wetter climate (Van der Kaars 1991; Van der Kaars et al. 2000). In addition, fern spores are produced in enormous numbers and hence suitable for quantitative analyses. Therefore, the fern spore proportions to the total pollen sum of land seed plants may serve as summer monsoon proxy. Downcore variations of fern percentages show higher values in interglacials and lower values in glacials, suggesting strong summer monsoons during warm periods (Fig. 5.25F). The significantly strong summer monsoon have occurred during late MIS 1, 5e and 15, evidenced by very high values of fern spore percentage. Fern spore percentage maintained high and constant values before MIS 16, probably reflecting relatively strong and stable summer monsoon before MIS 16.

Spectral analyses of herbs and pine percentages at Site 1144 discover a set of Milankovich cycles for the last 1 myr, the strong 100 kyr eccentricity cycle, the weak 41 kyr obliquity cycle and a more distinct 23 kyr precession cycle, as well as some significant semi-precessional cycles (~11, 10, and 9 kyr) (Fig. 5.28), revealing the orbital forcing on the vegetation changes in the source regions that delivered pollen to the northern SCS. Cross-spectral analyses of herb and pine pollen percentages with planktonic foraminiferal $\delta^{18}O$ records show very high non-zero coherences (>90%) at the 100 kyr and 23 kyr bands (Fig. 5.29). Phase relationships between pollen and $\delta^{18}O$ records show that the vegetation changes are nearly in phase with or slightly lag the global ice volume maxima at the 100 kyr and the 23 kyr bands, respectively (Sun et al. 2003). Spectral and cross-spectral analyses reveal close relationship of the vegetation changes in the northern SCS with those changes in global ice volume, sea level and monsoons.

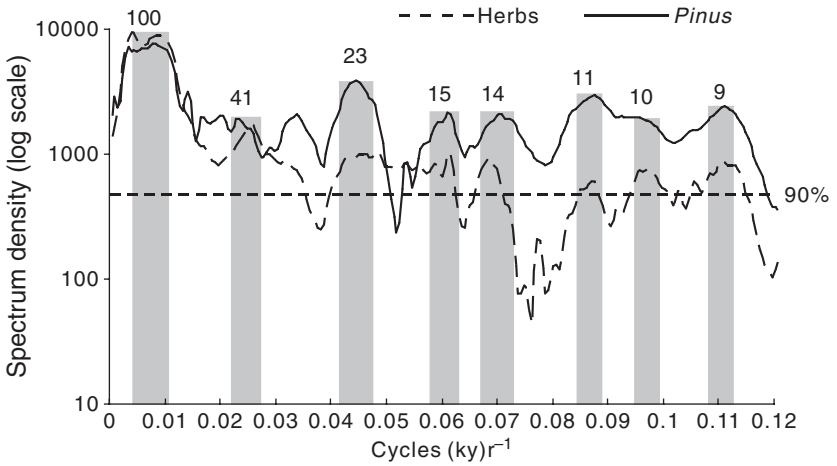

Fig. 5.28 Spectral analysis of pollen percentage values of herbs (*dashed line*) and pine (*solid line*) at ODP Site 1144 shows the presence of various Milankovich and suborbital cyclicities for the last 1.0 myr (from Sun et al. 2003). The *horizontal dashed line* indicates the 90% level of significance

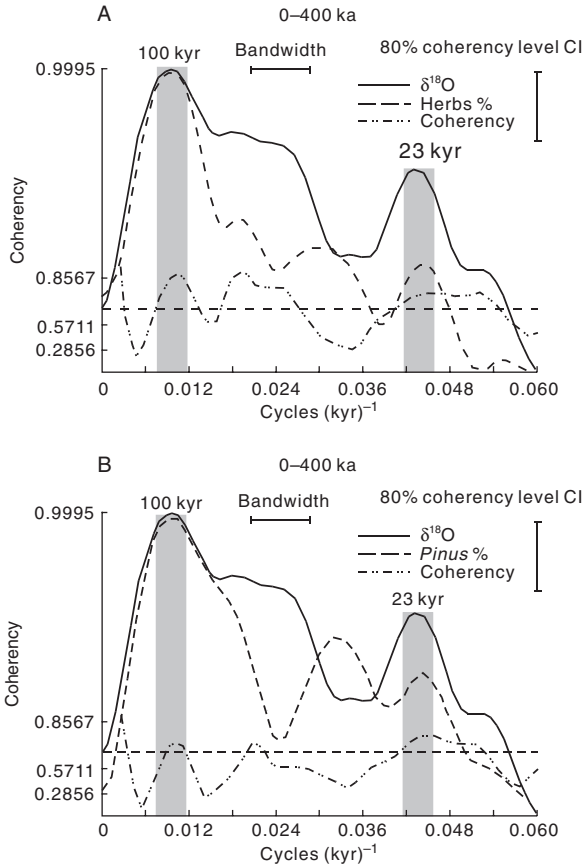

Fig. 5.29 Cross spectral analyses of $\delta^{18}O$ (*solid line*) with herbs% (**A**, *dashed line*) and *Pinus*% (**B**, *dashed line*) in the last 400 kyr at ODP Site 1144 show strong coherence over the 100 kyr eccentricity band and the 23 kyr precessional band (from Sun et al. 2003). Spectral densities are normalized and plotted on a log scale. The coherency spectra are plotted on a hyperbolic arctangent scale. The *horizontal dashed line* denotes 80% coherency level. Point-dashed lines indicate coherency

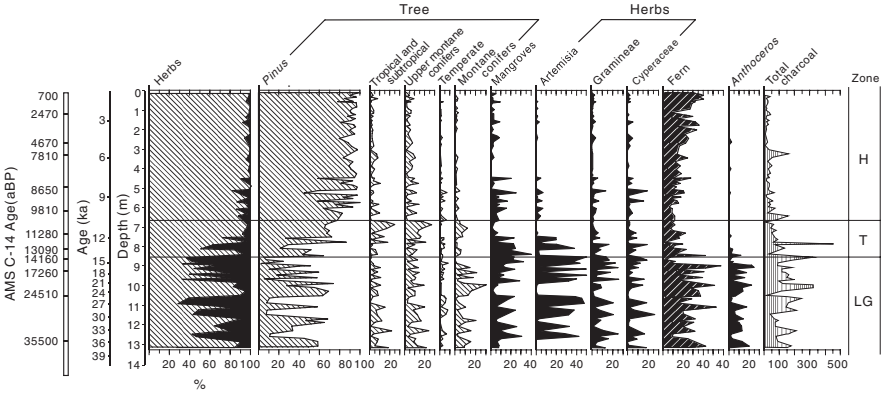

Fig. 5.30 Pollen percentage profiles and charcoal concentration curve (grains/cm^3) from core 17940, the northern SCS, show changes in three pollen zones (from Sun and Li 1999). Ecological groups include: tropical and subtropical broadleaved taxa (mainly *Castanopsis, Quercus, Ilex, Altingia, Elaecarpus*, Palmae, Sapindaceae, Araliaceae, Gesneriaceae, etc.), temperate broadleaved taxa (mainly *Betula, Carpinus, Alnus, Juglans*, etc.), montane confers (*Picea, Abies, Tsuga*) and upper montane rain forest taxa (*Podocarpus, Dacrydium, Phyllocladus, Dacrycarpus*)

Last Glacial Pollen Records: North-South Differences

Northern SCS

The best pollen record over the last glacial from the northern SCS was generated from core 17940, in which a total of 161 pollen types were identified, with 13 AMS ^{14}C dates for time constraint. A large number of tree pollen taxa from this core, except the predominant *Pinus*, were grouped into several categories according to their ecology (Fig. 5.30) (Sun and Li 1999). On the basis of downcore variation in different ecological groups it can be clearly divided into three zones, namely Zone LG, Zone T and Zone H (Table 5.2).

During MIS 3 and MIS 2 (the LGM), the pollen assemblages are marked by alternating dominance of montane conifers and upper montane rainforest taxa with herb taxa, denoting cooler climate than the present day. Today the montane conifers and montane rainforest gymnosperm incline to inhabit cool and humid environments. They are distributed either in montane areas of northern China and Taiwan (such as Picea, Abies) or in montane areas of tropical subtropical areas (*Dacrydium, Podocarpus, Dacrycarpus, Phyllocladus*). *Anthoceros* is a small liverwort, recorded

Table 5.2 Division of pollen zones in core 17940 is based on Sun and Li (1999)

Zone	Depth (cm)	Interval/Period	Age (ka)
H	0–660	Holocene (MIS 1)	0–10
T	660–723	Younger Dryas	10–11.3
	723–870	Bølling-Allerød	11.3–15
LG	870–1050	Last Glacial Maximum	15–25.3
	1050–1306	MIS 3	25.3–37

almost only during the last glaciation. The living *Anthoceros* prefers to grow in deforested areas, on the edges of forests, or on moist soil in northeastern China (Gao and Zhang 1981). High percentages of these pollen and spores denote much cooler climate than in the present day.

Large amount of herb pollens was found during the glacial period. As the dominant component in the herb group, *Artemisia* is a herb or a small shrub widely distributed in temperate grasslands in the northern Hemisphere. In the pollen assemblages from the surface sediments of the SCS, only a few pollen grains of this taxon occur in rare samples adjacent to the northern continent. During the LGM, high frequencies of *Artemisia* occurred in northern China and declined eastward and southward. In southeastern China, close to core 17940, *Artemisia* grains were sporadic or even absent at 18 ka (Sun and Li 1999; Sun et al. 2000b). So, where did such a great amount of *Artemisia* pollen in the glacial SCS come from? A plausible answer is that they came from the exposed continental shelf of the SCS which was occupied by grassland, dominated by *Artemisia*, under a comparatively dry and temperate condition. Judging from the above mentioned pollen data, the exposed continental shelf during the last glacial time was probably occupied by grassland, with montane conifers growing on nearby mountains. Therefore, the northern part of the SCS had experienced remarkable decline in temperature and humidity. Moreover, the amount of charcoal during the last glacial was much higher than during the Holocene, suggesting frequent fire due to the dry climate (Sun et al. 2000a). However, the frequent alternating predominance of the herb-dominant and montane confers-dominant groups also implies unstable conditions with frequent alternations between relatively cool and humid and comparatively dry and warm stages.

During Termination I, the vegetation and climate experienced remarkable fluctuations. Those include a sudden expansion of tropical and subtropical vegetation and mangroves, which indicates abrupt warming during the Bølling and Allerød, and a rapid increase of montane conifers, which indicates abrupt cooling during the Younger Dryas. These changes exhibit the main futures of climatic oscillations of the same time in the northern Hemisphere.

The Holocene is distinguished by absolute dominance of pine pollen (~90%), gradually increasing of fern spores and disappearance of *Anthocerus* and mangroves. The pollen records are quite similar to those of the surface sediments from the northern SCS, implying that the vegetation and climate was similar to that of the present day, with gradual warming of the climate and continuing submerging of the continental shelf. The sudden rise of spore *Dicranopteris* about 2 kyr ago might have resulted from intensification of human activities. *Dicranopteris* is atypical tropical or subtropical fern, often distributing in deforested places after human interferences (Guangdong Institute of Botany 1976).

Southern SCS

Pollen types are different between the southern and northern parts of the SCS. Four main ecological groups of pollen were discovered in pollen assemblages from the south (Li and Sun 1999). The first group includes tropical montane rainforest,

reflecting a cool and humid climate. The second group is low montane rainforest taxa. The third group is rainforest taxa with more than one hundred pollen morphs identified, denoting hot and humid climate. The fourth group includes mangroves, *Rhizaphora, Sonneratia* and *Liuminizera* growing in brackish water along tropical coasts and serving as an indicator of tropical coastal line. The rise of mangrove percentage in pollen diagram is closely related to sea level rise (Ellison 1993; Grindrod and Rhodes 1984). The last glacial pollen data of the southern SCS come from two areas: the southern continental slope and the Sunda Shelf.

Southern slope. Detailed pollen data are available from 3 cores: 17964, 17962 and 18287 (see Fig. 1.1 and Table 5.1 for locations). The bottom of core 17964 was dated at 26 ka, and the pollen assemblages from this core are dominated by tree pollen, with less herb pollen (<20%). Remarkable from the first glance is the absence of the glacial/interglacial contrast frequently observed in the northern SCS. Nevertheless, four pollen zones (P1-P4) were recognized that represent different stages of vegetation and climatic changes (Fig. 5.31) (Li and Sun 1999).

The glacial time (P1) is dominated by tree pollen taxa (>80%), excluding considerable amount of pine, composed mainly of upper montane rainforest and lowland rainforest and mangroves. Herb pollen percentages are quite stable through the profile (around 20%), while fern spores are very high in percentages. Pollen assemblage from this stage probably indicates that the climate was gradually getting cooler from MIS 3 towards the LGM. Mangroves pollen percentages increase upwards the profile as well, suggesting gradually exposure of the Sunda Shelf with sea level drop.

The striking feature of the deglaciation (P2) is that the total pollen influx (grains/cm^2/yr) and influxes of each group and taxa are in their maximum values, probably resulting from the rapid migration of the coastline and accompanied erosion. The pollen record at this stage denotes that the Sunda Land was covered mainly by lowland rainforest. The pollen percentages of mangroves increased during the later stage of deglaciation (P3).

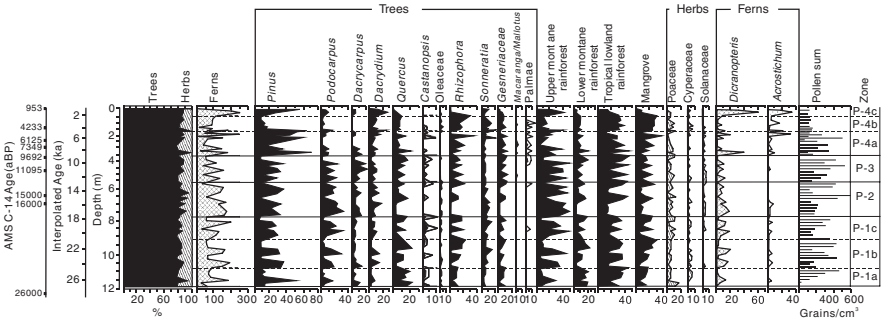

Fig. 5.31 Pollen percentage diagram of core 17964 from the southern South China Sea with four pollen zones (P1-P4) recognized: P1 (718–1178 cm, 18.3–26.5 ka), P2 (478–718 cm, 13.8–18.3 ka), P3 (318–478 cm, 9.9–13.8 ka), and P4 (0–318 cm, 0–9.9ka) (modified from Li and Sun 1999)

The Holocene (P4) can be divided into three substages. The early part (9.9–5.2 ka) is characterized by abruptly increased pine pollen and mangroves, and a slight decline of lowland rainforest. In the middle part of P4 (5.2–2.3 ka), pollen percentages of the lowland rainforest and mangroves (especially *Rhizophora* and *Sonneratia*) increased their pollen percentages, but those of the montane rainforests continuously declined and almost disappeared, indicating the warmest climate developed in the middle Holocene. In the most recent part (2.3 ka-present), pollen percentages of the lowland rainforest and mangroves declined, but those of *Pinus*, upper montane rainforest and fern spores (spores of *Dicranopteris* and *Acrostichum* in particular) increased considerably, implying a cooler climate and human disturbances during the late Holocene (Li and Sun 1999).

Core 17962 is quite similar to core 17964 in pollen assemblages, especially during the Holocene (Sun et al. 2002). However, the pollen assemblages of core 17962 changed much more smoothly (Fig. 5.32) and did not display clear millennial-scale oscillations in different ecological groups of pollen taxa. In addition, the lowland rainforest dominated the whole pollen profile, except the early Holocene. The pollen influx values in core 17962 were high during the glacial stage with maximum values in the LGM, but they progressively decrease during the Termination I and to a minimum in the Holocene (Fig. 5.32).

Core 18287 recovered from the upper slope close to the Sunda Shelf covers only Termination I and the Holocene, and the pollen profile is dominant by tree pollen taxa (Fig. 5.33; see Figs. 1.1 and 5.35 for location). The upper montane rainforest pollen of this core is low in percentages throughout the whole profile, but the

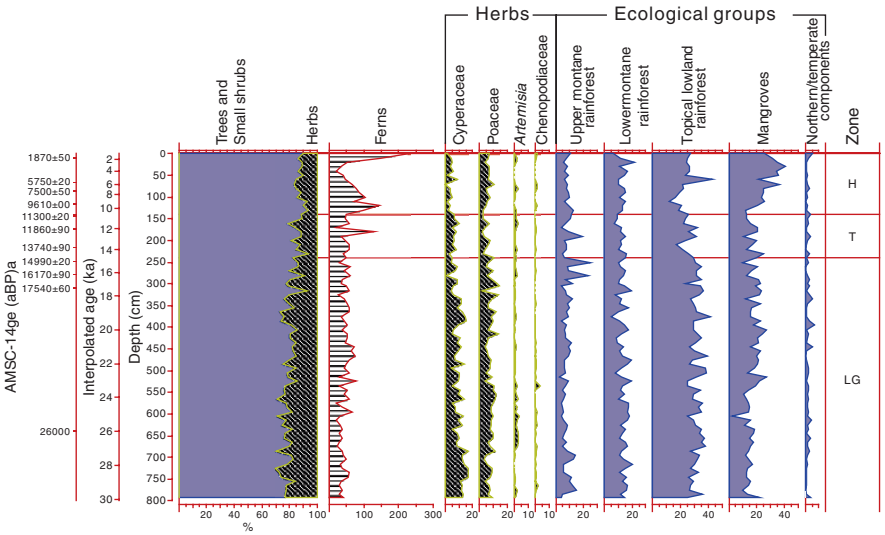

Fig. 5.32 Pollen percentage diagram of selected taxa from core 17962 from the southern SCS shows weaker variations compared to other site localities (Sun et al. 2002). LG = last glacial; T = Termination; H = Holocene

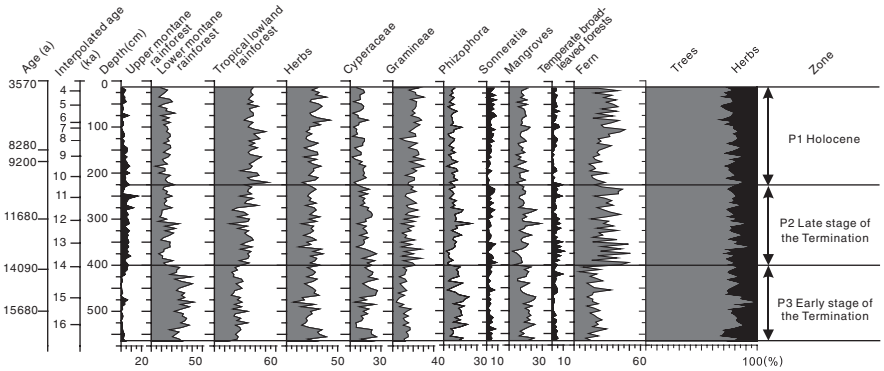

Fig. 5.33 Pollen percentage diagram of core 18287 from the southern SCS shows variations from Termination I to the Holocene (from Wang X. et al. 2007)

lower montane rainforest pollen serving as cool climate indicator is quite abundant. During theTermination the lowland rainforest and fern expanded their distributions and the lower montane rainforest progressively moved up to the mountains and its distribution area on the shelf shrank, probably caused by climate warming during this period (Wang X. 2006; Wang X. et al. 2007).

The three cores discussed above (17962, 17964, 18287) range from north to south. A comparison of their pollen influx profiles reveals a southward migration of its maximum value: at LGM in the northern core 17962 but at Termination I in the southern core 18287 (Fig. 5.34). This pattern confirms that the pollen was transported northward from the Sunda Shelf and the maximum influx moved to the

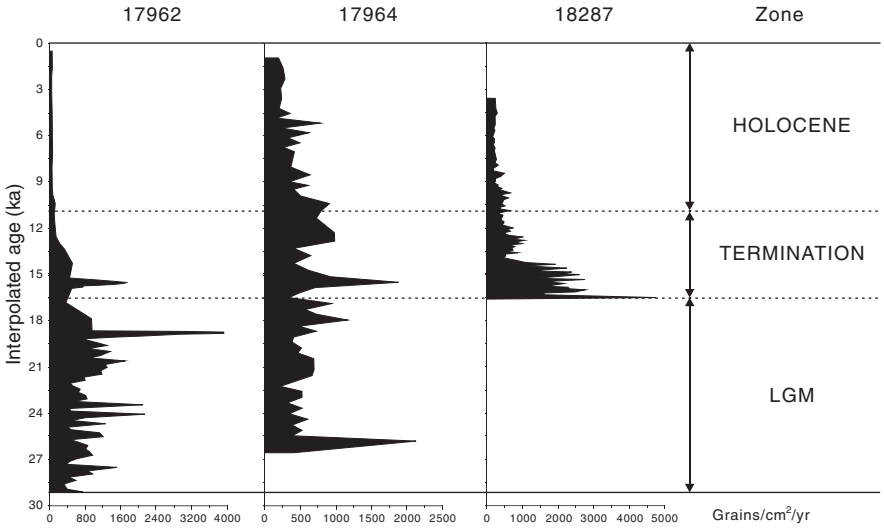

Fig. 5.34 Total pollen influx (grains/cm^2/yr) curves for cores 17962 (Sun et al. 2002), 17964 (Li and Sun 1999) and 18287 (Wang X. 2006) indicate a shift of pollen deposition center southward with sea level rise from the LGM to Termination I

south with the postglacial retreat of the coastline. In the Holocene, extremely low pollen influx at these cores indicates that the sea level rose and the Sunda Shelf submerged into the seawater. Therefore, the neighboring islands, mainly Borneo, became the only pollen source area. Noticeable is the middle Holocene, when both sea level rise and the submerged area of the shelf reached its maximum, and the climate was warmer and more humid than today, as evidenced by maximum pollen percentages of mangroves. During the late Holocene, pine pollen increased again but lowland rainforest and mangroves sharply decreased, probably related to climatic cooling. The sudden increase of fern spores in the late Holocene as recorded in core 17962 (Fig. 5.32) suggests intensive deforestation by human activities (Li and Sun 1999; Sun et al. 2002).

Sunda Shelf. During the LGM, the Sunda Shelf was widely subaerially exposed as a large low-gradient coastal plain, while the modern Malayan Peninsula, Borneo and Sumatra Islands formed highlands to the west and south (Tjia 1980; Hanebuth et al. 2000). Several rivers originating here drained the coast lowland during the LGM. Pollen assemblages from three cores were studied in detail (Wang X. 2006; Wang X. et al. 2007, 2008): cores 18300 and 18302 from the outer shelf in modern water depths of 92–98 m and core 18323 from the inner shelf but in a paleo-river channel with modern water depth of 87 m (Fig. 5.35). The pollen records from the three cores are shown in Fig. 5.36.

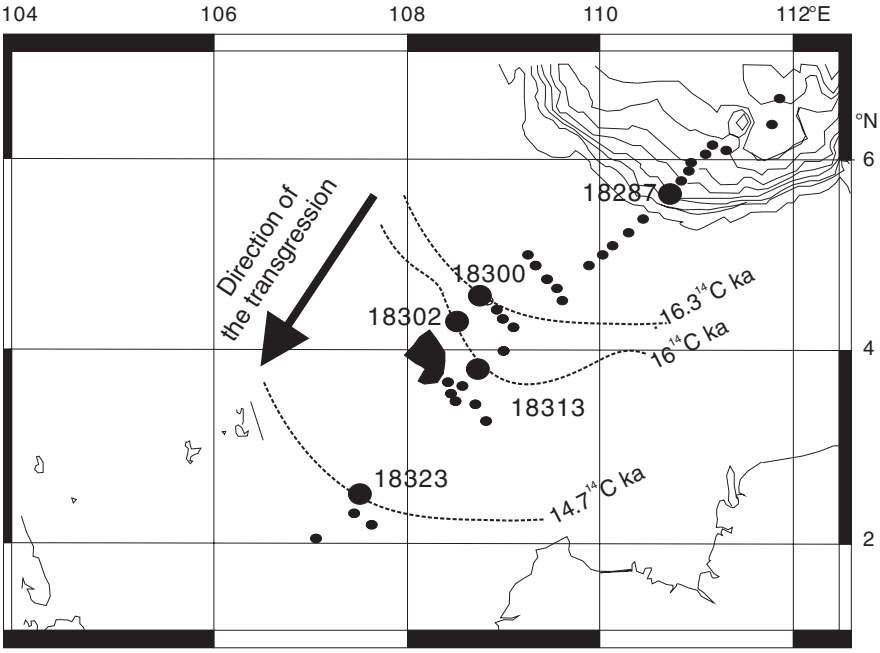

Fig. 5.35 Location map shows the palynologically studied sites (*large filled circles*) revealing the rising trend of sea level and the submergence of the Sunda Shelf after the LGM (from Wang X. 2006). *Dotted lines* show paleo-coastline. *Small dots* are other sites cored during SONNE Cruise 115 (Stattegger et al. 1997)

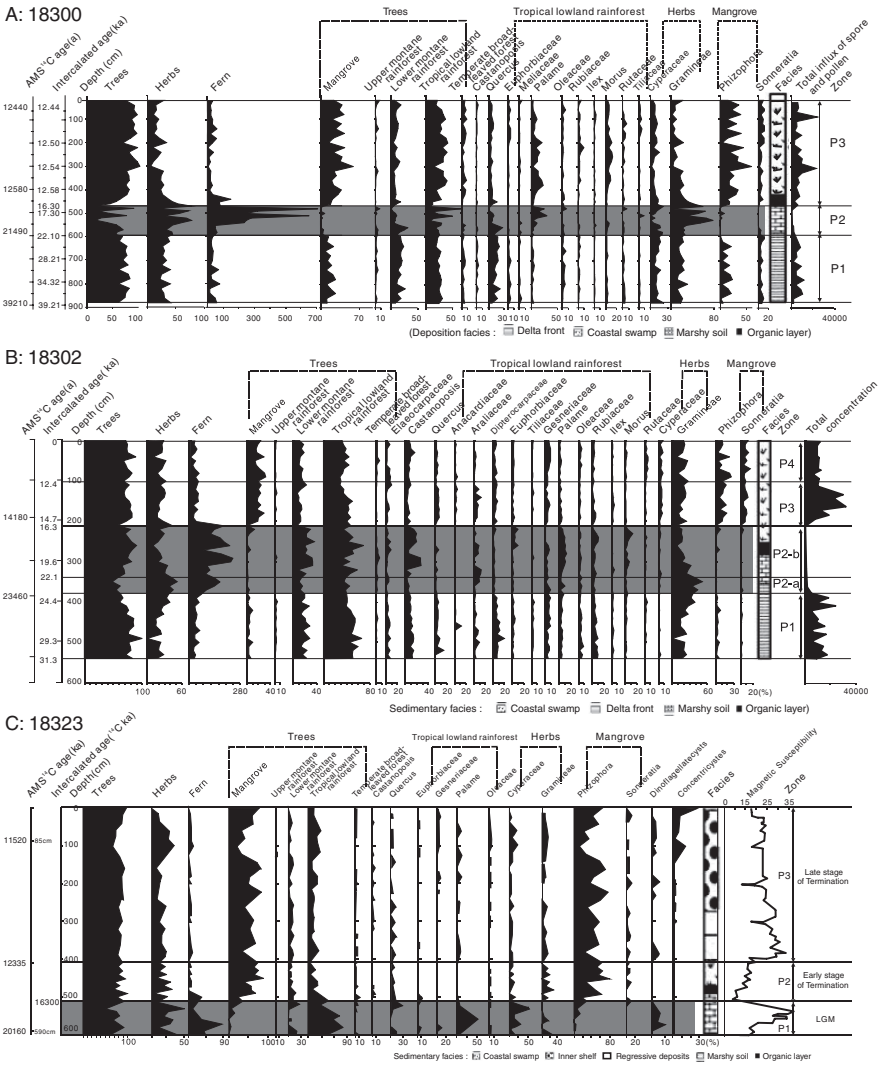

Fig. 5.36 Pollen percentage diagrams of cores 18300 (**A**), 18302 (**B**), and 18323 (**C**) from the Sunda Shelf indicate a major change during the LGM (*shaded interval*) (modified from Wang X. (2006)

All the 3 cores reached the last glacial. Most interesting is the pollen record of the LGM (including early H1 event; shaded zone in Fig. 5.36), although ages slightly differ between cores (~22.1–16.3 ka for P2 at 18300, ~20.16–16.3 ka for P1 at 18302, and ~23.46–16.3 ka for P2 at 18323). Before the LGM (such as P1 in 18300), tree pollen is prevailing with considerable amount of mangrove pollen. The LGM and early H1 times, however, are characterized by dominance of herb pollen (mainly Poaceae) and fern spores (mainly *Cyathea*) and by very low pollen

influx and occurrence of *Phagmites* (sedge, a water or swamp plant). Tree pollen dropped to ~50% and mangrove pollen almost disappeared during the interval. This is very different from the pollen assemblages of MIS 3 and subsequent Termination I (P3 in core 18300), which features a sharp decrease in herb pollen and fern spores but increase in tree pollen. Mangroves increased remarkably, suggesting that the area was submerged with the coastline approaching again (Fig. 5.36) (Wang X. et al. 2008).

Summarizing the pollen records from cores 18300, 18323, 17962 and 17964, regional environmental changes since MIS 3 in the southern SCS can be reconstructed. In the course of sea level drop, the inner shelf was already subaerially exposed and covered mainly by lowland rainforest, but the outer shelf was still covered by shallow seawater (Fig. 5.37A). The lower montane rainforest probably migrated from montane areas of the southern island down to the shelf and became an important part of the glacial vegetation. The climate at that time was cooler than the present day, but could be still very humid. During the LGM and early H1, the pollen assemblages from the continental slope were dominated by lowland rainforest and mangroves, whereas those from the shelf were prevailed by high percentages of herb pollen and fern spores without mangroves. One source area of the pollen was from the marshy plants growing along the Sunda River, and the other was from the vegetation distributed on the Sunda Land (Fig. 5.37B). Lowland rain forest and lower montane rainforest covered the exposed Sunda Land during the LGM and H1, and the upper montane rainforest periodically migrated down along the montane slopes of the southern islands. The climate should be cooler than the present day, but still humid. During the Termination I after ~16 ka, pollen assemblages are dominated by lowland rainforest and mangrove (Fig. 5.37C). Mangrove pollen reappeared and increased quickly upwards the profiles on the shelf, indicating sea level rise and shelf submerging again. These changes indicate postglacial warming and lowland rainforest covering the exposed part of the shelf during the Termination.

North-South Comparison of the Vegetation During the LGM

The pollen data summarized above have outlined a distinct picture of north-south contrast of vegetation in the late Quaternary SCS, specifically for peak glacial and H1 times. Grassland vegetation, mainly composed of *Artemisia*, then covered the exposed northern continental shelf of the SCS, indicating colder and drier climate relative to the present day. But the subaerially exposed southern continental shelf, the Sunda Land, was covered by lowland rainforest and lower montane rainforest; mangroves grew along the coast and montane rainforest migrated down the montane slopes many times during this period. Along the North Sunda River distributed marshy vegetation. This evidence of pollen assemblages indicates cool but humid climate in the southern SCS during the LGM.

The difference in humidity between the northern and southern SCS was probably caused by changes in the East Asian monsoon system (Sun et al. 2000b). The

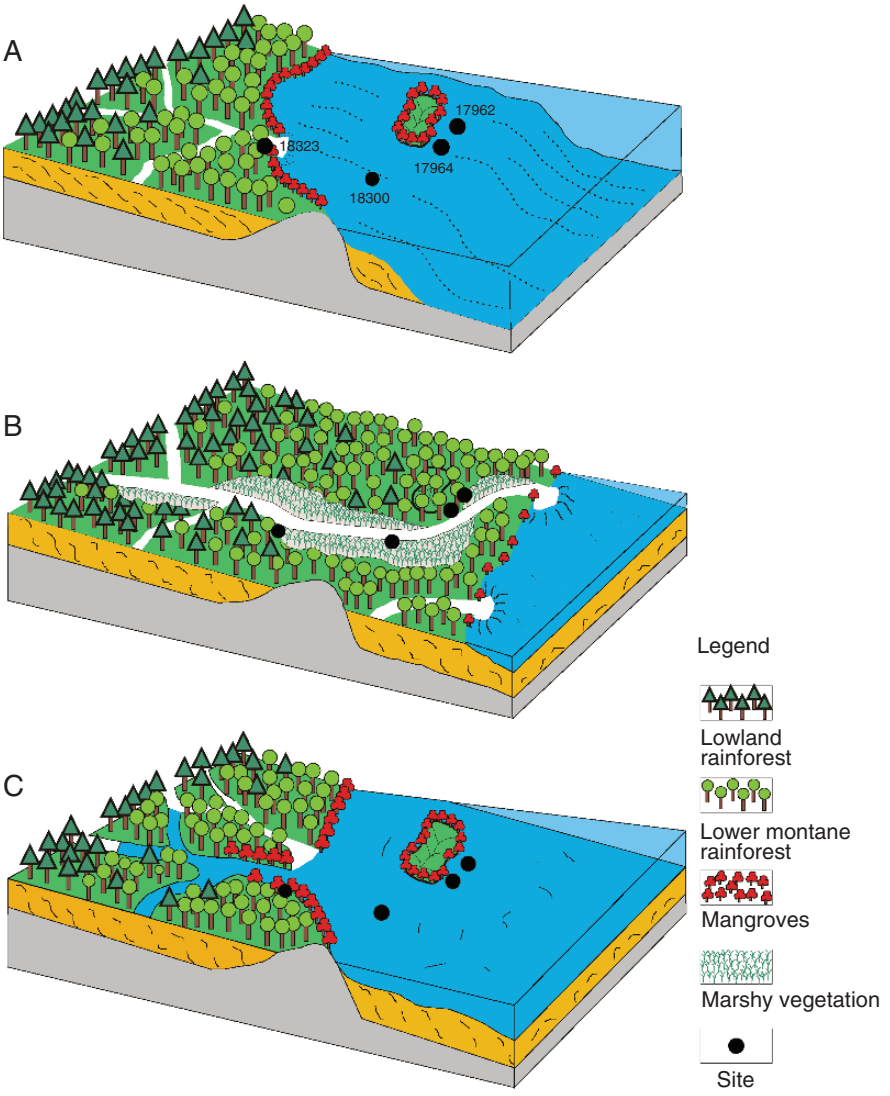

Fig. 5.37 Schematic diagrams show paleovegetation evolution on the Sunda Land from (**A**) MIS 3, to (**B**) LGM and H1 times, and (**C**) Termination I after 16 ka

intensification of Siberian High over the East Asian continent during the glacial period strengthened the East Asian winter monsoon, which in turn led to the lower temperature and reduced humidity in the region including the northern SCS. By contrast, the East Asian winter monsoon becomes Australian summer monsoon when it crosses the Equator, and brings precipitation to the islands of southeastern Asia. During the last glaciation, the strengthened boreal winter monsoon absorbed moisture when crossing the SCS and provided more precipitation to the Sunda

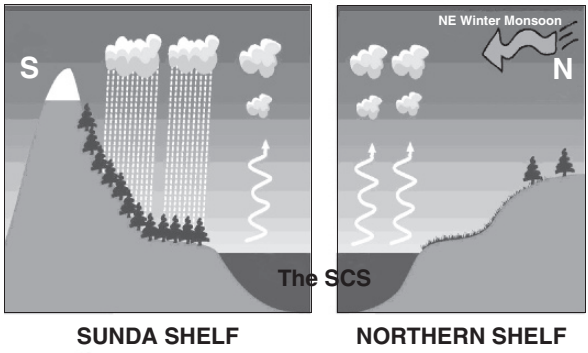

Fig. 5.38 A schematic diagram shows vegetation and rainfall differences between the northern (*right panel*) and southern SCS (*left panel*) during glacial stages. While grassland vegetation covered the exposed continental shelf under strong winter monsoon in the north, more precipitation in the south was provided by the strengthened winter monsoon which absorbed moisture when crossing the sea, enabling lowland rainforest to grow

Land, leading to the continued growth of lowland rainforest and mangroves there. Moreover, the island areas south of the southern SCS without relief obstruction could also receive more rainfall to enable humid rainforest vegetation to grow (Walker and Flenley 1976; Stuijts et al. 1988; Hope and Tulip 1994). However, areas located in the rain-shadow behind mountains may have experienced an arid climate and grown grassland vegetation due to a lack of moisture from the monsoon (Fig. 5.38).

This idea was confirmed by *n*-alkane stable carbon isotopic analysis ($\delta^{13}C$) of core 17962. Accumulation rates of long–chain *n*-alkanes suggest that intensified river flows occurred on Sunda Land due to intensified winter monsoon precipitation during the last glacial period. The isotopic composition ranges from $-27.1‰$ to $-33.9‰$ for C27-C33 n-alkanes in the entire core sequence, indicating an input mainly from C3 higher plants (Hu et al. 2003). This means that rainforest continued growing on the Sunda Shelf in a constant humid climate although the possibility of certain decrease in precipitation cannot be excluded. Since the present climate in the Sunda Shelf is extremely humid, "there could be a decrease in the total precipitation which the area receives, without there necessarily being any recognizable effect on vegetation" (Newsome and Flenley 1988).

5.4 Monsoon History (Jian Z. and Tian J.)

The climate records in the SCS discussed so far in this chapter cover a broad spectrum from land vegetation to upper water structure, but all are focused on the main feature of the region: the East Asian monsoon system. The following is a brief overview of the monsoon history as recorded in the SCS. A correct use of proxies is a prerequisite for paleo-monsoon reconstruction.

Monsoon Proxies

Terrestrial sediment records provide reliable East Asian Monsoon proxies. For example, loess deposits show clear evidences of monsoon changes in the late Cenozoic, with magnetic susceptibility and Rr/Sr ratio indicating summer monsoon change, and grain size and Al flux indicating winter monsoon change (Porter et al. 1992; Ding et al. 1992, 1994; Vandenberghe et al. 1997; An et al. 2001; Guo et al. 2002). Stable oxygen isotopes of cave stalagmites from the southern China document millennial and orbital scale variabilities of precipitation mostly during summer seasons, serving as a perfect East Asian Summer Monsoon proxy (Wang Y. et al. 2001, 2005, 2008; Cheng et al. 2006). Recently, the magnetic properties and the titanium content in sediments of Lake Huguang Maar in coastal southeast China have been found to be East Asian winter monsoon proxies (Yancheva et al. 2007), anticorrelated to the cave stalagmite records of summer monsoon.

Marine deposition in the SCS involves a complex of physical, biological, and chemical processes, making marine proxies associated not only with monsoon changes but also with several other variables, and thus is usually more complex than terrestrial deposition. In addition, there has been much less observation of monsoon-related modern processes in the SCS as compared to the Arabian Sea. Therefore, the use of monsoon proxies in the SCS needs to be employed with caution to avoid misinterpretation. As everywhere, it is better to utilize a multi-proxy method for monsoon study in the SCS, with support of evidences from modern hydrological features and from core top and sediment trap analyses.

In 2005, the SCOR-IMAGES Evolution of Asian MONSoon (SEAMONS) working group provided a summary of geological archives and their proxy data of the Asian monsoon (Wang P. et al. 2005). In general, monsoon proxies from the SCS can be divided into two groups according to the primary aspects of the monsoon that they address: direct proxies related to monsoon winds (direction and strength), and indirect proxies related to monsoon-induced precipitation or upper ocean structure changes such as the thermocline depth (Table 5.3). Many of the monsoon proxies have been already discussed in the previous paragraphs, some additional remarks and a few proxies specific of the SCS, grouped into paleontological, isotopic, mineral and elemental geochemical, and organic geochemical proxies, are briefly introduced below.

Microfossil and Isotopic Proxies

As shown in preceding sections, micropaleontological and palynological proxies are among the most frequently used methods in paleo-monsoon studies, yet the application of a particular proxy has its spatial and temporal limitations. In the Indian Ocean, for example, the census count of the planktonic foraminifera *Globigerina bulloides* serves as a good upwelling indicator and thus an ideal proxy of the Indian monsoon, as evidenced by sediment trap time series and plankton-tow data (Curry et al. 1992) and confirmed by its geographic distribution in core-top sediments (Prell 1984). *G. bulloides* has been widely used in upwelling regions of the Arabian Sea for paleo-monsoon studies on long-term tectonic scales (Kroon et al. 1991) to

Table 5.3 Synthesis of monsoon proxies indicates two groups of proxies (direct and indirect) commonly used in the SCS (modified from Wang P. et al. 2005)

Features and processes	Proxies	References
Wind system (*direct proxies*)		
Wind directions (surface and mid-tropospheric wind)	Lithogenic tracers	
	Clay minerals	Liu Z. et al. 2003
	Specific pollen types and assemblages	Sun et al. 1999
	Loess-type sediments (>6 μm)	Wang L. et al. 1999a
	Wind-induced coastal upwelling:	Wang L. et al. 1999a
	1. Summer upwelling S.W. of Vietnam	Jian et al. 2001
	2. Winter upwelling N.W. of Luzon	Huang B. et al. 2002
Wind strength	Silt modal grain sizes (>6 μm)	Wang L. et al. 1999a
Wind-driven precipitation (*indirect proxies*)		
Processes linked with wind strength	Thermocline depth	Jian et al. 2000b
	Planktonic foraminifera and nannofossil indices	Tian et al. 2005b Liu C. et al. 2002
1. Structure of surface ocean	Meridional SST gradient	
	Difference in planktonic $\delta^{18}O$	Wei et al. 2003
2. Upwelling productivity	Micropaleontological proxies:	
	1. Planktonic foraminifera	
	Abundance of *N. dutertrei*	Jian et al. 2003
	2. Benthic foraminifera indicative of high organic-carbon flux	Jian et al. 1999; Kuhnt et al. 1999
	3. Radiolaria Upwelling index	Wang and Abelmann 2002 Chen M. et al. 2003
	4. Nannofossils	Liu C. et al. 2002
	Geochemical proxies	
	1. Organic carbon % and flux	Jian et al. 1999
	2. Opal % and flux	Lin H. et al. 1999
	3. Ba/Al ratio	Wehausen and Brumsack 2002; Lin H. et al. 1999
	4. Cd/Ca ratio in foraminiferal tests	
	5. $\delta^{15}N$	Kienast et al. 2002 Higginson et al. 2003
	6. $\delta^{13}C$ in near-surface dwelling planktonic foraminifera as inverse nutrient signal	Wang L. et al. 1999a Jian et al. 2003
Continental runoff	Sea surface salinity estimates Planktonic $\delta^{18}O$	Wang L. et al. 1999a,b
Precipitation rate	Pollen (vegetation changes)	Sun and Li 1999; Sun et al. 2003
	Charcoal	Luo et al. 2001
Weathering and pedogenesis	Clay minerals	Trentesaux et al. 2004
	K/Si	Wehausen and Brumsack 2002
	Magnetic grain size (ARM/SIRM ratio)	Kissel et al. 2003

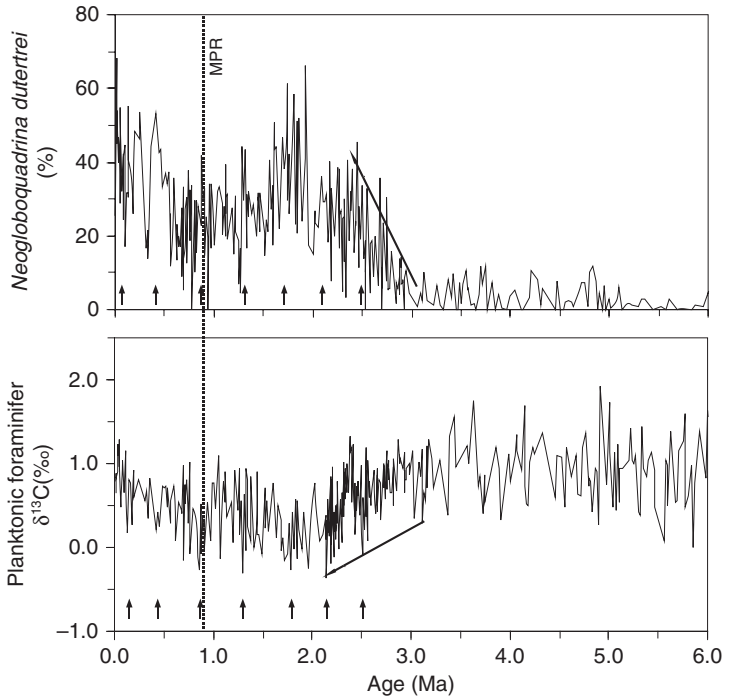

Fig. 5.39 Abundance changes in *Neogloboquadrina dutertrei* (*upper panel*) and planktonic $\delta^{13}C$ of *G. ruber* (*lower panel*) at ODP Site 1148 can be used as indirect monsoon proxies. *Oblique arrow* shows the East Asian winter monsoon strengthening in the late Pliocene. *Short arrows* indicate short-term winter monsoon enhancements as indicated by decreased $\delta^{13}C$ and increased abundance of *N. dutertrei*. *Vertical dashed line* indicates the mid-Pleistocene revolution (MPR)

high-resolution millennial scales (Anderson et al. 2002). However, its use in the SCS as monsoon indicator is hampered by its rarity because of the semi-enclosed nature of the sea basin. In the upwelling regions of the SCS, *Neogloboquadrina dutertrei*, rather than *G. bulloides*, is dominant (Pflaumann and Jian 1999). Modern observations in sediment traps (Chen et al. 2000) and surface sediments indicate that *N. dutertrei* is a typical winter and high-productivity species and can therefore serve as an indirect proxy for the East Asian winter monsoon in the SCS, as exemplified by a study of the Plio-Pleistocene sequence at ODP Site 1148 from the northern SCS (Fig. 5.39) (Jian et al. 2001, 2003).

$\delta^{18}O$ differences between subsurface *P. obliquiloculata* and surface *G. ruber* reflect monsoon-driven changes in the thermocline depth, thus are useful as monsoon indicator (see Fig. 5.20). Similarly, *G. ruber* $\delta^{13}C$ may also serve as proxy of the East Asian winter monsoon, as this seasonal reproducer (Chen et al. 2000) displays a gradual decrease in its $\delta^{13}C$ towards the Luzon Strait where the inflow of nutrient-enriched surface water is driven by the East Asian winter monsoon (Wang L. et al. 1999a; Jian et al. 2003; Cheng X. et al. 2005). At ODP Site 1148 from the northern SCS, rapid decreases in *G. ruber* $\delta^{13}C$ were coupled with increased

abundance in *N. dutertrei* during the period of 3.2–2.2 Ma, probably illustrating the trend of gradually enhanced East Asian winter monsoon. After ~2.2 Ma, several conspicuous *G. ruber* $\delta^{13}C$ negative excursions associating with increases in relative abundance of *N. dutertrei*, particularly at ~1.7, 1.3, 0.9, 0.45, and 0.15 Ma, or about every 0.4 Ma, may imply that the winter monsoon strengthened at those times (Fig. 5.39) (Jian et al. 2003).

Mineral and Elemental Geochemical Proxies

With the rapid development in technology, some mineral and elemental ratios of sediments have become progressively widely used proxies in paleo-monsoon studies. The following are a few examples from the SCS.

Ratio of smectite vs illite+chlorite is used to estimate the relative strength of the summer vs winter monsoons based on the observation that modern illite and chlorite in the SCS mainly come from the mainland of China and Taiwan Island, while smectite largely originates from Luzon and other islands of the southern SCS (Liu Z. et al. 2003; see "Clay Mineral" section in Chapter 4). The record of this ratio at ODP Site 1146 demonstrates distinctive glacial/interglacial cycles for the past 2 million years, with high values implying strong summer monsoons during interglacials and low values implying strong winter monsoons during glacials (Liu Z. et al. 2003), consistent with the results of palynological analysis at ODP Site 1144 (Fig. 5.40). Also at Sites 1143 and 1146, ratios of (illite+chlorite)/smectite,

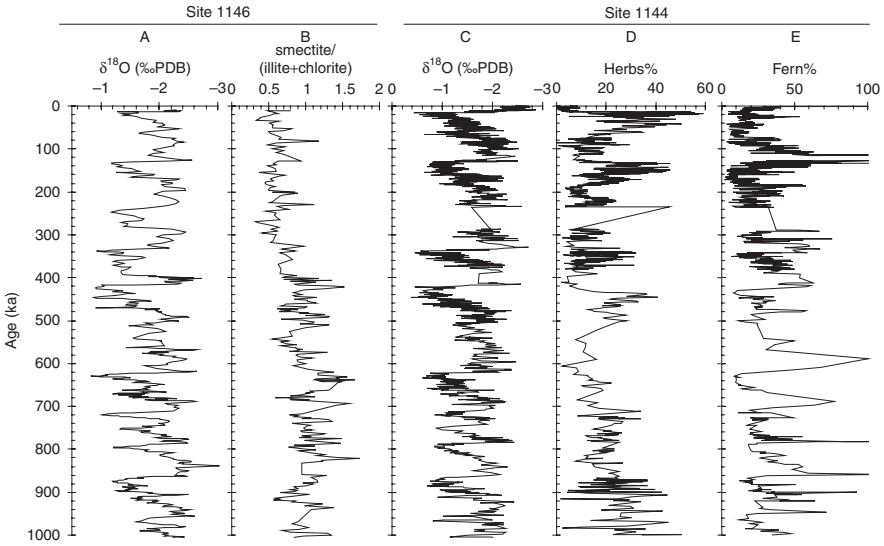

Fig. 5.40 Variations of monsoon proxies during the past one million years are from ODP Site 1146 (**A**, planktonic $\delta^{18}O$; **B**, ratio of smectite/illite+chlorite) and ODP Site 1144 (**C**, planktonic $\delta^{18}O$; **D**, herbs%; E, ferns% (percentage in the total pollen sum)) in the northern SCS (Wang P. et al. 2003)

(quartz+feldspar)% and mean grain-size of terrigenous materials have been considered as direct monsoon proxies, revealing a 20 myr long history of the East Asian Monsoon on the tectonic scale (Wan et al. 2006, 2007).

Ratio of hematite vs goethite (Hm/Gt) has been used as a reasonable precipitation proxy over the last 600 kyr in the southern SCS (Zhang et al. 2007). These authors measured the concentrations of hematite and goethite, two climatically significant Fe oxide minerals, using diffuse reflectance spectroscopy in ODP Site 1143 samples, and found a good correlation between variations in the Hm/Gt ratio and in stalagmite oxygen isotopes from South China, indicating that the Hm/Gt ratio provides a unique, long-term record of monsoon precipitation in Southeast Asia.

Ratios of K/Si and Ba/Al also show responses to insolation-driven monsoon variability in the northern SCS (Wehausen and Brumsack 2002). While the fluvial input (K/Si) responds to changes in the summer monsoon, productivity variations, as documented by Ba enrichments, seem to reflect variations in winter monsoon intensity. A stronger winter monsoon may have increased nutrient availability via dust input and/or upwelling activities. Ba/Al peaks, indicating enhanced productivity, occur during K/Si minima at ODP Site 1145 from 3.2 to 2.5 Ma, implying that summer and winter monsoons were approximately 180° out-of-phase (Fig. 5.41).

Chemical index of alteration (CIA) and elemental ratios, such as Ca/Ti, Na/Ti, Al/Ti, Al/Na, Al/K, and La/Sm, are sensitive to weathering which is closely related to East Asian summer monsoon changes (Wei G. et al. 2006). These proxies at ODP Site 1148 from the northern SCS are found to have recorded the chemical weathering history on a tectonic timescale since 23 Ma in South China. The results show that the East Asian summer monsoon has dramatically affected South China in the early Miocene, but its weathering influence decreased continuously since that time, probably because of the intensification of the winter monsoon (Fig. 5.42).

Organic Geochemical and Isotopic Proxies

$\delta^{15}N$ and chlorine accumulation rate of sediments have been employed to reconstruct oceanic nitrate inventory, the balance between denitrification and N fixation, and paleoproductivity since the LGM in the northern SCS. N fixation was locally enhanced during the LGM, coincident with increased inputs of iron-rich aeolian dust raised by invigorated winter monsoon winds from a desiccated continent (Higginson et al. 2003), indicating the possibility of $\delta^{15}N$ to be an East Asian winter monsoon index.

The accumulation rates of C_{37} alkenones and C_{30} alkyl diols have been used as East Asian winter monsoon proxies in the southern SCS (Hu et al. 2002). Pollen records indicate that drought occurred in the northern SCS and South China during the LGM (Sun et al. 1999). However, this is not the case in the southern SCS, where the enhanced winter monsoon brought precipitation of moisture from the West Pacific to the emerged Sunda Land during glacial times (Pelejero et al. 1999a,b), as evidenced in the enhanced accumulation rates of terrestrial biomarkers in core 17962 from the southern SCS (Hu et al. 2002). Both the proxies from core 17962 show enhanced paleoproductivity of coccolithophorids and microalgae such

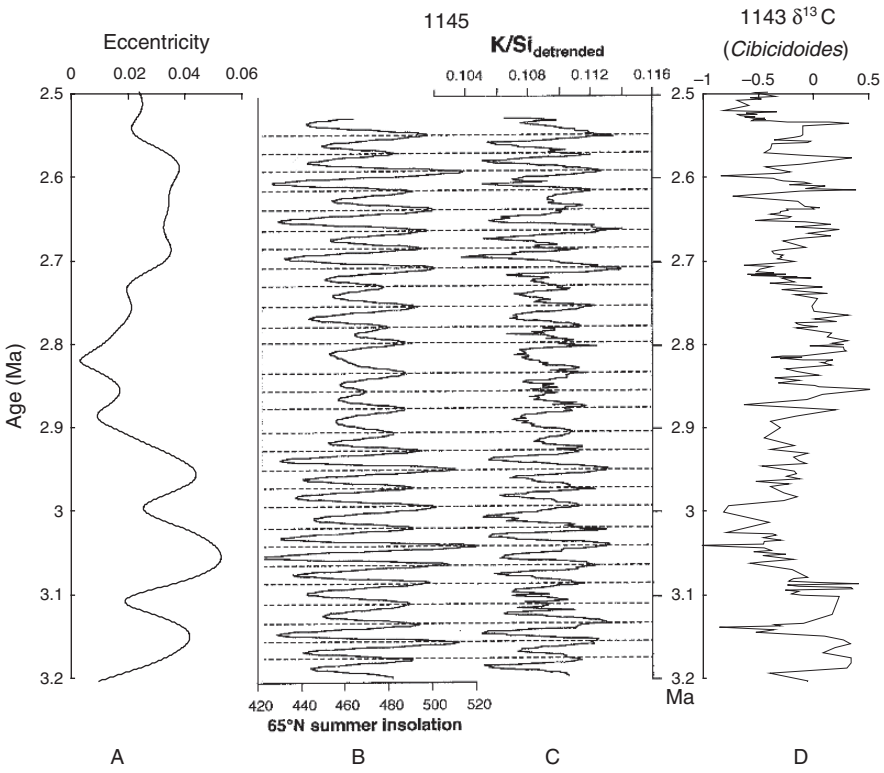

Fig. 5.41 K/Si ratio reflects the orbital forcing of summer monsoon variations in the late Pliocene (3.2–2.5 Ma) at ODP Site 1145 (**A**, eccentricity; **B**, insolation at 65 °N; **C**, K/Si ratio; from Wehausen and Brumsack 2002). Benthic $\delta^{13}C$ at ODP Site 1143 (**D**) is shown for comparison (Wang P. et al. 2003)

as eustigmatophytes during the glacial time, correlating well with those of terrestrial biomarkers (e.g., long-chain n-alkanes, high molecular n-alkanols and long-chain n-alkanoic acids), suggesting that the enhancement of marine productivity during the last glacial period would have been triggered by an increased supply of nutrients from rivers on Sunda Land, which probably had been caused by abundant monsoon rainfall.

Black carbon $\delta^{13}C$ or difference between atmospheric $\delta^{13}C$ and black carbon $\delta^{13}C$ (Δp) has been used to indicate East Asian monsoon, especially the summer monsoon variations since 30 Ma ago on the tectonic timescale (Jia et al. 2003). Because the negative adjustment in Δp of C_3 ecosystems is usually related to moisture deficits, and C_4 photosynthesis is commonly associated with hot, dry environments with warm-season precipitation in a low atmospheric pCO_2 background, secular changes in terrestrial Δp could be reasonably related to the East Asian climate evolution toward a monsoon circulation system. The reconstruction of black carbon $\delta^{13}C$ and Δp at ODP Site 1148 from the northern SCS reveals five events of

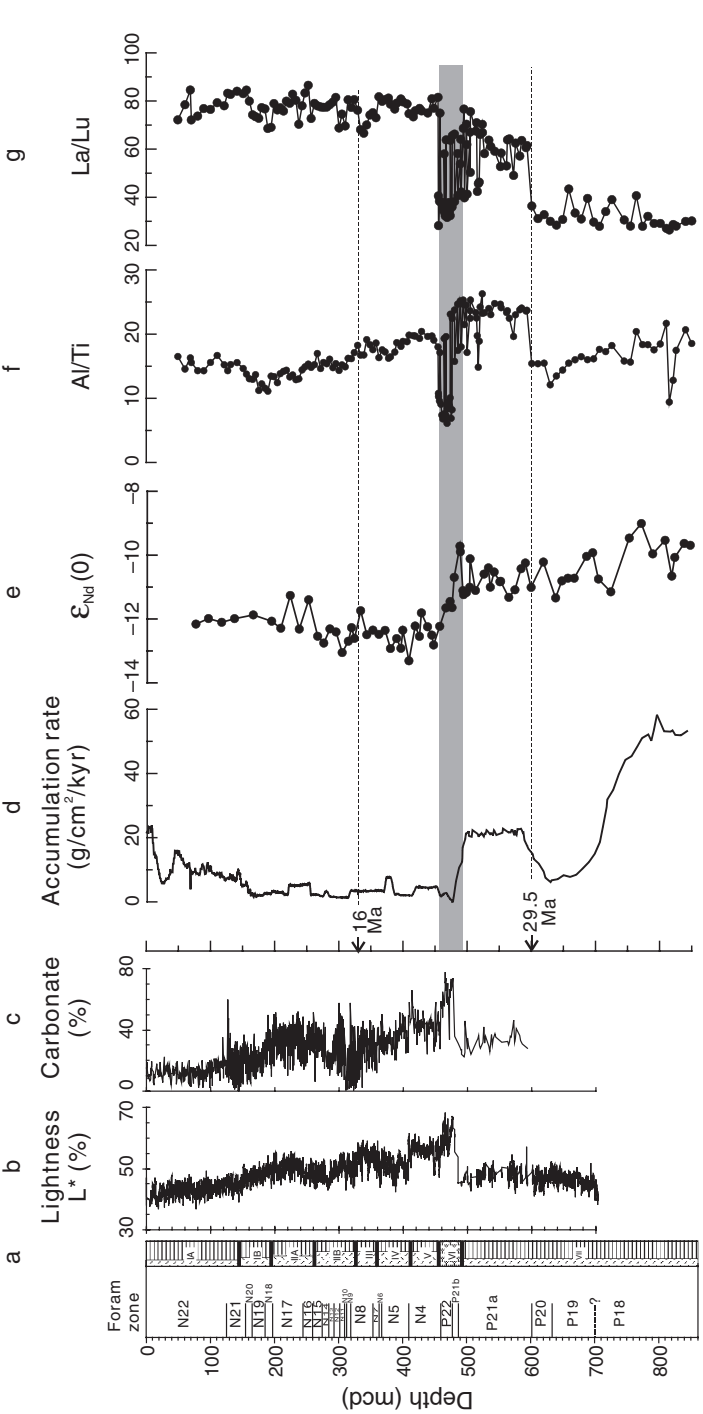

Fig. 5.42 Stratigraphy, lithology and geochemistry at ODP Site 1148 show a sudden change at ~29.5 Ma indicating increased humidity: (**a**) lithological units in Roman numbers, (**b**) color reflectance L^*, (**c**) $CaCO_3$%, (**d**) accumulation rate, (**e**) ε_{Nd}, (**f**) Al/Ti ratio, (**g**) La/Lu ratio (from Wang P. et al. 2003)

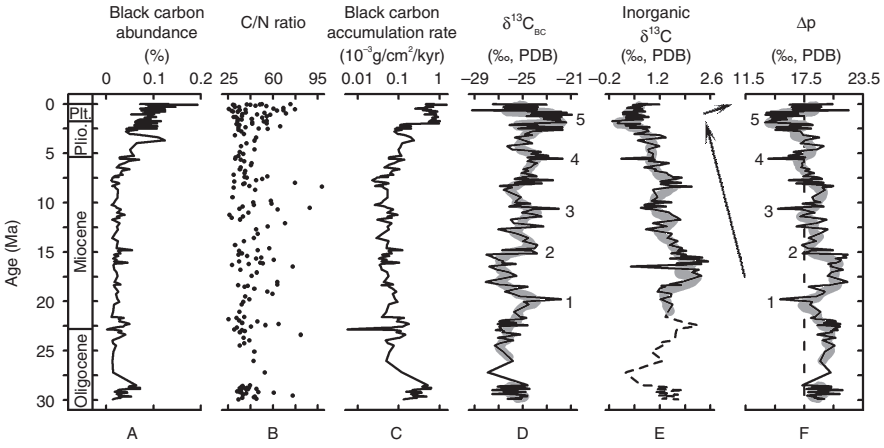

Fig. 5.43 Analytical data from ODP Site 1148 show 5 stages in carbon isotope changes related to monsoon development (Jia et al. 2003). (**A**) Black carbon abundance in dry bulk sediments; (**B**) C/N elemental ratio in treated samples containing black carbon; (**C**) black carbon accumulation rate; (**D**) isotopic composition of black carbon; (**E**) isotopic composition of marine inorganic carbon in planktonic foraminifera (*solid line*) and in bulk carbonate (*dashed line*); (**F**) difference (Δ_P) between atmospheric $\delta^{13}C$ and $\delta^{13}C_{BC}$. *Thick gray lines* in D, E, and F are 5 point running averages. PDB = Peedee belemnite; Plio = Pliocene; Plt = Pleistocene

the East Asian summer monsoon intensification since the early Miocene (Fig. 5.43; Jia et al. 2003).

Noteworthy is that the integrity of each monsoon proxy depends on the extent to which it responds to monsoon forcing only or, if influenced also by non-monsoon processes, the extent to which this additional signal can be identified and removed. Examples include the difficulty in differentiating the monsoon signal from the sea level signal when interpreting the deep-sea pollen record (Sun et al. 2003; Wang P. et al. 2005). For these reasons a multi-proxy approach is often employed, an example is the summer monsoon factor for the northern Arabian Sea based on factor analyses of five proxies: lithogenic grain size, Ba accumulation rate, $\delta^{15}N$, abundance of *G. bulloides* and opal mass accumulation rate (Clemens and Prell 2003). While the multi-proxy approach is clearly useful in that it provides a means of accounting for problems associated with multiple mechanisms influencing individual proxies, it does not replace the need for detailed understanding of the mechanisms influencing individual proxies.

The key to reliable paleoclimate reconstruction is an exact understanding of the various processes contributing to variance in any specific climate proxy. One means of accomplishing this is through long-term sediment trap studies. Careful analyses and applications of the sediment trap data will significantly improve our knowledge of monsoon proxies. However, it must be kept in mind that sediment trap results do not include many processes which take place during and after deposition which can strongly distort the integrity of a climate proxy signal. In addition, the majority of trap deployments is of short duration (two years or

less) and limited to one or two trap locations. Long-duration efforts are required to record the entire range of climate variability associated, for example, with El Niño. Short duration efforts of a year or two cannot record the entire range of variability necessary to evaluate proxy response under the full range of modern climate conditions. Multiple traps are required to record gradients which are often prevalent and important in regions of large variability such as the monsoon influenced regions.

High-quality core-top data sets are another base to establish and evaluate monsoon proxies. An example is the distribution of planktonic foraminiferal species in the northern Indian Ocean based on analyses of 251 core-top samples (Cullen and Prell 1984). This survey not only illustrated the link between *G. bulloides%* and monsoon-driven upwelling, but also brought to light the alteration of planktonic foraminiferal assemblages by carbonate dissolution. Similar work has been done for planktonic foraminifera (Pflaumann and Jian 1999) and pollen (Sun et al. 1999) in the SCS, but the number of sites is relatively low. In general, there are too few core-top data-sets published for the Asian monsoon region, and continued work on systematic core-top analyses to further refine monsoon proxies should be a high priority.

Tectonic-Scale Long-Term Evolution

Long-term monsoon records have been developed from DSDP/ODP cruises to the Indian Ocean and the Mediterranean sea (Legs 22, 24, 115, 116, 117, 121), as well as from studies of the Chinese Loess Plateau. Early monsoon studies in the SCS, however, were limited to the late Quaternary (Sarnthein et al. 1994; Wang L. et al. 1999a) until ODP Leg 184 in 1999, which has enabled us to study the long-term evolution of summer and winter monsoons. The first question to be answered is how far the East Asian monsoon history can be traced back.

Onset of the East Asian Monsoon System

The monsoon upwelling indicator, *Globigerina bulloides*, significantly increased only about 8.5 Ma at ODP Site 722, Arabian Sea (Kroon et al. 1991; Prell et al. 1992). In age, this is very close to the rapid ecological transition from C_3-dominated to C_4-dominated vegetation about 7.4–7.0 Ma, as revealed by the $\delta^{13}C$ data of pedogenic carbonates from northern Pakistan in the Himalayan foreland, and interpreted then as marking the origination or intensification of the Asian monsoon system (Quade et al. 1989). Numerical modeling supports the hypothesis of intensified uplift of the Tibetan Plateau around 8 Ma causing enhanced aridity in the Asian interior and the onset of the Indian monsoon (Prell and Kutzbach 1997). The loess-paleosol profile in China extended the history of the monsoon from 2.6 back to 7–8 Ma (Sun D. et al. 1998; Ding et al. 1998; An et al. 2001). However, the recent discovery of the Miocene loess-paleosol profile at Qin'an, western Loess Plateau,

indicates that the East Asian monsoon could be traced back to 22 Ma at the least (Guo et al. 2002).

There is yet no deep-sea data to discern the East Asian monsoon history over the entire late Cenozoic because pollen records from the SCS are limited only to the Oligocene and the Quaternary, although the longest sediment record of Leg 184 (Site 1148 on the lowermost northern slope) spans the last 32 myr. At Site 1148, a suite of element ratios such as Al/Ti, Al/K. Rb/Sr and La/L, indicative of the intensity of chemical weathering, increased abruptly around 29.5 Ma, in an early seafloor spreading stage of the SCS (Fig. 5.42). This event implies an increase in humidity, but whether it was related to the first East Asian monsoon is not clear (Wang P. et al. 2003).

A 30 myr long stable isotopic record of marine-deposited black carbon from regional terrestrial biomass burning from ODP Site 1148 of the northern SCS reveals photosynthetic pathway evolution of terrestrial ecosystems in the late Cenozoic. This record revealed 5 positive excursions and indicates that C_3 plants negatively adjusted their isotopic discrimination and C_4 plants appeared gradually as a component of land vegetation in East Asia since the early Miocene (21–22 Ma). This record coincides with the Qin'an Miocene loess profile in geological time (Guo et al. 2002), but significantly predates the 7–8 Ma age of sudden expansion of C_4 plants in Pakistan during the late Miocene and Pliocene (Fig. 5.43). The changes in terrestrial ecosystems with time can be reasonably related to the evolution of East Asian monsoons (Jia et al. 2003), although this evidence cannot be conclusive as the C_4 plants expansion may be caused by factors other than monsoon.

Sun and Wang (2005) compiled available marine records from the South and East China Seas together with profiles from onshore basins of China to approach the Cenozoic evolution of the East Asian monsoon. From 125 off- and on-shore sites with pollen and paleobotanical data collected, plus lithological indicators from all over the country, the distribution patterns of arid versus humid climates were reconstructed for five epochs. The results support the model that a broad arid zone was stretching across China in the Paleogene, but retreated to northwest by the end of the Oligocene, indicating the transition from a planetary to a monsoonal system in atmospheric circulation over the region. A variety of evidence, such as the Qin'an Miocene loess profile (Guo et al. 2002), the monsoonal Miocene mammalian fauna discovered in Southeast Asia (Ducrocq et al. 1994), and paleo-climate modeling (Ramstein et al. 1997), all support the existence of the Asian monsoon before the early Miocene. However, these new data do not support an onset of the Asian monsoon system around 8 Ma (Prell and Kutzbach 1997). Rather, the new data led to a hypothesis that the transition to the monsoon climate system in East Asia occurred in the latest Oligocene. The reorganization of the climate system, the appearance of C_4 plants and the increase in humidity in East Asia around the Oligocene/Miocene boundary provide evidence for the establishment of the modern East Asian monsoon. Since then, the Neogene has witnessed significant variations of the monsoon system, including enhancement of aridity and monsoon intensity around 8 Ma and 3 Ma. Thus, the Asian monsoon system has a longer history than previously thought (Wang P. et al. 2005; Sun and Wang 2005).

Development of the East Asian Monsoon System

No remarkable change in sediment accumulation was found at ODP Leg 184 sites in the SCS around 8 Ma (Wang P. et al. 2000). In oceans, the monsoon-driven upwelling can lead to increased productivity and shoaled thermocline. Important faunal signals of strengthened monsoons include abundance increases in productivity-indicative planktonic foraminifera due to upwelling and decreases in the percentage of planktonic foraminifera living in the mixed layer because of a shoaled thermocline. As already mentioned (see "Monsoon proxies"), the relative abundance of *G. bulloides* is a good proxy of upwelling-related high productivity in the Arabian Sea, but it never shows high abundance in the SCS. Instead, the percentage of *N. dutertrei* better unveils the monsoonal variability. According to previous studies and comparison of various stable isotope measurements, species of *Globigerinoides*, *Globigerinita*, and *Globigerina* comprise the major part of shallow water dwellers in the mixed layer. Figure 5.44 plots the variations of *N. dutertrei*% and shallow water dwellers% at Site 1146 in the northern SCS over the past 12 myr. It shows that *N. dutertrei*% increased abruptly at 7.6 Ma, and further increased from 3.2 to 2.0 Ma. Opposite to this trend are an abrupt decrease in the shallow water dwellers% after 8 Ma and a further decrease from 3.2 to 2.0 Ma, although their abundance has also been affected by carbonate dissolution around 11 Ma (Wang P. et al. 2003). Together, these planktonic foraminiferal results indicate paleo-monsoon enhancements at 8–7 Ma and 3.2–2.0 Ma.

The strengthening of the summer monsoon around 8 Ma is also supported by the increase in Pyloniid radiolarians at Site 1143 (Chen et al. 2003). Considering

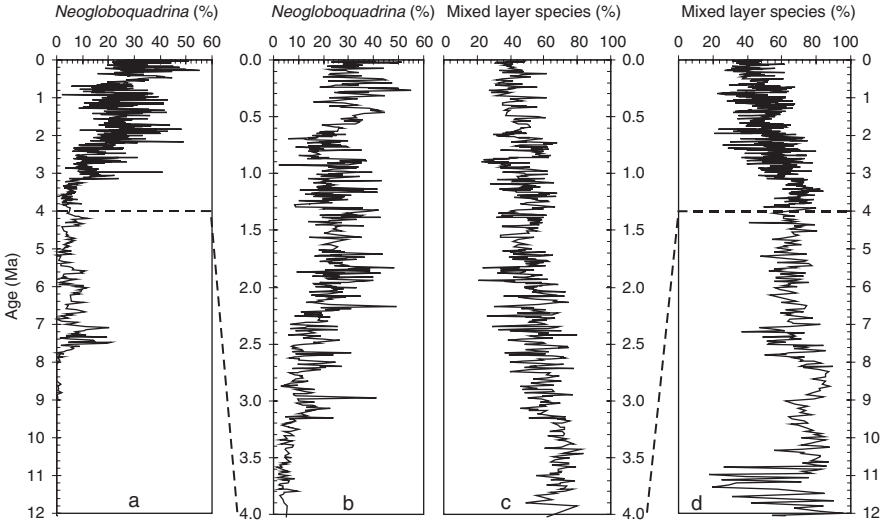

Fig. 5.44 Downcore variations of planktonic foraminiferal percentages at ODP Site 1146 show major changes at ~8 Ma and since ~3 Ma: (**a, b**) *Neogloboquadrina dutertrei*%; (**c, d**) mixed layer shallow-water species% (Wang P. et al. 2003)

the first obvious strengthening of the Indian monsoon at 8 Ma broadly concurred with the initiation of the Red Clay eolian deposition on the loess plateau, the SCS results confirm a significant enhancement of the Asian monsoon system around 8 Ma. Further development of monsoons from 3.2 to 2.0 Ma was also manifested by the increase of opal abundance at Site 1143 (Li J. et al. 2002) and by drastic coarsening of terrigenous clastic grain size due to intensified eolian transportation (Ding et al. 1992). Judging from the modern planktonic foraminiferal $\delta^{13}C$ distribution in the region, the prominent decrease in planktonic $\delta^{13}C$ at Site 1148 from 3.1 to 2.2 Ma was likely responding to the intensification of the winter monsoon (Jian et al. 2003). In the modern SCS, winter monsoons exert a major influence on the variation of productivity and thermocline depth. Therefore, the Leg 184 monsoonal proxies discussed above are interpreted as result of the intensification of the winter monsoon caused by the growth of boreal ice sheets.

The enhancements of the East Asian monsoon at 8–7 Ma and 3.2–2.0 Ma correspond well to the Indian monsoon records (Prell et al. 1992). Zheng H. et al. (2004) compared the monsoonal records from the Indian Ocean, Loess Plateau, the SCS and the North Pacific, and found that intensification of Asian aridity and monsoons around 8 Ma and 3 Ma ago has been convincingly documented both on land and in the ocean, which display similar stages in the development of the East and South Asian monsoons (Fig. 5.45), with an enhanced winter monsoon over East Asia being the major difference (Wang P. et al. 2003). Increased aridity around 8–7 Ma was recorded also in the North Pacific as a peak in dust accumulation rate (Rea et al. 1998), but this interval of higher dust accumulation was not sustained, unlike the younger record of a major dust increase since about 3.5 Ma (Fig. 5.45).

The number and geographic coverage of monsoon records decrease with increasing age and thus our knowledge of pre-Quaternary monsoon history remains relatively poor. Only long records will provide the opportunity to test the numerous hypotheses regarding the long-term history of the East Asian monsoon and the relative roles played by uplift, sea-land distribution and oceanic gateways. Therefore, we need more long and high-quality marine records from the SCS, including hemipelagic and lacustrine sediments of Miocene and Paleogene age.

Orbital-Scale Variability

Late Pliocene Monsoon Variations

Orbital-driven monsoon variations in the Pliocene can be demonstrated with isotopic records from ODP sites in the SCS. The period from 3.3 to 2.5 Ma in the late Pliocene is characterized by a continuous increase of global ice volume as recorded by a trend of positive shift in benthic $\delta^{18}O$. The planktonic $\delta^{18}O$ level, however, remains relatively constant, resulting in an increasing difference between benthic and planktonic isotopes (Jian et al. 2003; Tian et al. 2006). To test the connection of the isotopic signals with monsoon variability, the ice volume, water temperature, and salinity effects need to be distinguished first. As already introduced in the section

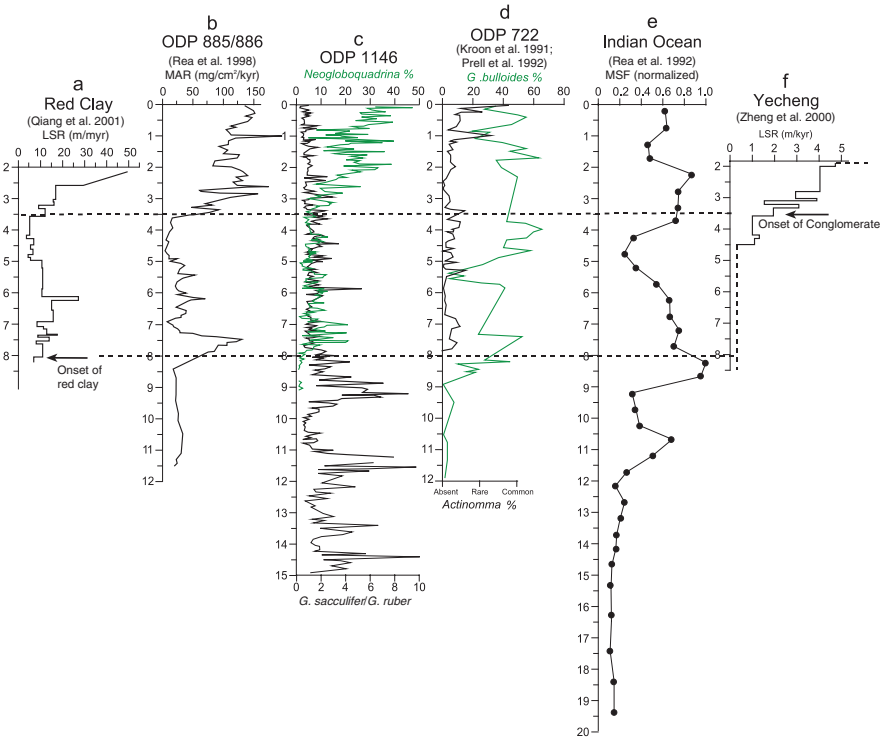

Fig. 5.45 Terrestrial and marine records reveal the monsoon history since the middle Miocene: (**a**) linear sedimentation rate of Jiaxian red clay in the Chinese Loess Plateau; (**b**) mass accumulation rate of eolian flux to the North Pacific (ODP Sites 885/886); (**c**) ratio of abundance of *G. sacculifer* and *G. ruber* (*solid line*) and abundance of *Neogloboquadrina* (*green line*) from the SCS (ODP Site 1146); (**d**) abundance of *G. bulloides* and relative abundance of radiolarian *Actinoma* spp. from the Indian Ocean (ODP Site 722); (**e**) normalized mean sediment flux to the Indian Ocean; (**f**) linear sedimentation rate of Yecheng molass (from Zheng et al. 2004)

"Sea surface temperature history", the paleo-SST at ODP Site 1143 from 3.3 to 2.5 Ma was estimated using the *G. ruber* Mg/Ca ratio (Fig. 5.3). The surface water $\delta^{18}O_{sw}$ can be calculated from the paired-*G. ruber* $\delta^{18}O$ and Mg/Ca ratio-based SST using the *Orbulina* low-light paleotemperature equation (Bemis et al. 1998). The derived $\delta^{18}O_{sw}$ shows a pattern of steady glacial/interglacial cycles from 3.3 to 2.5 Ma, without any obvious long-term trends (Tian et al. 2006). Since the $\delta^{18}O_{sw}$ depends both on global ice volume and water salinity, the regional sea surface salinity (SSS) variations can be estimated by removing the ice volume effects from the $\delta^{18}O_{sw}$, i.e., the residual $\Delta\delta^{18}O_{sw\text{-}b}$. The $\Delta\delta^{18}O_{sw\text{-}b}$ of Site 1143 was obtained by subtracting the benthic foraminiferal $\delta^{18}O$ from the calculated $\delta^{18}O_{sw}$. The derived $\Delta\delta^{18}O_{sw\text{-}b}$ shows a stepwise decrease during the period of significant ice sheet growth 3.3–2.5 Ma ago (Fig. 5.46C) (Tian et al. 2006).

The $\Delta\delta^{18}O_{sw\text{-}b}$ reflects SSS variations at Site 1143, which are associated with regional changes of precipitation and fluvial runoff in the southern SCS region. The

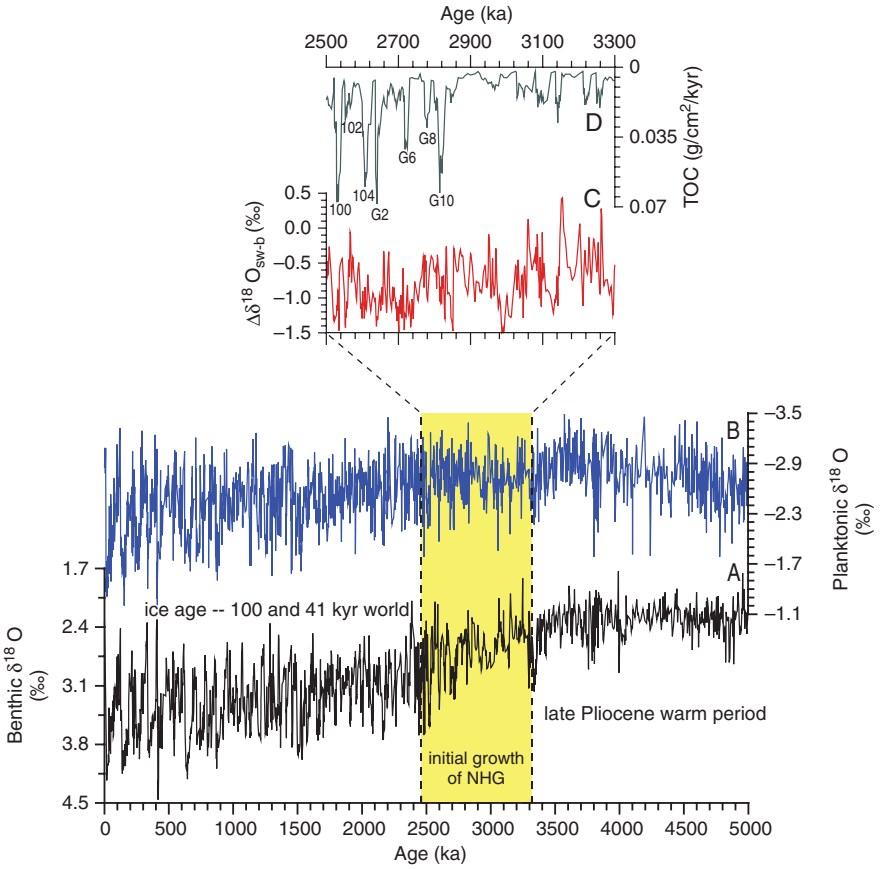

Fig. 5.46 Paleo-monsoon records from ODP Site 1143 show monsoon-driven salinity changes in the period of 2.5–3.3 Ma when Northern Hemisphere Glaciation (NHG) started: (A) *Cibicidoides* $\delta^{18}O$ for the past 5 myr, (B) *G. ruber* $\delta^{18}O$ for the past 5 myr, (C) $\Delta\delta^{18}O_{sw\text{-}b}$, the difference between sea water $\delta^{18}O$ and *Cibicidoides* $\delta^{18}O$, (D) total organic carbon mass accumulation rate, with marine isotope stages indicated (from Tian et al. 2006)

ice sheet growth caused an overall long-term sea level lowering of ~43 m (Mudelsee and Raymo 2005), which shortened the distance between Site 1143 and the continent, leading to a local decrease of SSS. Meanwhile, strengthened East Asian summer monsoons increased the annual mean precipitation in and the fluvial runoff to the southern SCS, which in turn resulted in SSS decreases at Site 1143. Thus, the $\Delta\delta^{18}O_{sw\text{-}b}$ variations from 3.3 to 2.5 Ma may reflect a stepwise development of the East Asian monsoons (Fig. 5.46C).

The down-core measurements of TOC flux at Site 1143 show clear glacial/interglacial cycles from 3.3 to 2.5 Ma, with higher values during glacial periods and lower values during interglacial periods (Fig. 5.46D). Just after 2.82 Ma (MIS G10), the amplitude of the TOC flux fluctuations within a glacial/interglacial cycle rapidly

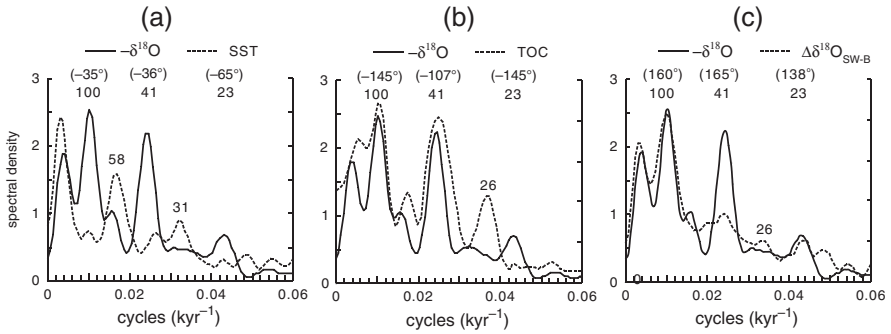

Fig. 5.47 Spectral analyses of *Cibicidoides* $-\delta^{18}O$ and Mg/Ca-derived SST, TOC and $\Delta\delta^{18}O_{sw\text{-}b}$ records from ODP Site 1143 reveal major cyclicities for the period of 2.5–3.3 Ma: (**a**) spectrum of $-\delta^{18}O$ (*solid line*) and SST (*dashed line*); (**b**) spectrum of $-\delta^{18}O$ (*solid line*) and TOC (*dashed line*); (**c**) spectrum of $-\delta^{18}O$ (*solid line*) and $\Delta\delta^{18}O_{sw\text{-}b}$ (*dashed line*) (Tian et al. 2006). Numbers denote the phases at the 100 kyr, 41 kyr and 23 kyr bands. Negative phases denote SST leads $-\delta^{18}O$, and positive phases denote TOC or $\Delta\delta^{18}O_{sw\text{-}b}$ lags $-\delta^{18}O$

increased, reaching a level nearly 3 to 4 times the amplitude observed prior to MIS G10 (Fig. 5.46D). As modern productivity in the southern SCS is associated with summer monsoon driven upwelling, the variations of TOC flux at Site 1143 indicate a rapid strengthening of the East Asian summer monsoon after 2.82 Ma. Both TOC flux and $\Delta\delta^{18}O_{sw\text{-}b}$ records reveal a general enhancement of the East Asian monsoons, especially the summer monsoon during the period of the late Pliocene ice sheet growth (Fig. 5.46).

Since SST, TOC and $\Delta\delta^{18}O_{sw\text{-}b}$ all vary someway in response to changes in monsoon intensity, cross-spectrum analyses were carried out between the monsoon proxies and benthic foraminiferal $\delta^{18}O$ (Fig. 5.47). Compared to the benthic $\delta^{18}O$, the SST records show weak variations at the primary orbital periodicities of 100 kyr, 41 kyr and 23 kyr, but relatively strong variations at the periodicities of 58 kyr and 31 kyr. Coherencies at the orbital periodicities are all above the 80% alarm test level, indicating a coherent relationship between the benthic $\delta^{18}O$ and the SST records. Phase relations reveal a lead of the SST changes relative to the global ice volume changes at each cycle (Fig. 5.47a), namely a lead of 35° at the 100 kyr band, equivalent to 9.72 kyr; a lead of 36° at the 41 kyr band, equivalent to 4.1 kyr; and a lead of 65° at the 23-kyr band, equivalent to 4.1 kyr. From 3.3 to 2.5 Ma, the 3–4 kyr lead of SST change at ODP Site 1143 relative to global ice volume signal at both the obliquity and precession bands is similar to that in the early Pleistocene, indicating a stationary phase relationship since the Pliocene.

TOC and $\Delta\delta^{18}O_{sw\text{-}b}$ are spectrally similar to the benthic $\delta^{18}O$, performing strong 100 kyr, 41 kyr and 23 kyr cycles (Fig. 5.47b,c). In addition, both the TOC and $\Delta\delta^{18}O_{sw\text{-}b}$ records show a periodicity of 26 kyr which is within the range of the precession in the Pliocene (Berger et al. 1992). Coherencies above the 80% alarm test level indicate coherent relationship between the benthic $\delta^{18}O$ and these two monsoon-related proxy records at the primary orbital periodicities. However, phase

relations reveal that these two records lag the global ice volume change at the 100 kyr, 41 kyr and 23 kyr bands. The phase offsets between the TOC and the benthic $\delta^{18}O$ record are 145° at the 100 kyr band equating with a lag of 40.2 kyr, and 107° at the 41 kyr band equating with a lag of 12.2 kyr, and 145° at the 23 kyr band equating with a lag of 9.2 kyr (Fig. 5.47b). The phase offsets between the $\Delta\delta^{18}O_{sw\text{-}b}$ and the benthic foraminiferal $\delta^{18}O$ are 160° at the 100 kyr band equating with a lag of 44.4 kyr, and 165° at the 41 kyr band equating with a lag of 18.8 kyr, and 138° at the 23-kyr band equating with a lag of 8.8 kyr (Fig. 5.47c). The cross spectral analyses thus show that the global ice volume change is a factor internal to the climate system with great influence on the variability of East Asian monsoons at least since the Pliocene. In the Pleistocene, monsoon proxy records in the Arabian Sea indicate that the monsoon maximum usually lags the minimum of global ice volume by 2–4 kyr at both the obliquity and precession bands (Clemens et al. 1991, 1996), much smaller than the lag of 8–18 kyr found at Site 1143. The differences reveal a nonstationary phase of the East Asian monsoon relative to the global ice volume in the Plio-Pleistocene. The numerical climate-model experiment reveals that the evolution of the Asian monsoons is linked to phases of Himalaya-Tibetan plateau uplift and to the boreal ice sheet growth (Prell and Kutzbach 1997). Thus, the decreased phase lag at the obliquity and precession bands is possibly linked to the amplified northern hemisphere ice sheets and the increased contrast between glacial and interglacial periods.

To sum up, the data from the southern SCS show important linkage of the East Asian monsoon with both the tropical and high latitude forcings. The records of ODP Site 1143 from the southern SCS reveal that East Asian monsoons gradually strengthened in response to the phased expansion of ice sheets in the high northern latitudes during the late Pliocene, with increased phase offsets at the obliquity and precession bands relative to the late Pleistocene. This finding suggests that the East Asian monsoons are not only simply driven by northern summer insolation at the precession period but also modulated by global ice volume change in high latitudes (Tian et al. 2006).

Pleistocene Monsoon Variations: Glacial/Interglacial Cycles

Compared to the late Pliocene, the Pleistocene displayed much more significant amplitude changes with glacial/interglacial cycles due to a prevalent monsoon climate. In the modern SCS, winter (from December to March) is the season when the average seasonal mixed layer reaches its maximum depth, and the SST decreased to the annual minimum, while the proxies of productivity, including opal%, *P. obliquiloculata* and *G. ruber* flux, organic carbon flux, all exhibit higher values than other seasons (Fig. 5.48). Accordingly, in the Pleistocene, all the monsoon proxies are expected to vary more strongly in glacial than interglacial cycles. Decreased SST and intensified winter monsoon during glacials strengthened the mixing in the upper water and thickened the mixed layer in the region as indicated by decreased $\Delta\delta^{18}O_{(P\text{-}G)}$ values at Site 1143 (Fig. 5.20C).

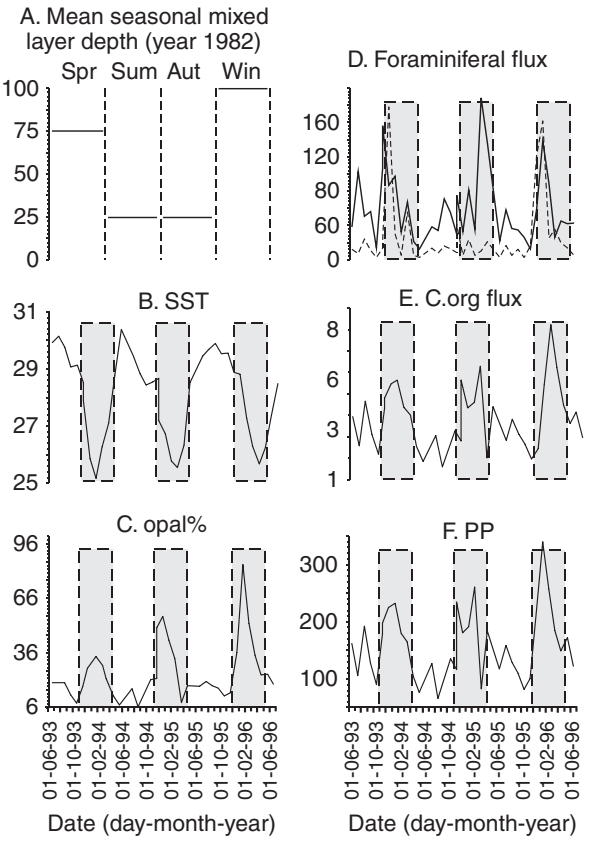

Fig. 5.48 Sediment trap records from the central SCS indicate seasonal changes in all variables, including (**A**) the average seasonal mixed layer depth for the SCS by integrating data from Levitus (1982); (**B**) SST °C; (**C**) opal%; (**D**) *P. obliquiloculata* (*dashed line*) and *G. ruber* (*solid line*) flux, individuals.m^{-2}.d^{-1}; (**E**) organic carbon flux, mg.m^{-2}.d^{-1}; (**F**) primary productivity, mg.m^{-2}.d^{-1} (from Tian et al. 2005b)

A compilation of some monsoon proxies over the last 800 kyr (Fig. 5.49) shows higher herbaceous pollen%, lower $\Delta\delta^{18}O_{(P\text{-}G)}$ values and lower *P. obliquiloculata%* during glacial intervals, indicating intensified winter monsoon in the SCS and southern China. *P. obliquiloculata* is a typical deep dwelling planktonic foraminifer, living in the uppermost part of the thermocline or below the bottom of the mixed layer. Since the sediment trap reveals its high flux (also *G. ruber* flux) corresponding to the deep winter mixed layer, the higher abundances of *P. obliquiloculata* during glacials (Fig. 5.49B) possibly reflect a deeper thermocline associated with cooling climate and intensified winter monsoon (Tian et al. 2005b). However, relating its higher abundances with a deep thermocline in the southern SCS remains to be confirmed because other studies indicate that deep-dwelling species including *P. obliquiloculata* and *Globorotalia tumida* often dominate the planktonic assemblage during times of a shallower surface mixed layer when the thermocline is located within the photic zone (Bé et al. 1985).

Analogous to higher opal concentrations during winter within the annual cycle as revealed in the sediment trap study in the central SCS (Fig. 5.48C), the opal flux at Site 1144 from the northern SCS displays higher concentrations during glacials than

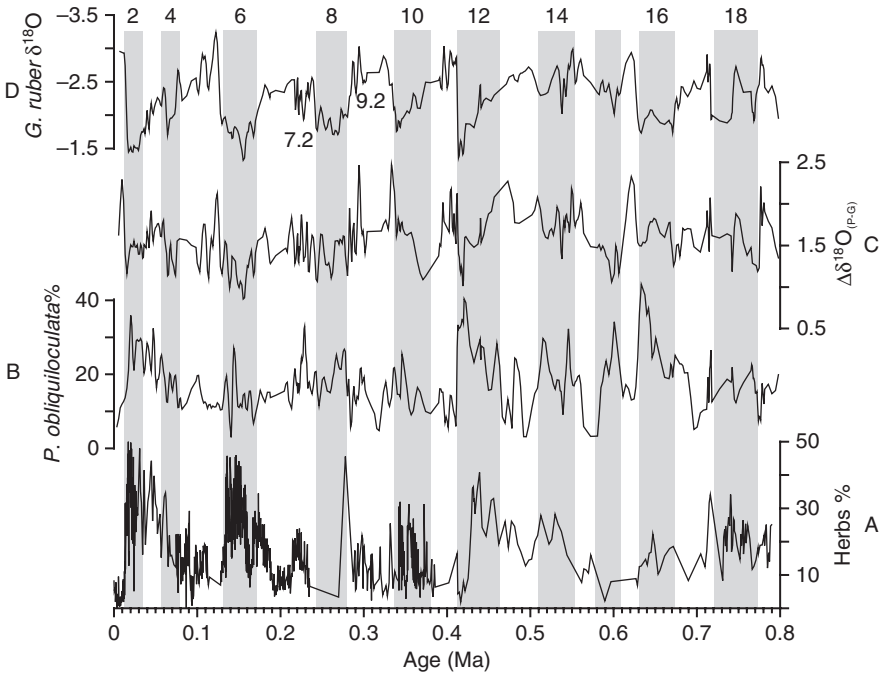

Fig. 5.49 East Asian monsoon proxy records from the SCS show monsoon variations over the last 800 kyr: (A) herbs% of ODP Site 1144 (Sun et al. 2003); (B) *P. obliquiloculata%* of Site 1143 (Xu et al. 2005); (C) $\Delta\delta^{18}O_{(P\text{-}G)}$ of ODP Site 1143 (PDB, ‰, 3-point Gaussian smoothing); (D) *G. ruber* $\delta^{18}O$ of Site 1143 (PDB, ‰, 3-point Gaussian smoothing), with numbers and shaded bars marking cold marine isotope stages (MIS) (Tian et al. 2005b)

during interglacials for the past 1.56 myr (Li and Wang 2004). At a nearby locality, Site 1146, siliceous microfossils also show higher abundances and higher accumulation rates during glacials than during interglacials for the past 1.0 myr (Wang R. et al. 2003). The evidence of increased opal flux and siliceous microfossils together implies higher glacial siliceous productivity in the northern SCS caused by strong East Asian winter monsoon winds. The intensified East Asian winter monsoon winds during glacials likely enhanced the inflow of upwelled nutrient-rich water through Bashi Strait and the transportation of more eolian dust, resulting in nutrient increases and higher productivity in surface waters of the northern SCS (Wang L. et al. 1999a).

Previous studies have revealed that most marine proxies are not associated with any particular climatic variable but with the integration of several variables, and only the variance held in common among several proxies can be attributed to the variable of interest. This approach is most useful when the proxies are of sufficiently different origins (chemical, physical, biological, isotopic) and from an array of sites such that the variance not held in common is largely independent (Clemens and Prell 2003). Although the $\Delta\delta^{18}O_{(P\text{-}G)}$ and *P. obliquiloculata%* of Site 1143, as

well as herbs% and opal flux of Site 1144, show many differences in both long- and short-term variations (Fig. 5.49), they all share common features of strong glacial/interglacial variations that may have been caused by strong winter monsoons during glacials.

Therefore, the main implication of the $\delta^{18}O$ differences between *G. ruber* and *P. obliquiloculata* from Site 1143 is that an intensified East Asian winter monsoon was the primary factor affecting upper ocean thermal gradient variations, especially the mixed layer depth or the thermocline depth in the southern SCS during the Pleistocene. This conclusion differs from faunal-climate records from the East Pacific where the cool sea surface and the shoaled thermocline are driven by wind-induced upwelling. The hydrologic feature of a deep mixed layer or thermocline driven by strong winter monsoons in the SCS, as demonstrated by modern observations and comparisons between paleo-climate proxies, seems to be unique in marginal seas where upwelling is weak but monsoon influence is strong.

Pleistocene Monsoon Variations: Coherence and Phase Relationship

Clemens et al. (1991) found that the Earth's geometry (ETP, eccentricity+obliquity-precession) serves as the external forcing of the Indian Ocean summer monsoon whereas the latent heat across the equator from the southern Indian Ocean to the northern serves as the internal forcing. In addition, they also found that the global ice volume changes have little impact on the evolution of the Indian Ocean summer monsoon, conflicting with the GCM simulations (Kutzbach and Guetter 1986; Prell and Kutzbach 1987). Later, Wang L. et al. (1999a) considered that the East Asian monsoon probably had a similar forcing mechanism to that of the Indian Ocean summer monsoon based on several short and mainly low resolution proxy records from the SCS. Cores from ODP Leg 184 sites provide high quality and long sediment records, which enable a test of this hypothesis by examining all available faunal, floral and geochemical proxies, especially the coherency and phase relationship of the East Asian Monsoon with orbital forcing and global ice volume changes during the Pleistocene.

ODP Site 1143 in the southern SCS. The flux of opal (including radiolarians and diatoms) usually reflects modern ocean productivity (Dickens and Barron 1997), and monsoon-driven upwelling can enhance the siliceous productivity of the upper ocean. In the Indian Ocean, opal flux indicates changes in the intensity of the Indian summer monsoon. Similarly in the SCS, the siliceous productivity indicated by Opal% is also related to the East Asian monsoon changes (Wang and Li 2003; Wang R. et al. 2003). Sediment trap studies in the northern and central SCS show opal flux peaking in both winter and summer monsoon seasons (Tian et al. 2004). At Site 1143, the opal% is lower before 400 ka, ranging from 1.5 to 2.5%, with a smaller glacial/interglacial amplitude; after 400 ka, it increases abruptly from 1.5 to 6.0%, with a larger glacial/interglacial amplitude (Fig. 5.50). In general, the opal% of Site 1143 is lower during glacials but higher during interglacials, indicating stronger summer monsoon during interglacials.

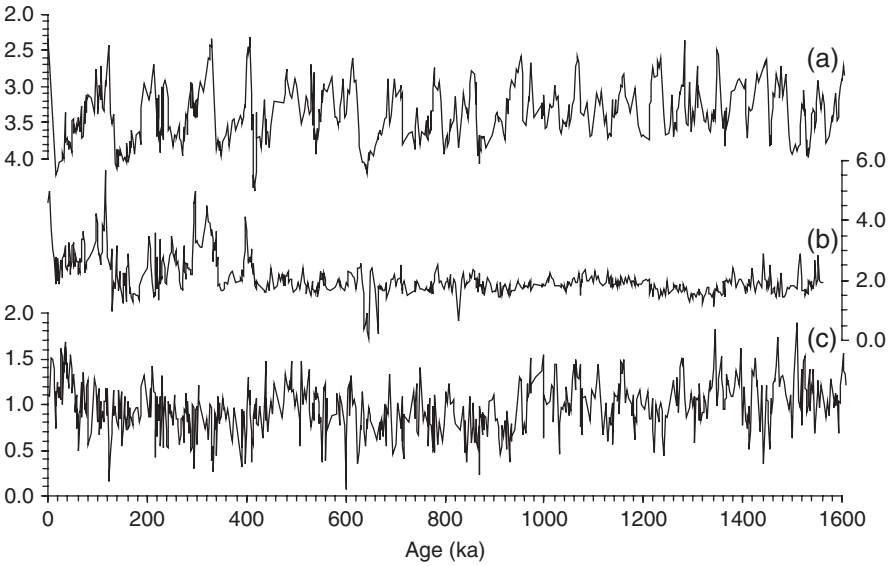

Fig. 5.50 Paleo-climate records of ODP Site 1143 show monsoon variations over the past 1.6 myr in the southern SCS: (**a**) benthic foraminiferal *Cibicidoides* $\delta^{18}O$ (‰, PDB) (Tian et al. 2002); (**b**) opal percentage (%) (Wang and Li 2003); (**c**) planktonic foraminiferal *G. ruber* $\delta^{13}C$ (‰, PDB) (Tian et al. 2005a)

When the nutrient-rich subsurface water upwells to the surface by the monsoon, the $\delta^{13}C$ of the sea surface water will decrease. If the foraminiferal shell equilibriums with the ambient water during the process of its calcification, the changes of the shell's $\delta^{13}C$ should record the changes of the monsoon intensity. In the SCS, in the upwelling areas off the northwest coast of the Philippines and off the east coast of Vietnam, the *G. ruber* $\delta^{13}C$ and *P. obliquiloculata* $\delta^{13}C$ in core-top samples show relatively lower values than in other areas (Wang L. et al. 1999). The planktonic foraminifer *G. ruber* $\delta^{13}C$ for the past 1.6 myr varies from 0.2 to 2.0‰ (Fig. 5.50). Although the glacial/interglacial change of *G. ruber* $\delta^{13}C$ is not as obvious as that of the benthic $\delta^{18}O$, the high-frequency and large amplitude fluctuations in the *G. ruber* $\delta^{13}C$ of Site 1143 may reflect productivity variations related to monsoon variability.

ODP Site 1144 in the northern SCS. The herbs and *Pinus* found in the deep sea sediments of Site 1144 were probably transported by strong winter monsoon-driven currents (Sun et al. 2003), and thus can be used as the proxies of the East Asian winter monsoon. The abundance sum of these two groups exceeds 50% in most samples and they always show a reverse relationship with higher *Pinus%* in interglacials and higher herbs% in glacials (Fig. 5.25), indicating strengthened winter monsoon during glacials and weakened winter monsoon during interglacials (see detailed discussion in section "Vegetation history in deep-sea record" above).

Coherencies and phases of monsoonal proxy records with orbital and global ice volume forcing. Cross spectral analyses indicate that the pollen records of the

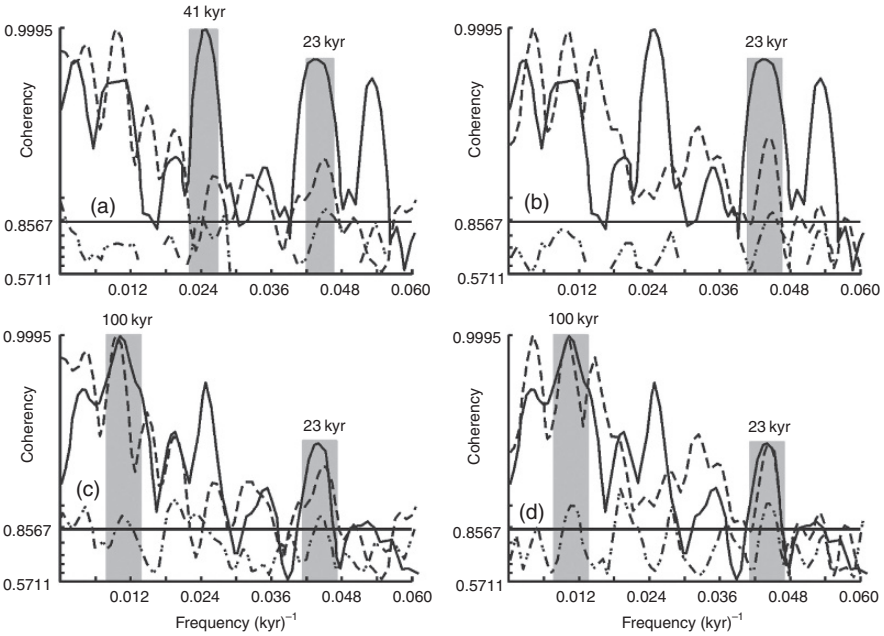

Fig. 5.51 Cross spectral analyses of the pollen records of ODP Site 1144 (0–1 Ma) with the orbital forcing (ETP) and the global ice volume variations ($\delta^{18}O$) show dominant orbital periods at 100 kyr, 41 kyr and 23 kyr (*grey bars*) where high coherencies are present: (**a**) ETP vs herbs%; (**b**) ETP vs *Pinus%*; (**c**) $\delta^{18}O$ vs herbs%; (**d**) $\delta^{18}O$ vs *Pinus%* (Tian et al. 2005a). *Solid lines* denote the spectrums of ETP or $\delta^{18}O$. *Dashed lines* denote the spectrums of the pollen records. *Dotted dashed line* denotes coherency. The *horizontal solid lines* denote the coherencies above 80% standard level

past 1 myr (Herbs% and *Pinus%*) at ODP Site 1144 demonstrate strong variances at the 100 kyr band and moderate to strong variance at the 41 kyr and 23 kyr bands, but they are coherent with the orbital forcing (ETP) only at the 23 kyr precession band (Fig. 5.51). The upper ocean temperature contrast in the southern SCS is also coherent with the ETP only at the precession band (Tian et al. 2004), as also in the east tropical Pacific (Ravelo and Shackleton 1995). These indicate that the tropical climate is externally controlled by the precessional radiation.

The herbs% and *Pinus%* are highly coherent with the global ice volume change (represented by foraminiferal $-\delta^{18}O$) at the 100 kyr and the 23 kyr bands (Fig. 5.51c,d). Though the cross spectrum between the pollen and the $\delta^{18}O$ records show no coherent relationship at the 41 kyr band, a highlighted coherency stands at the 54 kyr band, a heterodyne frequency of the primary orbital periods. A similar coherent relationship at the 54 kyr band also exists between the Indian Ocean monsoon tracers and the concentration of the orbital variance (Clemens et al. 1991). The 100 kyr glacial cycles are dominant in the Earth's Pleistocene climate records (Imbrie et al. 1992), especially in the foraminiferal $\delta^{18}O$ records. Both the herbs% and the *Pinus%* of Site 1144 display perfect glacial/interglacial variations for the past 1 myr. The graphic structure of the pollen records, which is identical to that

of the $\delta^{18}O$, in conjunction with the cross spectral analyses, indicate that the East Asian winter monsoon has been greatly influenced by and coherent with the global ice volume change. The inference is consistent with the conclusions drawn from the loess-paleosol sequence (An et al. 2001) and from the north Pacific dust concentration (Rea et al. 1998) as well as from numerical simulations (Kutzbach and Guetter 1986). As the other important component of the Asian monsoon system, the Indian Ocean summer monsoon appears to be different, with proxies not coherent with the global ice volume change at the 100 kyr band but coherent at the 41 kyr and the 23 kyr bands. In addition, the fact that the ice-volume minima (maximum effectiveness of sensible heating) lag the Indian Ocean summer monsoon maxima by 33 kyr over the eccentricity band, excludes a forcing-response relationship between the Northern Hemisphere Glaciation and the Indian Ocean summer monsoon changes (Clemens et al. 1991).

Both *G. ruber* $\delta^{13}C$ and opal% of Site 1143 are coherent with the concentration of orbital variances at the three primary orbital cycles, the 100 kyr, the 41 kyr and the 23 kyr bands (Fig. 5.52a,b). Particularly, the coherency of *G. ruber* $\delta^{13}C$ with the ETP at the 23 kyr precession band is the highest, nearly two times the coherency

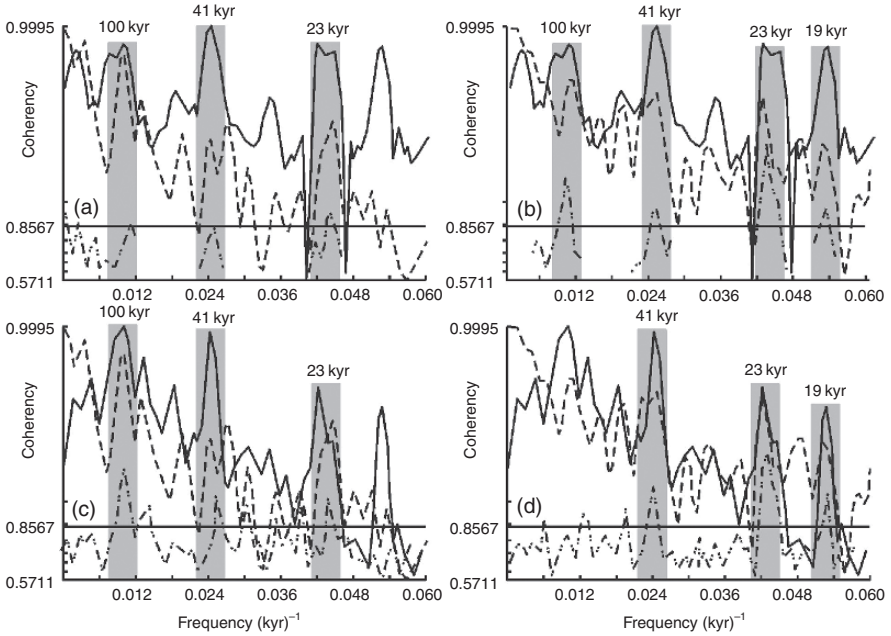

Fig. 5.52 Cross spectral analyses of *G. ruber* $\delta^{13}C$ and opal% of ODP Site 1143 with the orbital forcing (ETP) and the global ice volume variations ($\delta^{18}O$) show dominant orbital periods at 100 kyr, 41 kyr and 23 kyr (*grey bars*) where high coherencies are present over the last 1.6 myr: (**a**) ETP vs opal%; (**b**) ETP vs $\delta^{13}C$; (**c**) $\delta^{18}O$ vs opal%; (**d**) $\delta^{18}O$ vs $\delta^{13}C$ (Tian et al. 2005a). *Solid lines* denote the spectrums of ETP or $\delta^{18}O$. *Dashed lines* denote the spectrums of the proxy records. *Dotted dashed line* denotes coherency. The *horizontal solid lines* denote the coherencies above 80% standard level

at the eccentricity or obliquity bands. Also, the coherency of opal% with the ETP at the 23 kyr precession band is the highest among the three coherencies. These mean that the strongest responses of the East Asian monsoon to the orbital forcing occur at the precession band. This kind of relationship between the East Asian monsoon proxies and the orbital forcing highlights the precession as the primary force driving the tropical climate change. The opal% of Site 1143 is also highly coherent with the $-\delta^{18}O$ at the three primary orbital cycles; in addition, the *G. ruber* $\delta^{13}C$ is also strongly coherent with the -$\delta^{18}O$ at the 41 kyr band and the two precession bands (23 kyr and 19 kyr). Though the coherency of *G. ruber* $\delta^{13}C$ with the $-\delta^{18}O$ at the 100 kyr band does not exceed the 80% statistical level, a strong 100 kyr cycle also occurs in its spectrum. The coherent relationship of the opal% and *G. rube*r $\delta^{13}C$ with the $-\delta^{18}O$ is consistent with that between the pollen records and the $-\delta^{18}O$ at Site 1144 (Fig. 5.51c), revealing a close relationship between the East Asian monsoon variations and global ice volume changes.

Cross spectrum analysis has also revealed the phase relationships of the proxies with the orbital variance (ETP) at the orbital cycles. At the 100 kyr band, the opal% leads the ETP by $2.9^\circ \pm 2.4^\circ$, close to zero, while the pollen records are not coherent with the ETP, but in phase with $-\delta^{18}O$. Again, this indicates that the East Asian winter monsoon is greatly influenced by the global ice volume change. At the 41 kyr band, all monsoon tracers and the global ice volume change are coherent with the concentration of the ETP. Their phases relative to the ETP are close to each other if the phase errors are considered. This means that the orbital forcing has almost the same controls over the East Asia monsoon and the global ice volume change at the 41 kyr band. At the precession band, the phases of the monsoon proxies relative to ETP are overall much closer at the precession band than at the obliquity band, but they departure away from the phase of the $-\delta^{18}O$ relative to the ETP (see Tian et al. 2005a for further details).

Suborbital-Scale Variability

Paleomonsoon research was initiated with efforts to understand links between changes in monsoon intensity and large-scale boundary conditions such as orbital forcing and changes in global ice volume. These remain active areas of research. However, ice cores from Greenland have revealed records of climate change on far shorter time scales as well (Dansgaard et al. 1993; Grootes and Stuiver 1997). Now, it has been revealed that decadal- to millennial-scale climate variability is a global phenomenon, which was not limited to the ice cores and high latitudes of the North Atlantic, but also extended to other regions such as the tropical Pacific and monsoonal Asia. Millennial-to-centennial- scale variations have been extensively reported in the monsoon climate, including in the SCS, and a number of conceptual models are under development in efforts to constrain the forcing mechanisms underlying short-term changes in monsoon climate. Most hypothesize that the short-term changes in monsoon intensity are linked to internal oscillations in thermohaline circulation as well as atmospheric energy and moisture transfer. In some

cases, a link to millennial- and centennial-scale variations of solar activity has been made on the basis of variations in ^{10}Be flux and ^{14}C production (Bond et al. 2001; Schulz and Paul 2002; Sarnthein et al. 2002). Exploration of the tidal influences on monsoon variability, like the solar cycles, has also been discussed (e.g. Fairbridge 1986). Because very high-resolution records are requested for reconstructing the sub-orbital variations in monsoon climate, only fragmentary pieces of information from the Pleistocene history are available so far in the SCS.

Millennial-Scale Cycles in the Middle Pleistocene

It has been found that the rapid climate changes occurred not only in the last glacial stage, but also in the Holocene in Asian monsoon regions (Schulz et al. 1998; Wang L. et al. 1999a; von Rad et al. 1999), implying that the decadal- to millennial-scale climate variability operates independently of the glacial/interglacial climate cycle. Similarly, sub-orbital climate fluctuations existed beyond the late Quaternary.

McManus et al. (1999) reported the millennial-scale climate variability throughout the past 500 kyr according to the changes of the ice rafted debris in the North Atlantic. Almost at the same time, Raymo et al. (1998) found that the millennial-scale climate variability can be traced back to 1.2 Ma. They claimed that millennial-scale climate instability may be a pervasive and long-term characteristic of Earth's climate, rather than just a feature of the strong glacial/interglacial cycles of the past 800 kyr. These findings fundamentally altered the way Earth scientists thought about the operation of the Earth's climate system and the relative sensitivity of this system to major climatic shifts.

In the SCS, ODP Site 1144 is distinguished by extremely high sedimentation rate in the last 1 myr (Bühring et al. 2001). Its ultrahigh-resolution color reflectance (L^*) data (4 cm interval; time resolution of $\sim$10 yr), as a proxy of carbonate content in deep sea sediments (Sarnthein et al. 1994), provide a unique possibility to study millennial-scale climate variability during the middle Pleistocene climate transition (MPT).

Figure 5.53 shows the results of wavelet spectral analysis of the color reflectance (L^*) data of Site 1144 based on the oxygen isotopic stratigraphy of Bühring et al. (2001), which demonstrate that the D/O-like millennial-scale climate fluctuations existed throughout the glacial, deglacial and postglacial stages over the last 1 myr (Jian and Huang 2003). Of particular interest is that after the mid-Pleistocene revolution (MPR) at 900 ka, along with the strengthening of the East Asian winter monsoon, the signal of millennial-scale climate fluctuations became stronger during glacial stages. Before the MPR, the signals of millennial-scale climate fluctuations were relatively stronger during interglacials, but after the MPT they became relatively stronger during glacials. It seems that the MPT was reflected not only by a change in dominant climate periodicities from 41 to 100 kyr, but also by a change in the characteristics of millennial-scale climate fluctuations. Although the new results need further evidence from high-resolution isotope analyses, it illuminates that orbital and millennial/centennial scale climate changes are interwoven between

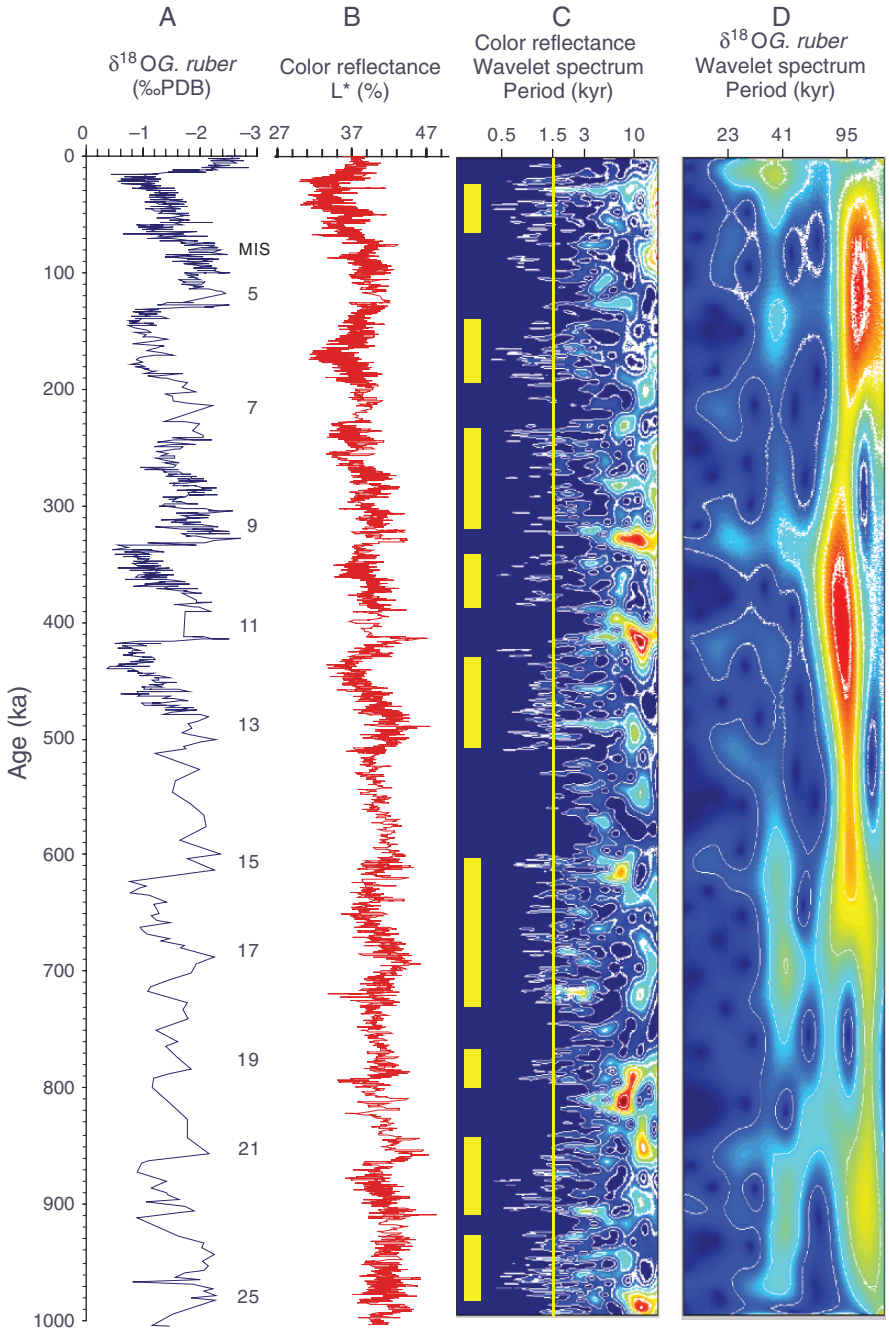

Fig. 5.53 Wavelet spectra of the $\delta^{18}O$ (**A, D**) and the color reflectance L* (**B, C**) show orbital and suborbital changes at ODP Site 1144 (Jian and Huang 2003). Number in (**A**) denotes interglacial marine isotopic stages (MIS). *Vertical yellow line* in (**C**) indicates the period of 1.5 kyr, and *short yellow bars* indicate intervals with strong millennial-scale climate fluctuations

them. This is very important for understanding the sub-orbital variability of the Asian monsoon system.

Dansgaard-Oeschger Cycles During the Last Glaciation

Monsoon variations on Dansgaard-Oeschger (D-O) time scales (~1.5 kyr) were reported from the carved sediment sections off Pakistan (Schulz et al. 1998), from bioturbated high-resolution sediment sections in the Arabian Sea (Sirocko et al. 1996), Bengal Fan (Kudrass et al. 2001), the SCS (Wang L. et al. 1999a; Bühring et al. 2001; Higginson et al. 2003; Zhao et al. 2006), the Sulu Sea (Oppo et al. 2001; de Garidel-Thoron et al. 2001), and the Sea of Japan (Tada et al. 1999). Wang L. et al. (1999a) were the first to report glacial millennial-scale D-O events from the SCS (Fig. 5.54). IMAGES Core MD972151 (Zhao et al. 2006) also offers an opportunity to correlate millennial- to centennial-scale SST variabilities in the SCS during the glacial period with the monsoon record from the Hulu Cave of eastern China (Wang Y. et al. 2001) and the D-O cycles in the GISP2 ice core record (Fig. 5.7). These results support that the glacial millennial-scale D-O events recorded in the SCS and on Chinese mainland are nearly synchronous with those found in Greenland ice cores, suggesting global climatic tele-connections.

As discussed earlier in this chapter, the SST difference between the southern and northern SCS can be used to monitor the strength of the East Asian winter monsoon, as illustrated in Fig. 5.55 with Mg/Ca-derived SST data from core 17961 and ODP Site 1145 (Oppo and Sun 2005). The S-N SST difference displays clear millennial-scale fluctuations at a period of ~1.4 kyr (Figs. 5.13 and 5.14). During interstadials of the D-O events, the S-N SST difference decreased correspondingly, indicating the decreased winter monsoon, and vice versa during stadials (Fig. 5.55). The overriding features of glacial D-O cycles correspond to increased summer monsoons during interstadials and increased winter monsoons during stadials, consistent with the exceptionally well-dated monsoon records of the Hulu Cave (Wang Y. et al. 2001) as well as with loess records from central China (An 2000).

Millennial-To-Centennial-Scale Cycles in the Holocene

Sub-orbital climate fluctuations also occurred in the Holocene, although the D/O-type variability of the last glaciation is no longer dominant (Schulz et al. 1999). Instead, the Holocene interval is characterized by variability with a broad range of periodicities near 890–950 yr, 550 yr, 200 yr, 145 yr, 80–105 yr, 20–24 yr and 11 yr (Wang P. et al. 2005). These scales of variability may be linked to changes in solar activity, which produce very weak variations in incident solar energy (Labitzke 2001; Beer et al. 2000; Haigh 1996).

In the northern SCS, fluctuations in the SSS during the Holocene reflect centennial periods of 775 yr and 102/84 yr which exceed the upper limit of red noise at 80% confidence level (Fig. 5.56). These periods lie far below the established range of Milankovitch orbital forcing, and also differ from the millennial-scale glacial D-O cycles (Wang L. et al. 1999a). Instead, the 102/84-year periodicities possibly reflect the Gleissberg cycle of solar activity.

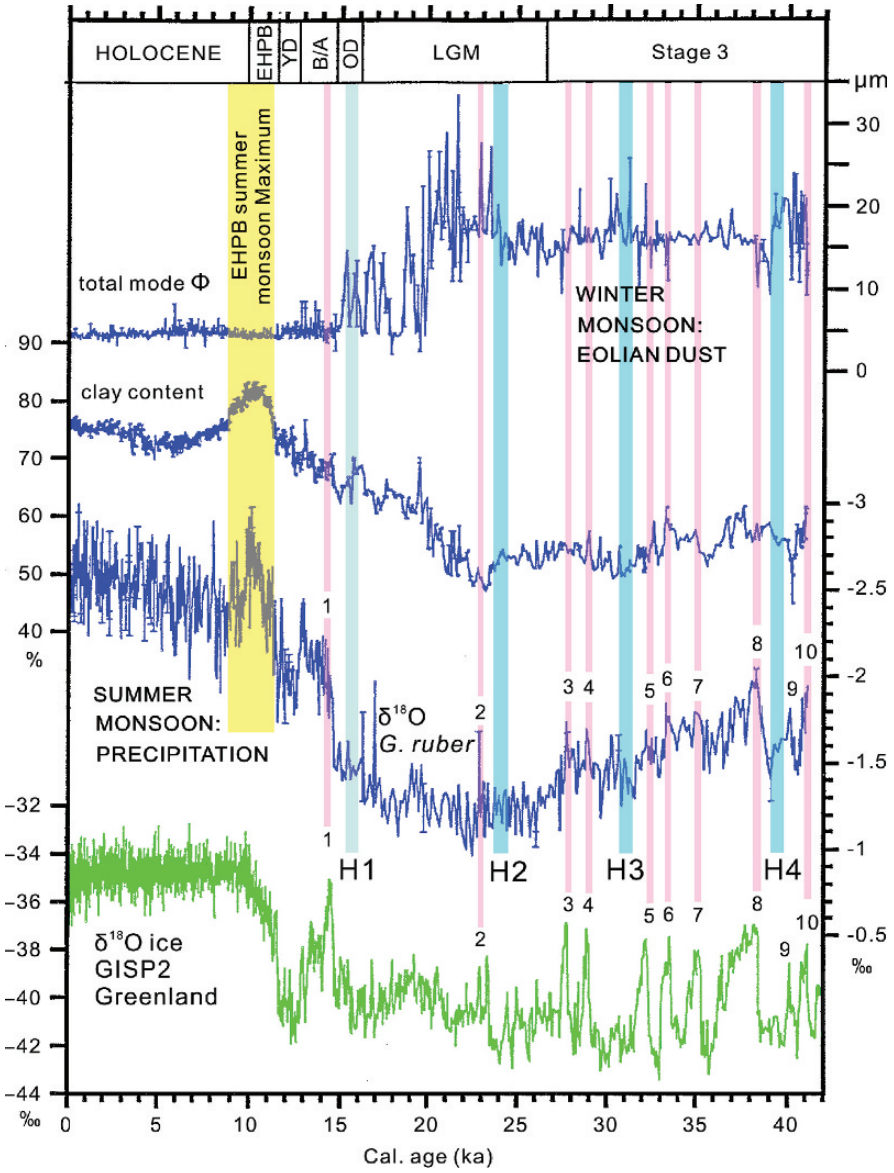

Fig. 5.54 Dansgaard-Oeschger (D-O in numbers) events and Heinrich events (H1 to H4) are recorded in core 17940-2 from the northern SCS (modified from Wang L. et al. 1999a). OD = Oldest Dryas; B/A = Bølling-Allerød; YD = Younger Dryas; EHPB = early Holocene/Preboreal

These new marine records can now be compared with a set of ultrahigh-resolution companion records from terrestrial archives, as obtained from East African and Tibetan lake sediments (Gasse et al. 1996), and Chinese speleothems (Wang Y. et al. 2001; Yuan et al. 2004). Among the millennial-scale climate records generated to

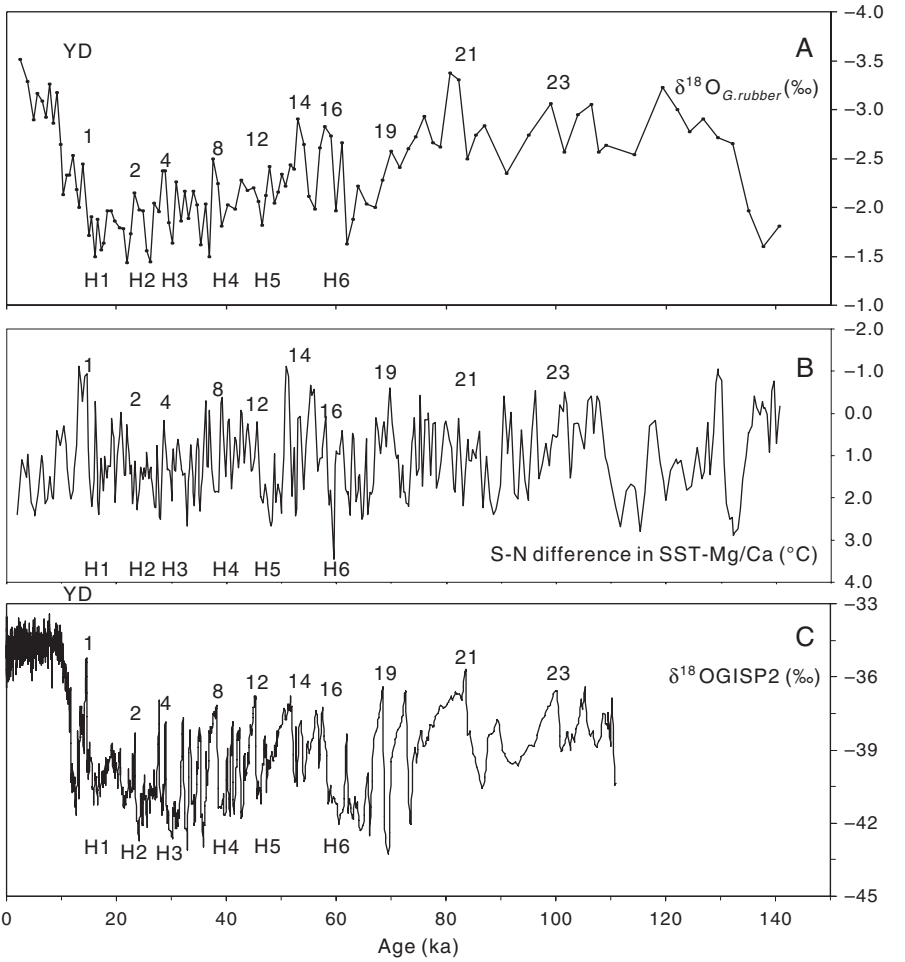

Fig. 5.55 Last glacial climate records from various regions show similar Dansgaard-Oeschger (D-O) events and Heinrich events (H1 to H6): (**A**) core 17961-2, southern SCS; (**B**) SST difference between core 17961 (Jian et al. 2008) from the southern and Site 1145 from northern SCS (Oppo and Sun 2005); (**C**) Greenland ice core $\delta^{18}O$ (Stuiver and Grootes 2000)

date, those from monsoonal regions show extremely strong similarities to those from the Greenland ice cores, indicating the coupled nature of high- and low-latitude abrupt climate change (Figs. 5.55 and 5.56). Despite their nature and mechanism are still vigorously being debated, factors such as tropical forcing and solar activity other than the glacial/interglacial ice cover volume change are most likely responsible for the sub-orbital climate changes. More high quality sediment sequences with high sedimentation rates in the SCS are needed for evaluating the phase relationships of climate signals in the monsoon region as compared to high-latitude climate components. This information will enhance our understanding of the role that monsoon circulation plays in sub-orbital variability.

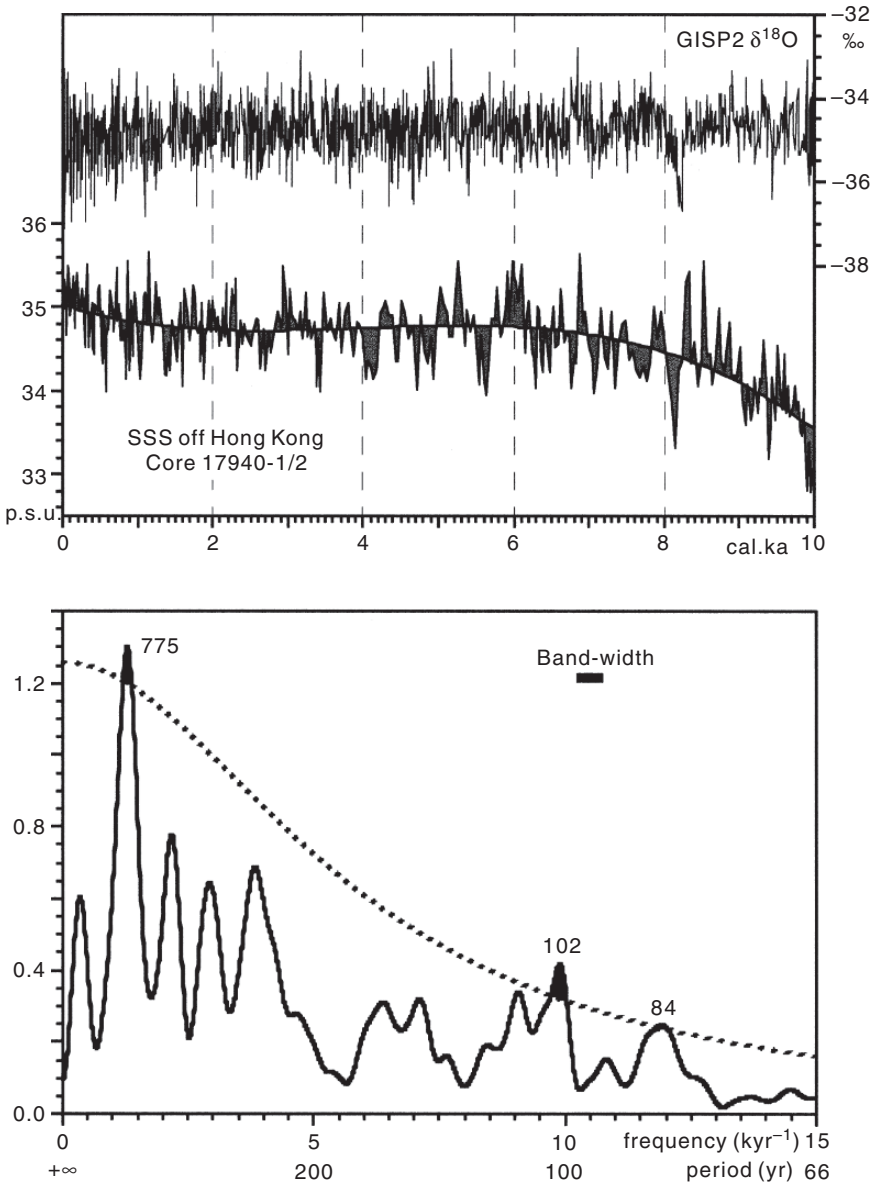

Fig. 5.56 Comparison between the δ^{18}O-based Holocene temperature record in Greenland ice-core GISP2 (Grootes and Stuiver 1997) and sea-surface salinity (SSS) changes in core 17940 off Hong Kong shows sub-orbital variations over the last 10,000 yr (from Wang L. et al. 1999a). Data are presented in the time (*upper panel*) and frequency domain (*lower panel* for SSS). Major temperature lows (δ^{18}O minima) on Greenland summit were coeval with SSS maxima, equal to lows and subsequent highs in monsoon precipitation in subtropical South China. *Horizontal bar* shows band-width. Numbers in the SSS power spectrum are significant periods in years, which exceed the *upper limit* of red noise at 80% confidence level (*dotted line*)

Summary

As the largest of the East Asian monsoon-dominated marginal seas between the largest continent Asia and the largest ocean Pacific, the SCS has witnessed dramatic changes in paleo-sea surface temperature, thermocline depth and paleo-vegetation of the surrounding continents/islands on tectonic, orbital and sub-orbital time scales in the late Cenozoic, which are summarized as follows:

1. *Upper water structure variations*. The upper water structure in the SCS is sensitive to changes in the East Asian monsoon and global ice-volume in the late Cenozoic. The foraminiferal assemblage data reveal that the depth of thermocline (DOT) in the SCS has experienced major changes at 11.5–10.6, 4.2–3.2 and 0.9 Ma, possibly related to the evolution of the WPWP. The Mg/Ca ratio derived SST in the southern SCS had ever decreased by ~5 °C during the formation of the Northern Hemisphere Glaciation. Since then, due to the strengthening of the winter monsoon and reorganization of sea circulation, the estimated SST decreased and the DOT deepened during glacials, and vice versa during interglacials. As shown by the paleo-SST estimations based on the transfer function technique, the average SST in the SCS was 0.9 °C cooler than in the Pacific at similar latitudes in summer, while the difference was as much as 4.9 °C in winter, resulting in an enhanced seasonality in the marginal seas, especially during glacials. The increased glacial/interglacial SST contrast in the marginal seas has been supported by $U^{K'}_{37}$ and Mg/Ca ratio analyses, showing the "amplifying effect" of climate changes in the SCS.
2. *East Asian monsoon evolution and variability*. A multi-proxy method for monsoon study in the SCS is recommended. The monsoon system started in the latest Oligocene and experienced major stages of intensification at ~8.0, 3.2, and 2.0 Ma, in accordance with the terrestrial records from the Loess Plateau. The evolution of East Asian monsoon was similar to the South Asian monsoon in stages, with an enhancement of the winter monsoon in East Asia being the major difference. On the orbital time scale, previous studies on Indian monsoonal upwelling have revealed that the Indian monsoon was externally forced by cyclical changes in solar insolation associated only with the obliquity and precession parameters. However, the SCS-based studies have shown that direct local insolation forcing could be less important in driving the East Asian winter monsoon variability, but the ice volume forcing may be the primary factor in determining their strength and timing. Therefore, intensified winter monsoon and weakened summer monsoon is typical of glacial periods, and vice versa for interglacial periods. The rich spectra of monsoon variability from the southern SCS exhibit characteristic features of orbital forcing in the low latitude ocean ranging from the 400 kyr eccentricity to 10 kyr semi-precessional cycles. The high-resolution Quaternary records have demonstrated that the D/O-like millennial-scale climate fluctuations exist throughout the last 1.0 myr and the rapid climatic events in the SCS were coeval with those found in Greenland ice cores, suggesting global climatic tele-connections.

3. *Land-Sea comparison*. The sediment records (e.g., marine pollen and clay mineral records) provide important information for the land-sea comparison of paleoclimatological changes in the SCS. The increase of cool-tolerant pollen group probably indicates climate cooling since ~8.0 and 2.6 Ma, consistent with the Chinese loess sequences. During the LGM, grassland vegetation mainly composed of *Artemisia* covered the exposed northern continental shelf of the SCS, indicating colder and drier climate relative to the present day. The glacial emergence of the continental shelf and SST decrease in SCS led to a considerable reduction of evaporation, involving a strongly enhanced continental aridity in the subtropical South China. Moreover, the evidence of pollen assemblages indicates cool but humid climate in the southern SCS during glacials. Since the southern SCS is a part of the WPWP, its exposure and cooling must have weakened the role of the warm pool in regional climate during glacial periods.
4. *South-North contrast*. The northern part of the SCS basin is controlled by the monsoon-driven cyclonic gyre, while the southern part belongs to the WPWP with much less monsoon influence. In the past, this S-N contrast became intensified with the growth of the Boreal ice sheet and the strengthening of the winter monsoon. Enhanced also by geological contrast between the landward sides to the NW (continent) and the SE (island arc), the southern and northern SCS are also different in many sedimentological and paleoceanographic aspects, including the different responses of the two parts to glacial cycles in micropaleontology, SST, and monsoon-induced upwelling. Palynological analyses have found grassland on the northern continental shelf, but forest on the southern shelf of the glacial SCS, indicating their different vegetational and climatic response to the LGM. Interestingly, the spectral analysis of the S-N SST difference (ΔSST) in the SCS has revealed precessional cycle and millennial variability, reflecting the changes in the East Asian monsoon on orbital and sub-orbital time scales.

Acknowledgments This work was supported by the Ministry of Science and Technology of China (NKBRSF Grant 2007CB815900), the National Natural Science Foundation of China (Grants 40621063, 40331002, 40476027 and 40776028) and the Ministry of Education of China (FANEDD Grant No. 2005036 to Tian).

References

An Z. 2000. The history and variability of the East Asian paleomonsoon climate. Quat. Sci. Rev. 19: 171–187.

An Z., Kutzbach J.E., Prell W.L. and Porter S.C. 2001. Evolution of Asian monsoons and phased uplift of the Himalaya-Tibetan Plateau since late Miocene time. Nature 411: 62–66.

Anand P., Elderfield H. and Conte M.H. 2003. Calibration of Mg/Ca thermometry in planktonic foraminifera from a sediment trap time series. Paleoceanography 18: 1050, doi:10.1029/2002PA000846.

Anderson C. 1997. Thansfer function vs. modern analog technique for estimating Pliocene sea-surface temperature based on planktonic foraminiferal data, west equatorial Pacific Ocean. J. Foraminiferal Res. 27: 123–132.

Anderson D. and Webb R.S. 1994. Ice-age tropics revisited. Nature 367: 23–24.

Anderson D.M., Overpeck J.T. and Gupta A.K. 2002. Increase in the Asian Southwest monsoon during the past four centuries. Science 297: 596–599.

Andreasen D.J. and Ravelo A.C. 1997. Tropical Pacific Ocean thermocline depth reconstructions for the last glacial maximum. Paleoceanography 12: 395–413.

Andree M., Oeschger H., Broecker W.S., Beavan N., Mix A., Bonani G., Hofmann H.J., Morenzoni E., Nessi M., Suter M. and Wolfli W. 1986. AMS radiocarbon dates on foraminifera from deep sea sediments. Radiocarbon 28(2A): 424–428.

Bé A.W.H. 1977. An ecological, zoogeographical and taxonomic review of recent planktonic foraminifera. In: Ramsay A.T.S. (ed.), Oceanic Micropaleontology. Academic Press, London, 1, pp. 1–100.

Bé A.W.H., Bishop J.K.B., Swerdlove M.S. and Gardner W.D. 1985. Standing stock, vertical distribution and flux of planktonic foraminifera in the Panama Basin. Mar. Micropaleontol. 9: 307–333.

Beer J., Mende W. and Stellmacher R. 2000. The role of the sun in climate forcing. Quat. Sci. Rev. 19: 403–415.

Bemis B., Spero H., Bijma J. and Lea D. 1998. Reevaluation of the oxygen isotopic composition of planktonic foraminifera: Experimental results and revised paleotemperature equations. Paleoceanography 13: 150–160.

Bentaleb I., Fontugne M. and Beaufort L. 2002. Long-chain alkenones and $U_{37}^{K'}$ variability along a south-north transect in the Western Pacific Ocean. Global Planet. Change 34: 173–183.

Berger A., Loutre M.F. and Laskar J. 1992. Stability of the astronomical frequencies over the Earth's history for paleoclimate studies. Science 255: 560–566.

Berggren W.A., Kent D.V., Swisher III C.C. and Aubry M.P. 1995. A revised Cenozoic geochronology and chronostratigraphy. In: Berggren W.A., Kent D.V., Aubry M.P. and Hardenbol J. (eds.), Geochronology, Time Scales and Global Stratigraphic Correlation. SEPM Spec. Publ. 54: 129–212.

Billups K., Ravelo A.C., Zachos J.C. and Norris R.D. 1999. Link between oceanic heat transport, thermohaline circulation, and the intertropical convergence zone in the early Pliocene Atlantic. Geology 27: 319–322.

Bond G., Broecker W., Johnsen S., McManus J., Labeyrie L., Jouzel J. and Bonani G. 1993. Correlations between climate records from North Atlantic sediments and Greenland ice. Nature 365: 143–147.

Bond G., Kromer B., Beer J., Muscheler R., Evans M.N., Showers W., Hoffmann S., Lotti-Bond R., Hajdas I. and Bonani G. 2001. Persistent solar influence on North Atlantic climate during the Holocene. Science 294: 2130–2136.

Broecker W.S., Andree M., Klas M., Bonani G., Wolfli W. and Oeschger H. 1988. New evidence from the South China Sea for an abrupt termination of the last glacial period. Nature 333: 156–158.

Bühring C., Sarnthein M. and Erlenkeuser H. 2001. Toward a high-resolution stable isotope stratigraphy of the last 1.1 million years: Site 1144, South China Sea. In: Prell W.L., Wang P., Blum P., Rea D. and Clemens S. (eds.), Proc. ODP Sci. Res. 184.

Cannariato K.G. and Ravelo A.C. 1997. Pliocene-Pleistocene evolution of eastern tropical Pacific surface water circulation and thermocline depth. Paleoceanography 12: 805–820.

Chaisson W.P. 1995. Planktonic foraminiferal assemblages and paleoceanographic change in the trans-tropical Pacific ocean: a comparison of West (Leg 130) and East (leg 138), latest Miocene to Pleistocene. In: Pisias N.G., Mayer L.A., Jenecek T.R., Palmer-Julson A. and van Andel T.H. (eds.), Proc. ODP Sci. Res. 138: 555–583.

Chao S.V., Shaw P.T. and Wu S.Y. 1996. Deep water ventilation in the South China Sea. Deep-Sea Res. II 43: 445–466.

Chapman M.R., Shackleton N. and Duplessy J.C. 2000. Sea surface temperature variability during the last glacial–interglacial cycles: assessing the magnitude and pattern of climate changes in the North Atlantic. Palaeogeogr. Palaeoclimatol. Palaeoecol. 157: 1–25.

Chen M.T., Huang C.C., Pflaumann U., Waelbroeck C. and Kucera M. 2005. Estimating glacial western Pacific sea-surface temprature: methodological overview and data compilation of surface sediment planktonic foraminifer faunas. Quat. Sci. Rev. 24: 1049–1062.

Chen M., Wang R., Yang L., Han J. and Lu J. 2003. Development of east Asian summer monsoon environments in the late Miocene: radiolarian evidence from Site 1143 of ODP Leg 184. Mar. Geol. 201: 169–177.

Chen R., Jian Z., Zheng Y. and Chen J. 2000. Seasonal variations of the planktonic foraminiferal flux in the central South China Sea. J. Tongji Univ. (Natural Sci.) 28(1): 73–77 (in Chinese).

Cheng H., Edwards R.L., Wang Y.J., Kong X., Ming Y., Gallup C.D., Kelly M.J., Wang X. and Liu W. 2006. A penultimate glacial monsoon record from Hulu Cave and two-phase glacial terminations. Geology 34: 217–220.

Cheng X., Huang B., Jian Z., Zhao Q., Tian J. and Li J. 2005. Foraminiferal isotopic evidence for monsoonal activity in the South China Sea: a present-LGM comparison. Mar. Micropaleontol. 54: 125–139.

Clemens S.C., Murray D.W. and Prell W.L. 1996. Nonstationary phase of the Plio-Pleistocene Asian monsoon. Science 274: 943–948.

Clemens S.C. and Prell W. 2003. A 350,000 year summer-monsoon multi-proxy stack from the Owen Ridge, Northern Arabian Sea. Mar. Geol. 201: 35–51.

Clemens S.C., Prell W., Murray D., Shimmield G. and Weedon G. 1991. Forcing mechanisms of the Indian Ocean monsoon. Nature 353: 720–725.

CLIMAP. 1981. Seasonal Reconstructions of the Earth's Surface at the Last Glacial Maximum. GSA Map. Chart Ser. MC-36.

Cullen J.L. and Prell W.L. 1984. Planktonic Foraminifera of the northern Indian Ocean: Distribution and preservation in surface sediments. Mar. Micropaleontol. 9: 1–52.

Curry W.B., Ostermann D.R., Guptha M.V.S. and Ittekkot V. 1992. Foraminiferal production and monsoonal upwelling in the Arabian Sea: Evidence from sediment traps. In: Summerhays C.P., Prell W.L. and Emeis K.C. (eds.), Upwelling Systems: Evolution Since the Early Miocene. Geological Society of London, Special Publication 63, pp. 93–106.

Dansgaard W., Johnsen S.J., Clausen H.B., Dahl-Jensen D., Gundestrup N.S., Hammer C.U., Hvidberg C.S., Steffensen J.P., Sveinbjornsdottir A.E., Jouzel J. and Bond G. 1993. Evidence for general instability of past climate form a 250-kyr ice-core record. Nature 364: 218–220.

de Garidel-Thoron T., Beaufort L., Linsley B.K. and Dannenmann S. 2001. Millennial-scale dynamics of the East-Asian winter monsoon during the last 200,000 years. Paleoceanography 16: 491–502.

Dekens P.S., Lea D.W., Park D.K. and Spero H.J. 2002. Core top calibration of Mg/Ca in tropical foraminifera: Refining paleotemperature estimation. Geochem. Geophys. Geosyst. 3: 10.1029/2001GC000200.

Dickens G.R. and Barron J.A. 1997. A rapid deposited pennate diatom ooze in upper Miocene-lower Pliocene sediment beneath the North Pacific polar front. Mar. Micropaleontol. 31: 177–182.

Ding Y., Li C. and Liu Y. 2004. Overview of the South China Sea Monsoon Experiment. Adv. Atmospheric Sci. 21: 343–360.

Ding Z.L., Rutter N.W., Han J.T. and Liu T.S. 1992. A coupled environmental system formed at about 2.5 Ma over East Asia. Palaeogeogr. Palaeoclimatol. Palaeoecol. 94: 223–242.

Ding Z.L., Sun J. and Liu D. 1999. Stepwise advance of the Mu Us Desert since Pliocene: Evidence of a red clay-loess record. Chinese Sci. Bull. 44(13): 1211–1214.

Ding Z.L., Sun J.M., Yang S.L. and Liu T.S. 1998. Preliminary magnetostratigraphy of a thick eolian red clay-loess sequence at Lingtai, the Chinese Loess Plateau. Geophys. Res. Lett. 25: 1225–1228.

Ding Z.L., Yu Z.W., Rutter N.W. and Liu T.S. 1994. Towards an orbital time scale for Chinese loess deposits. Quat. Sci. Rev. 13: 39–70.

Ducrocq S., Chaimanee Y., Suteethorn V. and Jaeger J.J. 1994. Ages and paleoenvironment of Miocene mammalian faunas from Thailand. Palaeogeogr. Palaeoclimatol. Palaeoecol. 108: 149–163.

Elderfield H. and Ganssen G. 2000. Past temperature and $\delta^{18}O$ of surface ocean waters inferred from foraminiferal Mg/Ca ratios. Nature 405: 442–445.

Ellison J.C. 1993. Mangrove retreat with rising sea level, Bermuda. Estuar. Coast. Shelf Sci. 37: 75–88.

Fairbanks R.G., Sverdlove M., Free R., Wiebe P.H. and Bé A.W.H. 1982. Vertical distribution and isotopic fractionation of living planktonic foraminifera from the Panama Basin. Nature 298: 841–844.

Fairbridge R.W. 1986. Monsoons and paleomonsoons. Episodes 9: 143–149.

Fang D., Jian Z. and Wang P. 2000. The paleoproductivity recorded in the southern Nansha sea area for about 30 ka. Chinese Sci. Bull. 45: 227–230.

Gao Q. and Zhang Q. 1981. Bryophytes of Northeast China. China Sci. Press, Beijing (in Chinese).

Gasse F., Fontes J.Ch., Van Campo E. and Wei K. 1996. Holocene environmental changes in Bangong Co basin (Western Tibet). Part 4: Discussion and conclusions. Palaeogeogr. Palaeoclimatol. Palaeoecol. 120: 79–92.

Grindrod J. and Rhodes E.G. 1984. Holocene sea-level history of a tropical estuary: Missionary Bay, North Queensland. In: Thom B.G. (ed.), Coastal Geomorphology in Australia. Academic Press, Sydney, pp. 151–178.

Grootes P.M. and Stuiver M. 1997. Oxygen 18/16 variability in Greenland snow and ice with 10^{-3}-to 10^{-5}-year time resolution. J. Geophys. Res. C102: 26455–26470.

Guangdong Institute of Botany 1976. Vegetation of Guangdong. China Sci. Press, Beijing (in Chinese).

Guo Z.T., Ruddiman W.F., Hao Q.Z., Wu H.B., Qiao Y.S., Zhu R.X., Peng S.Z., Wei J.J., Yuan B.Y. and Liu T.S. 2002. Onset of Asian desertification by 22 Myr ago inferred from loess deposits in China. Nature 416: 159–163.

Haigh J.D. 1996. The impact of solar variability on climate. Science 272: 981–984.

Hanebuth T., Stattegger K. and Groote P.M. 2000. Rapid flooding of the Sunda Shelf: a late-glacial sea-level record. Science 288: 1033–1035.

Hastings D., Kienast M., Steinke S. and Whitko A.A. 2001. A Comparison of three independent paleotemperature estimates from a high resolution record of deglacial SST records in the tropical South China Sea. EOS Trans. AGU 82: PP12B-10.

Hastings D., Russell A.D. and Emerson S.R. 1998. Foraminiferal magnesium in *Globigerinoides sacculifer* as a paleotemperature proxy. Paleoceanography 13: 161–169.

Hemleben C., Spindler M. and Anderson O.R. 1989. Modern Planktonic Foraminifera. Springer-Verlag, New York, 363pp.

Higginson M., Maxwell J.R. and Altabet M.A. 2003. Nitrogen isotope and chlorin paleoproductivity records from the Northern South China Sea: remote vs. local forcing of millennial- and orbital-scale variability. Mar. Geol. 201: 223–250.

Hirst A.C. and Godfrey J.S. 1993. The role of Indonesian throughflow in a global ocean GCM. J. Phys. Oceanogr. 23: 1057–1086.

Hope G.S. and Tulip J. 1994. A long vegetation history from lowland Iran Jaya, Indonesia. Paleogeogr. Paleoclimatol. Paleoecol. 109: 385–398.

Hostetler S., Pisias N. and Mix A. 2006. Sensitivity of Last Glacial Maximum climate to uncertainties in tropical and subtropical ocean temperatures. Quat. Sci. Rev. 25: 1168–1185.

Hovan S.A., Rea D.K., Pisias N.G. and Shackleton N.J. 1989. A direct link between the China loess and marine $\delta^{18}O$ records: Aeolian flux to the north Pacific. Nature 340: 296–298.

Hu J., Peng P., Fan D., Jia G., Jian Z. and Wang P. 2003. No aridity in Sunda land during the Last Glaciation: Evidence from molecular-isotopic stratigraphy of long-chain *n*-alkans. Palaeogeogr. Palaeoclinatol. Palaeoecol. 201: 269–281.

Hu J., Peng P., Jia G., Fang D., Fu J. and Wang P. 2002. Biological markers and their carbon isotopes as an approach to the paleoenvironmental reconstruction of Nansha area, South China Sea, during the last 30 ka. Org. Geochem. 33: 1197–1204.

Huang B., Cheng X., Jian Z. and Wang P. 2003. Response of upper ocean structure to the initiation of the North Hemisphere glaciation in the South China Sea. Palaeogeogr. Palaeoclimatol. Palaeoecol. 196: 305–318.

Huang B., Jian Z., Cheng X. and Wang P. 2002. Foraminiferal responses to upwelling variations in the South China Sea over the last 220 000 years. Mar. Micropaleontol. 47: 1–15.

Huang C.Y., Liew P.M., Zhao M., Chang T.C., Kuo C.M., Chen M. T., Wang C.H. and Zheng L.F. 1997a. Deep sea and lake records of the Southeast Asian paleomonsoons for the last 25 thousand years. Earth Planet. Sci. Lett. 146: 59–72.

Huang C.Y., Wu S.F., Zhao M., Chen M.T., Wang C.H., Tu X. and Yuan P.B. 1997b. Surface ocean and monsoon climate variability in the South China Sea since the last glaciation. Mar. Micropaleotol. 32: 71–94.

Hutson W.H. 1980. The Agulhas Current during the Late Pleistocene: Analysis of modern faunal analogs. Science 207: 64–66.

Imbrie J., Boyle E., Clemens S., Duffy A., Howard W.R., Kukla G., Kutzbach J., Martinson D.G., McIntyre A., Mix A.C., Molfino B., Morley J.J., Peterson L.C., Pisias N.G., Prell W.L., Raymo M.E., Shackleton N.J. and Toggweiler J.R. 1992. On the structure and origin of major glaciation cycles, 1, Linear responses to Milankovitch forcing. Paleoceanography 7: 701–738.

Imbrie J. and Kipp N.G. 1971. A new micropaleontological method for quantitative paleoclimatology: Application to a late Pleistocene Carinbbean core. In: Turekian K.K. (ed.), The Late Cenozoic Glacial Ages. Yale Univ. Press, New Haven, Conn., pp. 71–181.

Jia G., Peng P., Zhao Q. and Jian Z. 2003. Changes in terrestrial ecosystem since 30 Ma in East Asia: Stable isotope evidence from black carbon in the South China Sea. Geology 31: 1093–1096.

Jian Z. and Huang W. 2003. Rapid climate change and high resolution deep-sea sedimentary records. Adv. Earth Sci. 18(5): 673–680 (in Chinese).

Jian Z., Huang B., Lin H. and Kuhnt W. 2001. Late Quaternary upwelling intensity and East Asian monsoon forcing in the South China Sea. Quat. Res. 55: 363–370.

Jian Z., Li B., Huang B. and Wang J. 2000a. *Globorotalia truncatulinoides* as indicator of upper-ocean thermal structure during the Quaternary: Evidences from the South China Sea and Okinawa Trough. Palaeogeogr. Palaeoclimatol. Palaeoecol. 162: 287–298.

Jian Z., Wang B. and Qiao P. 2008. Late Quaternary changes of sea surface temperature in the southern South China Sea and their comparison with the paleoclimatic records of polar ice cores. Quat. Sci. 3: 391–398 (in Chinese).

Jian Z. and Wang L. 1997. Late Quaternary benthic foraminifera and deep-water paleoceanography in the South China Sea. Mar. Micropaleotol. 32: 127–154.

Jian Z., Wang L., Kienast M., Sarnthein M., Kuhnt W., Lin H. and Wang P. 1999. Benthic foraminiferal paleoceanography of the South China Sea over the last 40,000 years. Mar. Geol. 156: 159–186.

Jian Z., Wang P., Chen M.P., Li B., Zhao Q., Bühring C., Laj C., Lin H.L., Pflaumann U., Bian Y., Wang R. and Cheng X. 2000b. Foraminiferal response to major Pleistocene paleographic changes in the southern South China Sea. Paleoceanography 15: 229–243.

Jian Z., Yu Y., Li B., Wang J., Zhang X. and Zhou Z. 2006. Phased evolution of the south-north hydrographic gradient in the South China Sea since the middle Miocene. Palaeogeogr. Palaeoclimatol. Palaeoecol. 230: 251–263.

Jian Z., Zhao Q., Cheng X., Wang J., Wang P. and Su X. 2003. Pliocene-Pleistocene stable isotope and paleoceanographic changes in the northern South China Sea. Palaeogeogr. Palaeoclimatol. Palaeoecol. 193: 425–442.

Kennett J.P., Keller G. and Srinivasan M.S. 1985. Miocene planktonic foraminiferal biogeography and paleoceanographic de velopment of the Indo-Pacific region, in The Miocene Ocean: Paleogeography and Biogeography. GSA Memoir 163: 197–236.

Kienast M., Hanebuth T.J.J., Pelejero C. and Steinke S. 2003. Synchroneity of meltwater pulse 1a and the Bølling warming: new evidence from the South China Sea. Geology 31: 67–70.

Kienast M., Steinke S., Stattegger K. and Calvert S.E. 2001. Synchronous tropical South China Sea SST change and Greenland warming during deglaciation. Science 291: 2132–2134.

Kienast S.S., Calvert S.E. and Pedersen T.F. 2002. Nitrogen isotope and productivity variations along the northeast Pacific margin over the last 120 kyr: Surface and subsurface paleoceanography. Paleoceanography 17: 1055, doi: 10.1029/2001PA000650.

Kissel C., Laj C., Clemens S. and Solheid P. 2003. Magnetic signature of environmental changes in the last 1.2 Myr at ODP Site 1146, South China Sea. Mar. Geol. 201: 119–132.

Kroon D., Steens T.N.F. and Troelstra S.R 1991. Onset of monsoonal related upwelling in the western Arabian Sea. Proc. ODP Sci. Results 117: 257–264.

Kudrass H.R., Hofmann A., Doose H., Emeis K. and Erlenkeuser H. 2001. Modulation and amplification of climatic changes in the Northern Hemisphere by the Indian summer monsoon during the past 80 k.y. Geology 29: 63–66.

Kuhnt W., Hess S. and Jian Z. 1999. Quantitative composition of benthic foraminiferal assemblages as a proxy indicator for organic carbon flux rates in the South China Sea. Mar. Geol. 156: 123–157.

Kuroyanagi A. and Kawahata H. 2004. Vertical distribution of living planktonic foraminifera in the seas around Japan. Mar. Micropaleontol. 53: 173–196.

Kutzbach J.E. and Guetter P.J. 1986. The influence of changing orbital parameters and surface boundary conditions on climate simulations for the past 18000 years. J. Atmos. Sci. 43: 1726–1759.

Labitzke K. 2001. The global signal of the 11-year sunspot cycle in the stratosphere: differences between solar maxima and minima. Meteorol. Z. 10: 901–908.

Lea D.W., Pak D.K. and Spero H.J. 2000. Climate impact of Late Quaternary equatorial Pacific sea surface temperature variation. Science 289: 1719–1724.

Levitus S. 1982. Climatological Atlas of the World Ocean. In: NOAA Professional Paper 13. Washington, D.C.: U.S. Government Printing Office.

Levitus S. and Boyer T.P. 1994. World Ocean Atlas, vol. 4: Temperature. In: NOAA Atlas NESDIS 4. U.S. Govt. Printing Office, Washington, D.C.

Li J. 1991. The environmental effects of the uplift of the Qinghai-Xizang Plateau. Quat. Sci. Rev. 10: 479–483.

Li J. and Fang S. 1996. Studies on the uplift and environmental changes of the Qinghai-Xizang Plateau. Chin. Sci. Bull. 41: 316–322.

Li B., Wang J., Huang B., Li Q., Jian Z. and Wang P. 2004. South China Sea surface water evolution over the last 12 Ma: A south-north comparison from ODP Sites 1143 and 1146. Paleoceanography 19: PA1009, doi:10.1029/2003PA000906.

Li J. and Wang R. 2004. Paleoproductivity variability of the northern South China Sea during the past 1 Ma: The opal record from ODP Site 1144. Acta Geol. Sinica 78(2): 228–233 (in Chinese).

Li J., Wang R. and Li B. 2002. Variations of opal accumulation rates and paleoproductivity over the past 12 Ma at ODP Site 1143, southern South China Sea. Chinese Sci. Bull. 47: 596–598.

Li Q., Li B., Zhong G., McGowran B., Zhou Z., Wang J. and Wang P. 2006. Late Miocene development of the western Pacific warm pool: Planktonic foraminifer and oxygen isotopic evidence. Palaeogeogr. Palaeoclimatol. Palaoeecol. 237: 465–482.

Li X. and Sun X. 1999. Palynological records since Last Glacial Maximum from a deep-sea core in the southern South China Sea. Quat. Sci. 4: 526–535 (in Chinese).

Lin H., Lai C., Ting H., Wang L., Sarnthein M. and Huang J. 1999. Late Pleistocene nutrients and sea surface productivity in the South China Sea: a record of teleconnections with northern hemisphere events. Mar. Geol. 156: 197–210.

Liu C., Cheng X., Zhu Y., Tian J. and Xia P. 2002. Oxygen and carbon isotopic records of calcareous nannofossils for the past 1 Ma in the southern South China Sea. Chinese Sci. Bull. 47(10): 798–803.

Liu Z., Trentesaux A., Clemens S.C., Colin C., Wang P., Huang B. and Boulay S. 2003. Clay mineral assemblages in the northern South China Sea: implications for East Asian monsoon evolution over the past 2 million years. Mar. Geol. 201: 133–146.

Lohmann G.P. and Schweitzer P.N. 1990. *Globorotalia truncatulinoides* growth and chemistry as probes of the past thermocline: 1. Shell size. Paleoceanography 5: 55–75.

Löwemark L., Hong W.L., Yui T.F. and Hung G.W. 2005. A test of different factors influencing the isotopic signal of planktonic foraminifers in surface sediments from the northern South China Sea. Mar. Micropaleontol. 55: 49–62.

Luo Y., Cheng H., Wu G. and Sun X. 2001. Records of natural fire and climate history during the last three glacial- interglacial cycles around the South China Sea - Charcoal record from the ODP 1144. Sci. China (D) 44(10): 897–904.

Luo Y. and Sun X. 2007. Deep-sea pollen in the southern South China Sea during 12 ~ 1.6Ma BP and its response to the global climate change. Chinese Sci. Bull. 52(15): 2115–2122.

Luo Y., Sun X. and Jian Z. 2005. Environmental change during the penultimate glacial cycle: a high-resolution pollen record from ODP Site 1144, South China Sea. Mar. Micropaleontol. 54: 107–123.

Ma Y., Fan X., Li J., Wu F. and Zhang J. 2004. Vegetational and environmental changes during late Tertiary- early Quaternary in Jiuxi Basin. Sci. China (D) 34: 107–116 (in Chinese).

Ma Y., Li J. and Fan X. 1998. Pollen- based vegetation and climate records during 30.6 to 5.0 My from Linxia area, Gansu. Chinese Sci. Bull. 43(3): 301–304 (in Chinese).

Maier-Reimer E., Mikolajewicz U. and Crowley T. 1990. Ocean general circulation model sensitivity experiment with an open central American isthmus. Paleoceanography 5: 349–266.

Mao S., Li J., Wu G. and Harland R. 2007. Dinoflagellate cycts and environmental evolution of the Oligocene to Lower Miocene at Site 1148, ODP Leg 184, South China Sea. Palynology 31: 37–52.

Martinez J.I. 1997. Decreasing influence of Subantarctic Mode Water north of the Tasman Front over the past 150 kyr. Palaeogeogr. Palaeoclimatol. Palaeoecol. 131: 355–364.

Martinez J.I. 1994. Late Pleistocene paleoceanography of the Tasman Sea: implications for the dynamics of the warm pool in the western Pacific. Palaeogeogr. Palaeoclimatol. Palaeoecol. 112: 19–62.

McManus J.F., Oppo D.W. and Cullen J.L. 1999. A 0.5 million year record of millennial-scale climate variability in the North Atlantic. Science 283: 971–975.

Miao Q., Thunell R.C. and Andersen D.M. 1994. Glacial-Holocene carbonate dissolution and sea surface temperatures in the South China and Sulu seas. Paleoceanography 9: 269–290.

Mudelsee M. and Raymo M.E. 2005. Slow dynamics of the Northern Hemisphere glaciations. Paleoceanography 20: PA4022, doi:10.1029/2005PA001153.

Newsome J.C. and Flenley J.R. 1988. Late Quaternary vegetation history of the Central Highland of Sumatra II. Palaeopalynology and vegetation history. J. Biogeogr. 15: 555–578.

NGRIP (North Greenland Ice Core Project) Members 2004. High-resolution record of Northern Hemisphere climate extending into the last interglacial period. Nature 431: 147–151.

Nürnberg D., Bijma J. and Hemleben C. 1996. Assessing the reliability of magnesium in foraminiferal calcite as a proxy for water mass temperature. Geochim. Cosmochim. Acta 60: 803–814.

Nürnberg D., Muller A. and Schneider R.R. 2000. Paleo-sea surface temperature calculations in the equatorial east Atlantic from Mg/Ca ratios in planktic foraminifera: a comparison to sea surface temperature estimates from $U^{K'}_{37}$, oxygen isotopes, and foraminiferal transfer function. Paleoceanography 15(1): 124–134.

Oppo D.W., Linsley B.K., Dannemann S. and Beaufort L. 2001. A 400-kyr long planktic $\delta^{18}O$ record from the Sulu Sea: constraints on ice volume and the tropical hydrologic cycle. EOS Trans. AGU 82(47): F737.

Oppo D.W. and Sun Y. 2005. Amplitude and timing of sea-surface temperature change in the northern South China Sea: Dynamic link to the East Asian monsoon. Geology 33: 785–788.

Pelejero C. and Calvo E. 2003. The upper end of the $U_{37}^{K'}$ temperature calibration revisited. Geochem. Geophys. Geosyst. 4: doi:10.1028/2002GC000431.

Pelejero C. and Grimalt J.O. 1997. The correlation between the $U_{37}^{K'}$ index and sea surface temperatures in the warm boundary: the South China Sea. Geochim. Cosmochim. Acta 61: 4789–4797.

Pelejero C., Grimalt J.O., Heilig S., Kienast M. and Wang L. 1999a. High-resolution $U_{37}^{K'}$ temperature reconstructions in the South China Sea over the past 220 kyr. Paleoceanography 14: 224–231.

Pelejero C., Grimalt J.O., Sarnthein M., Wang L. and Flores J.A. 1999b. Molecular biomarker record of sea surface temperature and climatic change in the South China Sea during the last 140,000 years. Mar. Geol. 156: 109–121.

Pflaumann U., Duprat J., Pujol C. and Labeyrie L.D. 1996. SIMMAX: a modern analog technique to deduce Atlantic sea surface temperatures from planktonic foraminifera in deep-sea sediments. Paleoceanography 11: 15–35.

Pflaumann U. and Jian Z. 1999. Modern distribution patterns of planktonic foraminifera in the South China Sea and western Pacific: A new transfer technique to estimate regional sea-surface temperatures. Mar. Geol. 156: 41–83.

Porter S.C., An Z. and Zheng H. 1992. Cyclic Quaternary alleviation and terracing in a nonglaciated Drainage Basin on the north flank of Qingling Shan, central China. Quat. Res. 38: 157–169.

Prahl F.G. and Wakeham S.G. 1987. Calibration of unsaaturation patterns in long-chain ketone composition for paleotemperature assessment. Nature 330: 367–369.

Prell W.L. 1984. Covariance pattern of foraminiferal $\delta^{18}O$: An evaluation of Pliocene ice volume change near 3.2 million years ago. Science 226: 692–693.

Prell W.L. and Kutzbach J.E. 1987. Monsoon variability over the past 150,000 years. J. Geophys. Res. 92: 8411–8425.

Prell W.L. and Kutzbach J.E. 1997. The impact of Tibetan-Himalayan elevation on the sensitivity of the monsoon climate system to changes in solar radiation. In: Ruddiman W.F. (ed.), Tectonic Uplift and Climate Change, Plenum Press, pp. 171–201.

Prell W.L., Murray D.W., Clemens S.C. and Anderson D.M. 1992. Evolution and variability of the Indian Ocean summer monsoon: Evidence from the western Arabian Sea drilling program. In: Duncan R.A., Rea D.K., Kidd R.B., von Rad U. and Weissel J.K. (eds.), The Indian Ocean: A Synthesis of Results from the Ocean Drilling Program. Geophys. Monogr. 70, AGU, pp. 447–469.

Qin G. 1996. Biostratigraphic zonation and correlation of the late Cenozoic planktonic foraminifera in Pearl River Basin. In: Hao Y. (ed.), Research on Micropalaeontology and Paleoceanography in Pearl River Mouth Basin, South China Sea. China Univ. Geosci. Press, Beijing, pp. 19–31 (in Chinese).

Quade J., Cerling T.E. and Bowman J.E. 1989. Development of Asian monsoon revealed by marked ecological shift during the latest Miocene in northern Pakistan. Nature 342: 163–166.

Qiang X.K., Li Z.X., Powell C. and Zheng H. 2001. Magnetostratigraphic record of the Late Miocene onset of the East Asian monsoon, and Pliocene uplift of northern Tibet. Earth Planet. Sci. Lett. 187: 83–93.

Ravelo A.C., Andreasen D.H., Lyle M., Olivarez Lyle A. and Wara M.W. 2004. Regional climate shifts caused by gradual cooling in the Pliocene epoch. Nature 429: 263–267.

Ravelo A.C., Fairbanks R.G. and Philander S.G.H. 1990. Reconstructing tropical Atlantic hydrography using planktonic foraminifera and an ocean model. Paleoceanography 5: 409–431.

Ravelo A.C. and Fairbanks R.G. 1992. Oxygen isotopic composition of multiple species of planktonic foraminifera: Recorders of the modern photic zone temperature gradient. Paleoceanography 7: 815–831.

Ravelo A. and Shackleton N.J. 1995. Evidence for surface-water circulation changes at Site 851 in the eastern tropical Pacific Ocean. Proc. ODP Sci. Res. 138: 503–514.

Raymo M.E., Ganley K., Carter S., Oppo D.W. and McManus J. 1998. Millennial-scale climate instability during the early Pleistocene epoch. Nature 392: 699–702.

Ramstein G., Fluteau F., Besse J. and Joussaume S. 1997. Effect of orogeny, plate motion and land-sea distribution on Eurasian climate change over the past 30 million years. Nature 386: 788–795.

Rea D.K. 1992. Delivery of Himalayan sediment to the northern Indian Ocean and its relation to global climate, sea level, uplift, and seawater strontium. In: Duncan R.A. (ed.), Synthesis of Results from Scientific Drilling in the Indian Ocean. Geophys. Monogr. Ser. 70: 387–402.

Rea D.K., Snoeck H. and Joseph L.H. 1998. Late Cenozoic eolian deposition in the North Pacific: Asian drying, Tibetan uplift, and cooling of the Northern Hemisphere. Paleoceanography 13: 215–224.

Rosenthal Y. and Lohmann G.P. 2002. Accurate estimation of sea surface temperatures using dissolution corrected calibrations for Mg/Ca paleothermometry. Paleoceanography 17: 10.1029/2001PA000749.

Rosenthal Y., Oppo D.W. and Linsley B.K. 2003. The amplitude and phasing of climate change during the last deglaciation in the Sulu Sea, western equatorial Pacific. Geophys. Res. Lett. 30(8): 1428, doi: 10.1029/2002GL016612.

Sarnthein M., Kennett J.P., Allen J.R.M., Beer J., Grootes P., Laj C., McManus J., Ramesh R. and SCOR-IMAGES Working Group 117. 2002. Decadal-to-millennial-scale climate variability - chronology and mechanisms: summary and recommendations. Quat. Sci. Rev. 21: 1121–1128.

Sarnthein M., Pflaumann U., Ross R., Tiedemann R. and Winn K. 1992. Transfer functions to reconstruct ocean paleoproductivity: a comparison. Geol. Soc. Spec. Public. 64:411–427.

Sarnthein M., Pflaumann U., Wang P. and Wong H.K. (eds.). 1994. Preliminary Report on SONNE-95 Cruise "Monitor Monsoon" to the South China Sea. Berichte-Reports, Geol.-Palaont. Inst. Univ. Kiel, 48, pp. 1–225.

Schmidt H., Berger W.H., Bickert T. and Wefer G. 1993. Quaternary carbon isotope record of pelagic foraminifers: Site 806, Ontong Java Plateau. Proc. ODP Sci. Res. 130: 397–409.

Schulz M., Berger W.H., Sarnthein M. and Grootes P. 1999. Amplitude variations of 1470-year climate oscillations during the last 100,00 years linked to fluctuations of continental ice mass. Geophys. Res. Lett. 26: 3385–3388.

Schulz M. and Paul A. 2002. Holocene climate variability on centennial-to- millennial time scales: 1. Climate records from the North-Atlantic realm. In: Wefer G., Berger W.H., Behre K.E. and Jansen E. (eds.), Climate Development and History of the North Atlantic Realm, Springer Verlag, Berlin, pp. 41–54.

Schulz H., von Rad U. and Erlenkeuser H. 1998. Correlation between Arabian Sea and Greenland climate oscillations of the past 110,000 years. Nature 393: 54–57.

Shaw P.T. 1996. Winter upwelling off Luzon in the Northeastern South China Sea. J. Geophys. Res. 101: 16435–16448.

Sirocko F., Garbe-Schönberg C.D., McIntyre A. and Molfino B. 1996. Teleconnections between the subtropical monsoons and high-latitude climates during the last deglaciation. Nature 272: 526–529.

Stattegger K., Kuhnt W., Wong H.K. and Scientific Party 1997. Cruise Report SONNE 115 SUNDAFLUT. Berichte-Report 86, Institüt für Geowissenschaften, Univ. Kiel, 211pp.

Steinke S. and Chen M.T. 2003. The spatial distribution patterns of *Pulleniatina obliquiloculata* in the South China Sea: implications of latitudinal differences in the strength of the East Asian winter monsoon intensity during the last glaciations. EGS-AGU-EUG Joint Assembly, Scientific Program, 327.

Steinke S., Chiu H.Y, Yu P.S., Shen C.C., Erlenkeuser H., Löwemark L. and Chen M.T. 2006. On the influence of sea level and monsoon climate on the southern South China Sea freshwater budget over the last 22,000 years. Quat. Sci. Rev. 25: 1475–1488.

Steinke S., Chiu H.Y, Yu P.S., Shen C.C., Löwemark L., Mii H.S. and Chen M.T. 2005. Mg/Ca ratios of two *Globigerinoides ruber* (white) morphotypes: implications for reconstructing past tropical/subtropical surface water conditions. Geochem. Geophys. Geosyst. 6: doi:10.1029/2005GC000926.

Steinke S., Kienast M., Groeneveld J., Lin L.C., Chen M.T. and Rendle-Bühring R. 2008a. Proxy dependence of the tempral patten of deglacial warming in the tropical South China Sea: toward resolving seasonality. Quat. Sci. Rev. 27: 688–700.

Steinke S., Kienast M., Pflaumann U., Weinelt M. and Stattegger K. 2001. A high resolution sea-surface temperature record from the tropical South China Sea (16,500–3000 B.P.). Quat. Res. 5: 353–362.

Steinke S., Yu P.S., Kucera M. and Chen M.T. 2008b. No-analog planktonic foraminiferal faunas in the glacial southern South China Sea: Implications for the magnitude of glacial cooling in the western Pacific warm pool. Mar. Micrpaleontol. 66: 71–90.

Stott L., Poulsen C., Lund S. and Thunell R. 2002. Super ENSO and global climate oscillations at millennial time scales. Science 297: 222–226.

Stuijts I., Newsome J.C. and Flenley J.R. 1988. Evidence for late Quaternary vegetational change in the Sumatran and Javan Highlands. Rev. Palaeobot. Palynol. 55: 207–216.

Stuiver M. and Grootes P.M. 2000. GISP2 oxygen isotope ratios. Quat. Res. 53: 277–284.

Su G. and Wang T. 1994. Basic characteristics of modern sedimentation in the South China Sea. In: Zhou D., Liang Y.B. and Zheng C.K. (eds.), Oceanology of China Seas. Kluwer, New York, pp. 407–418.

Sun Y. and An Z. 2001. History and variability of aridification in Asian Interior as recorded in dust flux of the Loess Plateau over the last 7 ma. Sci. China (D) 31(9): 769–767 (in Chinese).

Sun D.H., Shaw J., An Z., Cheng M. and Yue L. 1998. Magnetostratigraphy and paleoclimatic interpretation of a continuous 7.2 Ma Late Cenozoic eolian sediments from the Chinese Loess Plateau. Geophys. Res. Lett. 25: 85–88.

Sun X. and Li X. 1999. A pollen record of the last 37 ka in deep sea core 17940 from the northern South China Sea. Mar. Geol. 156: 227–244.

Sun X., Li X. and Beug H.J. 1999. Pollen distribution in hemipelagic surface sediments of the South China Sea and its relation to modern vegetation distribution. Mar. Geol. 156: 211–226.

Sun X., Li X. and Chen H. 2000a. Evidence for natural fire and climate history since 37 ka BP in the northern part of the South China Sea. Sci. China (D) 43(5): 487–493.

Sun X., Li X., Luo Y. and Chen X. 2000b. The vegetation and climate at the last glaciation on the emerged continental shelf of the South China Sea. Palaeogeogr. Palaeoclimatol. Palaeoecol. 160: 301–316.

Sun X., Li X. and Luo Y. 2002. Vegetation and climate on the Sunda Shelf of the South China Sea during the Last Glactiation-Pollen results from station 17962. Acta Bot. Sinica 44(6): 746–752.

Sun X. and Luo Y. 2001. Pollen record of the last 280 ka from deep-sea sediments of the northern South China Sea. Sci. China (D) 44(10): 879–888.

Sun X., Luo Y., Huang F., Tian J. and Wang P. 2003. Deep-sea pollen from the South China Sea: Pleistocene indicators of East Asian monsoon. Mar. Geol. 201: 97–118.

Sun X. and Wang P. 2005. How old is the Asian monsoon system? – Palaeobotanical records from China. Palaeogeogr., Palaeoclimatol., Palaeoecol. 222: 181–222.

Svensson A., Andersen K.K., Bigler M., Clausen H.B., Dahl-Jensen D., Davies S.M., Johnsen S.J., Muscheler R., Parrenin F., Rasmussen S.O., Röthlisberger R., Seierstad I., Steffensen J.P. and Vinther B.M. 2008. A 60 000 year Greenland stratigraphic ice core chronology. Clim. Past 4: 47–57.

Tada R., Irino T. and Koizumi I. 1999. Land-ocean linkages over orbital and millennial timescales recorded in late Quaternary sediments of the Japan Sea. Paleoceanography 14: 236–247.

Thompson P.R. 1981. Planktonic foraminifer in the western North Pacific during the past 150,000 years: comparison of modern and fossil assemblages. Palaeogeogr. Palaeoclimatol. Palaeoecol. 35: 441–479.

Thunell R.C., Curry W.B. and Honjo S. 1983. Seasonal variation in flux of planktonic foraminifera time-series sediment trap results from the Panama Basin. Earth Planet. Sci. Lett. 64: 44–55.

Tian J., Pak D.K., Wang P., Lea D., Cheng X. and Zhao Q. 2006. Late Pliocene monsoon linkage in the tropical South China Sea. Earth Planet. Sci. Lett. 252: 72–81.

Tian J., Wang P. and Cheng X. 2004. Development of the East Asian monsoon and Northern Hemisphere glaciation: Oxygen isotope records from the South China Sea. Quat. Sci. Rev. 23: 2007–2016.

Tian J., Wang P., Cheng X., Wang R. and Sun X. 2005a. Forcing mechanism of the Pleistocene east Asian monsoon variations in a phase perspective. Sci. China (D) 48(10): 1708–1717.

Tian J., Wang P., Chen R. and Cheng X. 2005b. Quaternary upper ocean thermal gradient variations in the South China Sea: Implications for east Asian monsoon climate. Paleoceanography 20: PA4007, doi:10.1029/2004PA001115.

Tian J., Wang P., Cheng X. and Li Q. 2002. Astronomically tuned Plio-Pleistocene benthic $\delta^{18}O$ records from South China Sea and Atlantic-Pacific comparison. Earth Planet. Sci. Lett. 203: 1015–1029.

Tija H.D. 1980. The Sunda Shelf, Southeast Asia. Zeitschrift fuer Geomorphologie N.F. 24: 405–427.

Traverse A. 1988. Production, dispersal, and sedimentation of spore/pollen. In: Traverse. A. (eds.), Palynology, Charpter 17. Unwin Hyman, Boston, pp. 375–430.

Trentesaux A., Liu Z., Colin C., Clemens S.C., Boulay S. and Wang P. 2004. Clay mineral assemblages in the northern South China Sea: Implications for the East Asian monsoon evolution over the past 2 million years. In: Prell W.L., Wang P., Blum P., Rea D.K. and Clemens S.C. (eds.), Proc. ODP, Sci. Results 184 [Online].

Vandenberghe J., An Z., Nugteren G., Lu H. and Van Huissteden K. 1997. New absolute time scale for the Quaternary climate in the Chinese loess region by grain-size analysis. Geology 25: 270–273.

Van der Kaars S. 1991. Palynology of eastern Indonesian marine piston-core: a late Quaternary vegetational and climatic record for Australasia. Palaeogeogr. Palaeoclimatol. Palaeoecol. 85: 239–302.

Van der Kaars S., Wang S., Kershaw P., Guichard F. and Setiabudi D.A. 2000. A late Quaternary palaeoecological record from the Banda Sea, Indonesia: patterns of vegetation and biomass burning in Indonesia and northern Australia. Palaeogeogr. Palaeoclimatol. Palaeoecol. 155: 135–153.

Visser K., Thunell R.C. and Stott L. 2003. Magnitude and timing of temperature change in the Indo-Pacific warm pool during deglaciation. Nature 421: 152–155.

von Rad U., Schaaf M., Michels K.H., Schulz H., Berger W.H. and Sirocko F. 1999. A 5000-yr record of climate change in varved sediments from the oxygen minimum zone off Pakistan, northeastern Arabian Sea. Quat. Res. 51: 39–53.

Walker D. and Flenley J.R. 1976. Late Quaternary vegetational history of the Enga District of upland Papua New Guinea. Phil. Trans. R. Soc. B286: 265–344.

Wan S., Li A., Clift P.D. and Jiang H. 2006. Development of the East Asian summer monsoon: Evidence from the sediment record in the South China Sea since 8.5 Ma. Palaeogeogr. Palaeoclimatol. Palaeoecol. 241: 139–159.

Wan S., Li A., Clift P.C. and Stuut J.B.W. 2007. Development of the East Asian monsoon: Mineralogical and sedimentologic records in the northern South China Sea since 20 Ma. Palaeogeogr. Palaeoclimatol. Palaeoecol. 254: 561–582.

Wang B., Clemens S.C. and Liu P. 2003. Contrasting the Indian and East Asian monsoons: implications on geological timescales. Mar. Geol. 201: 5–21.

Wang L. 2000. Isotopic signals in two morphotypes of *Globigerinoides ruber* (white) from the South Chian Sea: implication ns for monsoon climate change during the last glacial cycle. Palaeogeogr. Palaeoclimatol. Palaeoecol. 161: 381–394.

Wang L., Sarenthein M., Erlenkeuser H., Grimalt J., Grootes P., Heilig S., Ivanova E., Kienast M., Pelejero C. and Pflaumann U. 1999a. East Asian monsoon Climate during the late Pleistocene: high- resolution sediment records from the South China Sea. Mar. Geol. 156: 245–284.

Wang L., Sarenthein M., Grootes P. and Erlenkeuser H. 1999b. Millennial reoccurrence of century- scale abrupt events of East Asian monsoon: A possible heat conveyor for the global deglaciation. Paleoceanography 14: 725–731.

Wang L. and Wang P. 1990. Late Quaternary paleoceano-graphy of the South China Sea: glacial-interglacial contrasts in an enclosed basin. Paleoceanography 5: 77–90.

Wang P. 1999. Response of Western Pacific marginal seas to glacial cycles: Paleoceanographic and sedimentological features. Mar. Geol. 156: 5–39.

Wang P., Clemens S., Beaufort L., Braconnot P., Ganssen G., Jian Z., Kershaw P. and Sarnthein M. 2005. Evolution and variability of the Asian monsoon system: state of the art and outstanding issues. Quat. Sci. Rev. 24: 595–629.

Wang P., Jian Z., Zhao Q., Li Q., Wang R., Liu Z., Wu G., Shao L., Wang J., Huang B., Fang D., Tian J., Li J., Li X., Wei G., Sun X., Luo Y., Su X., Mao S. and Chen M. 2003. Evolution of the South China Sea and monsoon history revealed in deep-sea records. Chinese Sci. Bull. 48(23): 2549–2561.

Wang P., Min Q., Bain Y. and Cheng X. 1981. Strata of Quaternary transgressions in East China: a preliminary study. Acta Geol. Sinica 1: 1–13 (in Chinese).

Wang P., Prell W.L., Blum P. (eds.). 2000. Proc. ODP, Init. Repts, Vol. 184 [CD-ROM]. Ocean Drilling Program, Texas A&M University, College Station TX 77845–9547, USA.

Wang P., Wang L., Bian Y. and Jian Z. 1995. Late Qauternary paleoceanography of the South China Sea: surface circulation and carbonate cycles. Mar. Geol. 127: 145–165.

Wang R. and Abelmann A. 2002. Radiolarian responses to paleoceanographic events of the southern South China Sea during the Pleistocene. Mar. Micropaleontol. 46: 25–44.

Wang R.J. and Li J. 2003. Quaternary high-resolution opal record and its paleo-productivity implication at ODP Site 1143, southern South China Sea. Chin. Sci. Bull. 48(4): 363–367.

Wang R., Clemens S., Huang B. and Chen M. 2003. Late Quaternary paleoceanographic changes in the northern South China Sea (ODP Site 1146): radiolarian evidence. J. Quat. Sci. 18(8): 745–756.

Wang Y.J., Cheng H., Edwards R.L., An Z.S., Wu J.Y., Shen C.C. and Dorale J.A. 2001. A high-resolution absolute-dated late Pleistocene monsoon record from Hulu Cave, China. Science 294: 2345–2348.

Wang Y.J., Cheng H., Edwards R.L., He Y.Q., Kong X.G., An Z.S., Wu J.Y., Kelly M.J., Dykoski C.A. and Li X.D. 2005. The Holocene Asian monsoon: Links to solar changes and North Atlantic climate. Science 308: 854–857.

Wang Y.J., Cheng H., Edwards L.R., Kong X., Shao X., Chen S., Wu J., Jiang X., Wang X. and An Z. 2008. Millennial-and orbital-scale changes in the East Asian monsoon over the past 224,000 years. Nature 451: 1090–1093.

Wang X. 2006. Paleovegetation on the Sunda Shelf over the last 40 ka and its paleoenveronment. Ph.D. Thesis, School of Ocean & Earth Sciences, Tongji University (in Chinese).

Wang X., Sun X., Wang P. and Stattegger K. 2007. A high-resolution history of vegetation and climate history on Sunda Shelf since the last glaciation. Sci. China (D) 50: 75–80.

Wang X., Sun X., Wang P. and Stattegger K. 2008. The records of coastline changes reflected by mangroves on the Sunda Shelf since the last 40 ka. Chinese Sci. Bull. 53(13): 2069–2076.

Wara M.W., Ravelo A.C. and Delaney M.L. 2005. Permanent El Niño–like conditions during the Pliocene warm period. Science 309: 758–761.

Wehausen R. and Brumsack H.J. 2002. Astronomical forcing of the East Asian monsoon mirrored by the composition of Pliocene South China Sea sediments. Earth Planet. Sci. Lett. 201: 621–636.

Wei G.J., Deng W.F., Liu Y. and Li X.H. 2007. High-resolution sea surface temperature records derived from foraminiferal Mg/Ca ratios during the last 260ka in the northern South China Sea. Palaeogeogr. Palaeoclimatol. Palaeoecol. 250: 126–138.

Wei G.J., Li X., Liu Y., Shao L. and Liang X. 2006. Geochemical record of chemical weathering and monsoon climate change since the early Miocene in the South China Sea. Paleoceanography 21: PA4214, doi: 10.1029/2006PA001300.

Wei K.Y., Chiu T.C. and Chen Y.G. 2003. Toward establishing a maritime proxy record of the East Asian summer monsoons for the late Quaternary. Mar. Geol. 201: 67–79.

Wu G., Qin J. and Mao S. 2003. Deep-water Oligocene pollen record from South China Sea. Chinese Sci. Bull. 48(22): 2511–2515.

Wyrtki K. 1961. Scientific results of marine investigations of the South China Sea and Gulf of Thailand 1959∼1961. Naga Rep. 2, Scripps Institution of Oceanography, University of California, San Diego, pp. 164–169.

Xu J., Wang P., Huang B., Li Q. and Jian Z. 2005. Response of planktonic foraminifera to glacial cycles: Mid-Pleistocene change in the southern South China Sea. Mar. Micropaleontol. 54: 89–105.

Yancheva G., Nowaczyk N.R., Mingram J., Dulsji P., Schetter G., Negendank J.F.W., Liu J., Sigman D.M., Peterson L.C. and Haug G.H. 2007. Influence of the intertropical convergence zone on the East Asian monsoon. Nature 7123: 74–77.

Yuan D., Chen H., Edwards R.L., Dykoski C.A., Kelly M.J., Zhang M., Qing J., Lin Y., Wang Y., Wu J., Dorale J.A., An Z. and Cai Y. 2004. Timing, duration, and transitions of the last interglacial Asian monsoon. Science 304: 575–578.

Zhang Y., Ji J., Baslsam W.L., Liu L. and Chen J. 2007. High resolution hematite and goethite records from ODP 1143, South China Sea: Co-evolution of monsoon precipitation and El Niño over the past 600,000 years. Earth Planet. Sci. Lett. 264: 136–150.

Zheng H.B., Powell C.M., Rea D.K., Wang J.L. and Wang P.X. 2004. Late Miocene and mid-Pliocene enhancement of the East Asian monsoon as viewed from the land and sea. Global Planet. Change 41: 147–155.

Zheng F., Li Q., Li B., Chen M., Tu X., Tian J. and Jian Z. 2005. A millennial scale planktonic foraminifer record of the mid-Pleistocene climate transition from the northern South China Sea. Palaeogeogr. Palaeoclimatol. Palaeoecol. 223: 349–363.

Zheng H., Powell C. McA., An Z., Zhou J. and Dong G. 2000. Pliocene uplift of the northern Tibetan Plateau. Geology 28: 715–718.

Zhao M., Huang C.Y., Wang C.C. and Wei G. 2006. A millennial-scale $U_{37}^{K'}$ sea-surface temperature record from the South China Sea (8°N) over the last 150 kyr: Monsoon and sea-level influence. Paleogeogr. Paleoclimat. Paleoecol. 236: 39–55.